DEGREE PROJECT IN ENGINEERING PHYSICS,
SECOND CYCLE, 30 CREDITS
STOCKHOLM, *SWEDEN 2021*

Superradiant axion clouds and their interaction with astrophysical plasma

ERIK ENGSTEDT

KTH ROYAL INSTITUTE OF TECHNOLOGY
SCHOOL OF ENGINEERING SCIENCES

KTH Engineering Sciences

Master of Science Thesis

Superradiant axion clouds and their interaction with astrophysical plasma

Erik Engstedt

Particle and Astroparticle Physics, Department of Physics,
School of Engineering Sciences,
KTH Royal Institute of Technology, SE-106 91 Stockholm, Sweden

Stockholm, Sweden 2021

Typeset in LaTeX

Examensarbete för avläggande av masterexamen i Teknisk Fysik, inom ämnesområdet teoretisk fysik.

Master thesis for the degree of Master of Science, in the subject area of Theoretical Physics.

TRITA-SCI-GRU 2021:348

Printed in Sweden by Universitetsservice US AB

Abstract

Axions are one of the best-motivated particles beyond the standard model of particle physics and a promising candidate for dark matter. Through the superradiant instability, axions can extract a significant amount of rotational energy from spinning black holes resulting in dense axion clouds. These axion clouds can imprint themselves on the spin of the black hole and even emit detectable gravitational waves, making them very potent tools in the search for axions.

The considerable number of axions present in these clouds can also compensate for the weak coupling between the axion and the standard model particles. However, the interaction between the cloud and the astrophysical plasma that the black hole accretes is often assumed to be negligible. In this thesis, we examine this assumption by studying the interaction between the astrophysical plasma and the axion cloud to determine if it can cause any significant effects.

We find no new gravitational signatures and can conclude that the interaction is not effective enough to halt the evolution of the cloud. Therefore, the main focus of this work is the emitted low-frequency photons that the axions convert into through the interaction. We find that the emission from systems with typical accretion rates can reach up to 10^{14} W and is most efficient around fast-spinning stellar black holes that accrete spherically without an accretion disk. However, we conclude that most of this emission will quickly be reabsorbed into the plasma and not cause any detectable signals.

We also study resonant conversion of axions, which can occur when the plasma frequency is comparable to the axion mass. We find that the low accretion rates that enable this are reachable around isolated stellar-mass black holes that travel rapidly through low-density regions of space. In these systems, the luminosity can reach 10^{25} W, and possibly even higher if we include stimulation effects. We can, therefore, conclude that a population of fast-traveling isolated black holes can pose a new tool in the search for axions.

Key words: axions, superradiance, black holes, black hole accretion, astrophysical plasma.

Sammanfattning

Axioner är en av de bäst motiverade partiklarna bortom standardmodellen för partikelfysik och en lovande kandidat för mörk materia. Genom superstrålning kan axioner extrahera en signifikant mängd rotationsenergi från svarta hål vilket kan resultera i täta axionmoln. Dessa axionmoln kan ge avtryck genom deras påverkan på spinnet hos svarta hål och till och med avge detekterbara gravitationsvågor. Detta gör axionmoln till kraftfulla verktyg i sökandet efter axioner.

Den stora mängd axioner som dessa moln består av kan också kompensera för den svaga växelverkan mellan axionerna och partiklarna från standardmodellen. Växelverkan mellan molnet och den astrofysikaliska plasmat som det svarta hålet ackumulerar från omgivningen antas ändå ofta vara försumbar. I denna rapport undersöker vi detta antagande genom att studera växelverkan mellan den astrofysikaliska plasmat och axionmolnet för att avgöra om den kan orsaka några observerbara effekter.

Vi finner inga nya gravitationella effekter och kan dra slutsatsen att växelverkan inte är tillräckligt effektiv för att påverka utvecklingen av axionmolnet. Därför är huvudfokus i detta arbete utstrålningen av de fotoner som resulterar från växelverkan. Vi finner att emissionen från system med typiska ackretionshastigheter kan nå upp till 10^{14} W och är mest effektiv kring svarta hål med låg massa och högt spinn som ackumulerar sfäriskt utan att bilda en ackretionsskiva. Vi drar dock slutsatsen att det mesta av denna emission snabbt kommer att återabsorberas i plasmat och inte orsaka några detekterbara signaler.

Vi studerar även konvertering av axioner via resonans, vilket kan inträffa när plasmafrekvensen är jämförbar med massan hos axionerna. Vi finner att de låga ackretionshastigheterna som möjliggör detta kan nås runt isolerade svarta hål som färdas snabbt genom delar av rymden med låg omgivande densitet. I dessa system kan luminositieten nå 10^{25} W, och möjligen ännu högre om vi inkluderar stimuleringseffekter. Vi kan därför dra slutsatsen att en population av isolerade svarta hål med hög hastighet kan potentiellt användas i sökandet efter axioner.

Key words: axioner, strålningsförstärkning, svarta hål, svart hålansamling, astrofysikalisk plasma.

Preface

Geometrized units

In the theoretical parts of this thesis we have used a set of geometrized units where $\hbar = G = c = k_B = 1$ which simplifies the algebra significantly. To return to SI or cgs units we use table 1 which allow us to switch between different units.

Table 1. Unit conversion table.

Quantity	Factor
Energy×Mass^{-1}	$1 = c^2 = 5.61 \times 10^{32}\,\mathrm{eV\,g^{-1}}$
Energy×Time	$1 = \hbar = 6.58 \times 10^{-16}\,\mathrm{eV\,s}$
Energy×Length	$1 = c\hbar = 1.97 \times 10^{-5}\,\mathrm{eV\,cm}$
Energy×Temperature^{-1}	$1 = k_B = 8.62 \times 10^{-5}\,\mathrm{eV\,K^{-1}}$

The only remaining unit, relevant for this thesis, is gauss, the cgs unit for magnetic field strength. To demonstrate how the table should be used we derive here the corresponding factor between eV and gauss:

$$1\,\mathrm{G} = 1\,\mathrm{g}^{1/2}\,\mathrm{cm}^{-1/2}\,\mathrm{s}^{-1} = \sqrt{\frac{5.61 \times 10^{32}\,\mathrm{eV}}{(1.97 \times 10^{-5}\,\mathrm{eV})^{-1}\,(6.58 \times 10^{-16}\,\mathrm{eV})^{-2}}} = 0.069\,\mathrm{eV}^2.$$

Acknowledgements

First and foremost, I want to thank my supervisor Ricardo Zambujal Ferreira for all the help and support throughout this interesting project. It has been fun and rewarding. Secondly, I want to thank Tommy Ohlsson for your patience and helpful feedback about the report. Finally, I want to thank my family for all the emotional support. Without you, this project would have been a lot harder. I especially want to thank my father for engaging in conversations about the project with me, even though you did not always understand what I was talking about.

Contents

Chapter 1

Introduction

Physics today is described by two immensely successful theories, the standard model of particle physics and general relativity. The former describes the known particles of the universe and their interactions through the electromagnetic and nuclear forces, while general relativity explains the large-scale structure of gravity. Although these theories are very successful, we know that some observations remain unaccounted for by them. One unexplained phenomenon in the intersection of the two is dark matter which we know accounts for a large portion of the energy content of the universe but whose exact nature is unknown.

There are many different theories about what constitutes dark matter, and one common explanation is the existence of particles beyond the standard model. One such particle is the light, weakly interacting, long-lived, pseudoscalar boson called the axion. It was first introduced in a solution to the strong CP problem [1–4] and was quickly found to have properties suitable to also account for up to all dark matter in the universe [5, 6]. This makes axions a particle of great interest since it could potentially answer two unanswered questions in physics. Due to this, a wide array of different experimental searches has developed over the years, and the search is still very active today [7]. Since its introduction, the theoretical aspects of axions have also evolved [8], and there is still a large parameter space yet unrestricted where axions could be found. Axion physics is, therefore, still a very active and evolving field.

Beyond the axion that solves the strong CP problem, sometimes referred to as the QCD-axion, other theories that include axion-like particles, or ALPs, have been developed. For example, one theory that predicts a large set of different ALPs with masses and couplings spanning many orders of magnitude is string theory [9]. Together, the QCD-axion and different ALP models, which we will collectively refer to as axions in this thesis, span a vast parameter space. Thus developing methods that can probe different parts of this parameter space is of great interest and can potentially lead to the discovery of new physics.

There is a variety of different methods used in the search for axions that have managed to restrict large portions of the parameter space [7]. This includes direct searches using helioscopes [10], haloscopes [11], and also light-shining-through-walls experiments [12]. The existence of axions can also have a significant effect on stellar evolution, and observations of stars have been a successful way to indirectly constrain axions [13–19]. The largest obstacle in the search for axions is the weak coupling with the particles of the standard model. A way to overcome this problem is to have an environment supporting large densities of axions that can compensate against the weak coupling. One source for creating a large axion density is the superradiant instability of rotating black holes [20–23]. Through the Penrose process [24], a boson field can extract energy from a spinning black hole through superradiant scattering. If the field is bound to the black hole, the scattering can repeat continuously, and enough energy can be extracted to noticeably spin down the black hole and cause the field to grow exponentially [22, 23, 25–27]. Thus, a small fluctuation in the axion field close to a black hole of the right mass can yield exponential growth of the number of axions, creating what is commonly called a superradiant axion cloud around the black hole.

In the most effective superradiant instabilities, the axion field can extract up to 29% [28] of the rotational energy of the black hole. This can cause major observational consequences and can be used to detect the instability, and consequentially the axion [29–37]. The simplest manifestation of this is that we would expect gaps in the mass-spin plots of the observed black hole population since all black holes with masses where the superradiant instability is effective should be spun down. The axion cloud will also give rise to monochromatic emission of gravitational waves at the frequency corresponding to the axion mass. These could then be detected using the emerging technology of gravitational-wave astronomy.

These gravitational channels of axion detection are the most explored signs of superradiant axion clouds. The clouds can also provide an environment where the interaction between axions and matter might become significant due to the large axion densities and some references have studied this. For example, Refs. [38–41] explored stimulated axion decay which can yield laser-like emission with large luminosities, in Refs. [29, 42] the conversion in the magnetic field around black holes are considered, and reactions with electrons found in the accreting plasma around the black hole have been studied in the case of superradiant vector bosons [43–45]. However, the interactions between the axion cloud and the astrophysical plasma around the black hole are more often than not assumed to be negligible.

In this thesis, we will explore this interaction between the axion cloud and the astrophysical plasma that the host black hole accretes. The interaction between the cloud and the plasma can convert axions into photons, yielding electromagnetic signals. If the conversion is effective enough to quench the superradiant growth, it could also affect the previously mentioned gravitational signatures. We will use accretion models such as Bondi accretion [46] and the accretion disk of Novikov and Thorne [47] to describe the surrounding plasma, which are good first approximations widely used in astrophysics. The interactions between the cloud and the

plasma can also be categorized into two parts: scattering processes and resonant conversion. The former dominates when the accretion rate is high, leading to a denser plasma, where photons are converted through the process $e + a \to e + \gamma$. For lower accretion rates, the plasma frequency can become comparable to the axion mass, allowing for resonant conversion to take place [48]. We will analyze these scenarios separately to determine for which black hole systems the interaction between the plasma and the axion cloud could lead to observable signals.

1.1 Outline

The thesis is structured as follows. The next chapter provides the necessary background regarding axions, black holes, superradiance, and the accretion models used throughout the thesis. The two subsequent chapters comprise the main part of the thesis. In chapter 3 we investigate the scattering processes found in denser accretion flows, while in chapter 4 resonant conversion in less dense accretion flows is studied. In chapter 5 we discuss the possible detection strategies of the signals estimated in the previous chapters. We also include a discussion of the most critical uncertainties of the thesis in this chapter. Finally, in chapter 6 the thesis is summarized and concluded.

Chapter 2

Background

In this chapter, we will go through the basic theory and terminology needed to understand the rest of the thesis. References are provided for more detailed accounts for the interested reader. In the first section, we will briefly review the QCD-axion and the generalization to axion-like particles. After that, the basics of Kerr black holes are presented to introduce the concept of superradiant instabilities, which are described in the subsequent section. The chapter concludes with a section describing basic accretion theory and the accretion models used in this thesis.

2.1 Axion phenomenology

2.1.1 The QCD-axion

The first axion, or *the* axion, also called the QCD-axion, was found as a consequence of a solution to the strong CP problem proposed by Peccei and Quinn in 1977 [1, 2]. In order to explain why QCD does not violate CP-symmetry, they introduced a new U(1) symmetry, often referred to as the PQ-symmetry or $\mathrm{U}(1)_{PQ}$, which spontaneously breaks at a large energy scale, usually denoted f_a. Shortly after, Weinberg and Wilczek pointed out that this symmetry breaking results in a new pseudo-Goldstone boson which is the particle we now call the axion [3, 4]. This axion turns out to be a very light, weakly interacting, and stable pseudoscalar boson, and these properties makes the axion an excellent candidate for dark matter [5, 6].

Through its relationship to QCD, the axion is coupled to the gluon but beyond that there exist different models of the QCD-axion. These are usually based on two fundamental models, KSVZ [49], and DFSZ [50], where the major differences lay in which particles are coupled under the PQ-symmetry. A recent review of the QCD-axion and these models is given in Ref. [8]. The explicit details of the underlying symmetries are not relevant to this thesis, and we will only go through the axion properties relevant to us.

Fundamentally we have that the mass of the QCD-axion is inversely proportional to f_a, which in some models can exceed the GUT scale of $f_{GUT} \sim 10^{16}$GeV, and is explicitly given by [8]

$$m_a \approx 5.7 \left(\frac{1 \times 10^{12}\,\text{GeV}}{f_a} \right) \mu\text{eV}. \tag{2.1}$$

Further, all couplings to the standard model particles are also suppressed by f_a, thus the scale of f_a is the reason the axion is so light and weakly interacting. Smaller f_a is generally restricted by experiments and one usually considers $f_a > 10^8$ GeV. In this thesis we are mainly interested in the axions interaction with photons and electrons. The photon coupling is included through the Lagrangian term

$$\mathcal{L}_a \supset \frac{g_{a\gamma}}{4} F_{\mu\nu} \tilde{F}^{\mu\nu} a, \tag{2.2}$$

where the coupling constant is given by[1]

$$g_{a\gamma} = \frac{\alpha_{em}}{2\pi f_a} \left[\frac{E}{N} - \frac{2}{3} \frac{4m_d + m_u}{m_u + m_d} \right]. \tag{2.3}$$

The second term of this coupling constant comes from the fundamental connection with the quarks, which allow the axion to interact with the photon through pions. m_u and m_d are the mass of the up and down quark, respectively. The first term is due to anomalies in the conservation of the PQ-current and yields a direct coupling to the photon. The exact values are model dependent, but typically $E/N \sim O(1)$.

The electron coupling is given by the Lagrangian term

$$\mathcal{L}_a \supset \frac{g_{ae}}{2m_e} \bar{e} \gamma^\mu \gamma_5 e \partial_\mu a, \tag{2.4}$$

where

$$g_{ae} = \frac{m_e}{f_a} \left(c_e^0 + \delta c_e \right). \tag{2.5}$$

e is the electron field, m_e is the electron mass, c_e^0 is the tree-level coupling which are present in some models, and δc_e is related to $g_{a\gamma}$ through one-loop diagrams involving photons. We have that $c_e^0 \sim O(0.1)$ for DFSZ and $c_e^0 = 0$ for KSVZ.

2.1.2 Axion-like particles

Since the mass of the QCD-axion is directly related to the decay constant f_a, the available parameter space is narrow. With multiple experiments excluding large parts of the parameter space, the existence of the QCD-axion has become less and less likely, at least for masses larger than approximately $O(0.1)$ eV [51]. There are, however, other theories, mainly string theory [9], that have introduced axion-like particles (ALPs) which have the same properties as the QCD-axion but are

[1] α_{em} is the fine-structure constant.

unrelated to the strong CP problem. The decay constant and mass of these ALPs are not necessarily related, which extends the possible parameter space where the axion could be found. We will, in this thesis, consider a general axion that has a mass m_a and couplings $g_{a\gamma}$ and g_{ae} unrelated to each other.

2.1.3 Experimental searches

There are a variety of different methods used in the search for axions that have managed to restrict large portions of the parameter space [7]. Some methods that have tried to detect the axions directly are helioscopes and haloscopes. Helioscopes, such as CAST at CERN [10], try to detect axions created in the Sun, while haloscopes, such as ADMX [11], looks for dark matter axions passing through Earth. Some experiments also try to simultaneously create and detect the axion in a laboratory. These are so-called light-shining-through-walls experiments [12], where some of the photons in a laser beam aimed at a wall should convert into axions, which then can pass through the wall, before finally turning back into photons on the other side, giving the illusion that the laser shined through the wall. Indirect methods, such as astrophysical observations of stellar evolution has also been successfully in restricting large portions of the parameter space [13–19]. These exploit the fact that an axion coupled to the standard model particles should carry away a significant amount of energy from a star, altering its evolution. Thus, observing stars in different stages of their evolution cycle can restrict the existence of axions with certain masses and couplings.

These experiments do not generally rely on the mass-coupling relation of the QCD-axion, so the experimental upper bounds found for the couplings are valid for all axions in a certain mass range. Axions with $m_a < 10^{-10}$ eV are those which can experience superradiant growth around astrophysical black holes and which are the focus of this thesis. The current upper bound on the photon coupling for these masses comes from the helioscope CAST at CERN [10] which sets it at

$$g_{a\gamma} < 0.66 \times 10^{-10}\,\mathrm{GeV}^{-1} \tag{2.6}$$

for masses bellow $m_a < 0.02$ eV. The upper limit on the electron coupling comes from astrophysical observations of red giants and white dwarfs and are set at around [7, 8]

$$g_{ae} < 3 \times 10^{-13} \tag{2.7}$$

for all masses of interest.

2.2 Kerr black holes

Black holes are relatively simple objects and can effectively be described by just their mass and angular momentum, assuming that they have no net electric charge. We usually categorize black holes into two main categories based on their mass:

stellar black holes and supermassive black holes (SMBHs). Stellar black holes are those believed to originate from collapsed stars and have masses of order $10M_\odot$, where $M_\odot = 2 \times 10^{30}\,\mathrm{kg}$ is the solar mass. The smallest observed stellar black hole candidate has a mass of around $3M_\odot$ [52] and the largest around $60M_\odot$ [53]. SMBHs reside in the center of galaxies and have masses of around $10^5 - 10^{10}M_\odot$. Two examples are Sagittarius A* with the mass $\sim 4 \times 10^6 M_\odot$ [54] in the center of the Milky Way, and Messier 87 with a mass of $\sim 6.2 \times 10^9 M_\odot$ [55]. Black holes with masses in the region between stellar and SMBHs are less prevalent and usually referred to as intermediate black holes. The only observed candidates in this category are formed through the merging of two large stellar black holes [56].

If the black hole has no angular momentum, then space-time around it is described by the famous Schwarzschild metric. However, we expect black holes to carry some rotational energy, which will reshape space-time around them. Roy Kerr was first to suggest a solution to Einstein's field equations which included angular momentum [57]. Spinning black holes are, therefore, often referred to as Kerr black holes. The rotational motion is included in the metric through the spin parameter

$$a = \frac{J}{M}, \tag{2.8}$$

where J is the total angular momentum of the black hole. This parameter is restricted by $a < M$ to prevent naked singularities [58] and when $a \approx M$, the black hole is called extremal. Measuring the spin of a black hole is more difficult than measuring the mass, and estimations of spins are, therefore, less certain. However, there is evidence for black holes with spin down to around $0.1M$ and up to $0.99M$, and there seems to be a inclination towards more rapidly spinning black holes [59].

Space-time around a Kerr black hole is best descibed in Boyer–Lindquist coordinates, (t, r, θ, ϕ), by the metric [60]

$$\begin{aligned} ds^2 = &-\left(1 - \frac{2Mr}{\rho^2}\right) dt^2 - \frac{4Mra}{\rho^2} \sin^2\theta dt d\phi \\ &+ \frac{\rho^2}{\Delta} dr^2 + \rho^2 d\theta^2 + \left(r^2 + a^2 + \frac{2Mra^2 \sin^2\theta}{\rho^2}\right) \sin^2\theta d\phi^2, \end{aligned} \tag{2.9}$$

where

$$\rho^2 = r^2 + a^2 \cos^2\theta \text{ and } \Delta = r^2 + a^2 - 2Mr. \tag{2.10}$$

This metric introduces multiple important quantities, which we want to highlight. First of all, we have the gravitational radius, which in geometrized units is $r_g = M$. This radius describes the scale of the black hole, and we will normalize distances to this, $r \to r/M$, after this section. Further, we have the coordinate singularity at $\Delta = 0$, which corresponds to the event horizon, but in contrast to the Schwarzschild metric, we have two solutions, given by

$$r_\pm = M \pm \sqrt{M^2 - a^2}. \tag{2.11}$$

r_+ can be thought of as the typical event horizon and coincide with the one in the Schwarzschild metric when $a = 0$. We also have a region outside the event horizon, called the ergosphere, in which extraction of energy is possible. This region is defined as where $-(1 - 2Mr/\rho^2) > 0$ and the surface

$$r_e = M + \sqrt{M^2 - a^2 \cos^2(\theta)} \tag{2.12}$$

is its outer edge. The existence of this region is what allows the superradiant instability to occur. Another surface of importance is the innermost stable circular orbit (ISCO), r_{isco}, which is given by a more involved expression, see for example eq. (2) in [59], but has the limits $r_{isco}(a = M) = r_+$ and $r_{isco}(a = 0) = 6M$. The ISCO is the closest a stable circular orbit can be held without the object necessarily plummeting into the black hole. The ISCO is important in accretion disk models, where the inner edge usually is assumed to coincide with it. Lastly, we have the angular velocity of the event horizon

$$\Omega = \frac{a}{2Mr_+}, \tag{2.13}$$

which is an important quantity for describing the superradiant instability.

2.3 The superradiant instability

Superradiance is an amplification effect where, under the right circumstances, a wave scattering off a rotating body can be amplified by extracting rotational energy from the body [28, 61]. When the rotating body is a Kerr black hole, superradiant scattering can work in conjunction with the Penrose process [24] to extract energy from the black hole. If the source of the scattering is bounded to the black hole, the extraction of energy can repeat indefinitely, leading to an instability of the Kerr metric. This process can extract a significant amount of rotational energy from the black hole, which can spin it down noticeably. The extracted energy is deposited into the field, leading to a large density around the black hole. This process was first considered in the context of a "black hole bomb" where photons were bound to a black hole by an enclosing mirror [20, 21, 62], but the mass of a massive boson field works equally well to bound the field [22, 23, 25, 26, 33]. Thus, small fluctuations of a massive boson field around a Kerr black hole can lead to exponential growth of the number density of the corresponding particle [22, 23]. This growth is most efficient for vector bosons [27], and non-existent for fermions because of Pauli-blocking [63]. In this thesis, we are interested in the (pseudo)scalar case, relevant for axions.

For the superradiant instability to be effective, the Compton wavelength of the axion, $\sim 1/m_a$, must be of the same order as the gravitational radius of the black hole, $r_g = M$. Therefore, the gravitational coupling

$$\alpha = Mm_a \tag{2.14}$$

is closely linked to the effectiveness of the superradiant instability of black holes, and $\alpha \sim O(1)$ corresponds to the fastest energy extraction and subsequent growth

of the surrounding field. More specifically, numerical investigations have found that, for an extremal black hole, $\alpha = 0.42$ yields the fastest growth rates [64]. For $\alpha > 1$ the instability is exponentially suppressed [22], whereas when $\alpha \ll 1$ the growth rate are proportional to some power of α. $\alpha \lesssim 1$ is, therefore, the most interesting case. From eq. (2.14) we then get that the superradiant instability can effectively create large densities of axions around stellar black holes if $m_a \lesssim 10^{-11}$ eV, and around SMBHs if $m_a \lesssim 10^{-16}$ eV.

2.3.1 The superradiant rates

The superradiant instability is found when one analyzes the Klein–Gordon equation,

$$\left(\nabla_\mu \nabla^\mu - m_a^2\right) \varphi = 0, \tag{2.15}$$

in the Kerr-background, eq. (2.9). Even though the field can extract a significant portion of the energy of the black hole, the energy will be spread out over a large volume. It is, therefore, enough to consider the vacuum equation and neglect any backreactions as a first-order approximation in α [31]. The equation then turns out to be separable by the ansatz [65]

$$\varphi = e^{-\mathrm{i}\omega t + \mathrm{i}m\phi} R(r) S(\theta), \tag{2.16}$$

where $R(r)$ solves the radial equation (A.3), and $S(\theta)$ solves the angular equation (A.4). There are many references exploring these equations both numerically and analytically in different approximations. Some detailed references are Refs. [22, 23, 25–27, 29, 31, 62, 65], a review is given in Ref. [28], and a derivation in the non-relativistic, $\omega \sim m_a$, weak coupling, $\alpha \ll 1$, and slow spinning, $a \ll M$, limits is provided in appendix A of this thesis. The main goal is to determine the energy eigenvalues, ω, of the quasibound-modes of the equation, which turn out to have a small imaginary part, $\Gamma = \mathrm{Im}(\omega)$. If $\Gamma > 0$, which is the case when the so-called superradiant condition

$$m\Omega - \omega > 0 \tag{2.17}$$

is satisfied, the field will grow exponentially with e-folding time $1/\Gamma$, and the superradiant instability is found. The basic approach in finding ω, and subsequently Γ, is to consider the radial equation in two regions, the far region $r \gg M$ and the near region $r \ll 1/m_a$. When $\alpha < 1$, the two regions overlap, and by matching the far and near solutions in the overlap, one obtains an equation for ω. The final expressions can be found in many places, expressed slightly differently, and in this section, we summarize the analytical results which are in good agreement for numerical calculations for $\alpha < 0.2$ and all spins. It is worth noting that, even though the following analytic results do not apply for $\alpha \sim 0.4$, that a large cloud still grows with only a slightly slower rate than predicted by these expressions [28, 64]. This discrepancy is only relevant when studying the full time evolution of the systems, which is not part of this thesis.

The solution to eq. (2.15) is very similar to that of the hydrogen atom, and this system is, therefore, sometimes referred to as the gravitational atom [27]. The quasi-bound hydrogen like states are labeled by the three quantum numbers n, l, and m, where l and m are the usual angular momentum numbers and $\tilde{n} = n+l+1$ is the principle number. It varies in the references whether one uses n or $\tilde{n}$, we will stick to n. The frequency, $\mathrm{Re}(\omega)$, which we from now on refer to as ω_{nlm}, is given, to second order in α, by

$$\omega_{nlm} = m_a \left(1 - \frac{\alpha^2}{2(n+l+1)^2}\right), \tag{2.18}$$

and the imaginary part $\Gamma_{nlm} = \mathrm{Im}(\omega)$, also called the superradiant rate, is given by [29]

$$\Gamma_{nlm} = m_a \alpha^{4l+4} r_+ \left(m\Omega - \omega\right) C_{nlm}, \tag{2.19}$$

where

$$C_{nlm} = \frac{2^{4l+3}(2l+n+1)!}{(l+n+1)^{2l+4} n!} \left(\frac{l!}{(2l)!(2l+1)!}\right)^2 \times \prod_{j=1}^{l} \left(j^2 \left(1 - \frac{a^2}{r_g^2}\right) + 4r_+^2 \left(m\Omega - \omega\right)^2\right). \tag{2.20}$$

We see here that the rate is only positive if eq. (2.17) is satisfied. Since Ω is proportional to a, which will decrease by the energy extraction, the instability will eventually shut down, specifically when

$$m\frac{a}{M} < \frac{4m\alpha}{m^2 + 4\alpha^2}. \tag{2.21}$$

From the superradiant condition, we also see that only modes with $m > 0$ can extract energy from the black hole, i.e. the infalling wave has to have angular motion parallel to the black hole spin. Further, the rate decreases with growing l, and the most efficient mode has $n = 0$ and $l = m = 1$, which corresponds to the $2p$ state of the hydrogen atom. In the slow-spinning approximation, $a \ll M$, the rate of this mode is

$$\Gamma_{011} \approx \frac{a}{M}\frac{\alpha^9}{24M}, \tag{2.22}$$

which expressed in seconds

$$\Gamma_{011} = 8.4 \times 10^{-6} \left(\frac{a}{M}\right) \left(\frac{\alpha}{0.1}\right)^9 \left(\frac{M_\odot}{M}\right) \mathrm{s}^{-1}. \tag{2.23}$$

For superradiant growth to be observationally relevant, α and M must satisfy [33]

$$0.005 \left(\frac{M}{3M_\odot}\right)^{1/9} \lesssim \alpha < 0.5. \tag{2.24}$$

The lower limit comes from requiring that $1/\Gamma_{011}$ should be shorter than the age of the universe and the upper limit comes from condition (2.21) which blocks superradiant growth for all $\alpha > 0.5$ independently of spin.

2.3.2 Shape and size of the dominate mode

If the instability is present, a large population of axions will accumulate around the black hole. We call this population a superradiant axion cloud. As mentioned, the $2p$ state grows the fastest and will dominate the cloud. We can, therefore, in this thesis, disregard all the other states. This would not be the case if one includes self-interactions [37] or when one studies the details of gravitational wave emission where level transitions are important [30, 31, 33, 34].

In the small α limit, the wave function of the dominate state is approximately [31]

$$\varphi \approx A_0 e^{-\mathrm{i}\omega_{011}t+\Gamma_{011}t+\mathrm{i}\phi}\alpha^2 r \exp\Big(-\alpha^2\frac{r}{2}\Big)\sin\theta. \tag{2.25}$$

A_0^2 is proportional $f = M_{cl}/M$ where M_{cl} is the total mass of the axion cloud. We note here that we have scaled the radial coordinate to the gravitational radius, $r \to r/M$, which will be kept throughout the thesis unless otherwise stated. The dominant state also has $\omega_{011} = m_a(1-\alpha^2/8)$, and one can identify the velocity of the axions as $v \approx \alpha/2$, which means that for small α it is safe to consider the axions as non-relativistic [29]. We can, therefore, estimate the number density in the cloud as $n_a = \rho/m_a = -T^0_0/m_a$ where $T^{\mu\nu}$ is the energy-momentum tensor. From Ref. [31] we then have

$$n_a \approx \frac{M_{cl}}{64\pi M^2}\alpha^7\exp\big(-\alpha^2 r\big)\left[1+\cos^2\theta+\sin^2\theta\left(1-\alpha^2 r+\frac{\alpha^4}{4}r^2+2\alpha^2 r^2\right)\right] \tag{2.26}$$

assuming $1/\omega_{011} \ll 1/\Gamma_{011}$, i.e. the field oscillations occur on much shorter time scales than the superradiant growth. We have neglected the time dependence in this expression, which is valid as long as we consider time scales much shorter than $1/\Gamma_{011}$ where M_{cl}, M, and α are roughly constant. To get the exact time dependence of the cloud, the corresponding time evolution equations should be solved, including depletion through gravitational waves and other channels, see e.g. Ref. [31]. We can get a limit on the maximum mass the cloud can acquire by imposing that the angular momentum of the cloud should not exceed that of the black hole [39]. If N_a is the number of axions in the cloud, then $J_{cl} = lN_a$ is the total angular momentum, where $l = 1$ is the azimuthal quantum number for the dominant mode. With this, we can derive the following condition

$$1 > \frac{J_{cl}}{J_{BH}} = \frac{N_a}{aM} = \frac{m_a N_a}{m_a M^2 a/M} = \frac{M_{cl}}{\alpha M a/M} = \frac{f}{\alpha a/M}, \tag{2.27}$$

which limits the mass to $f < \alpha$ for an extremal black hole. More detailed considerations yield an overall maximum mass of $f \approx 0.29$ [28].

The spacial distribution of the axion cloud can be estimated with the radial expectation value, which for the dominante state is [28, 39]

$$\langle r \rangle \equiv r_{cl} = \frac{5}{\alpha^2}. \tag{2.28}$$

For the extent of the cloud, we have the standard deivation of the radial cordinate

$$\Delta r_{cl} = \frac{\sqrt{5}}{\alpha^2}. \tag{2.29}$$

The cloud is, therefore, fairly localized around $r \sim 1/\alpha^2 \gg r_g$ and a first order approximation for the number density of the cloud, used in, for example, Ref. [39], is to assume that the axions are homogeneously spread out in a torus with major radius r_{cl} and minor radius Δr_{cl}. With this we get the homogeneous-density approximation

$$n_a^{(h)} = \frac{fM}{m_a V_c}. \tag{2.30}$$

V_c is the volume of the torus which is

$$V_c = \pi(\Delta r_{cl} M)^2 2\pi r_{cl} M = 2\pi^2 \left(\frac{\sqrt{5}M}{\alpha^2}\right)^2 \frac{5M}{\alpha^2} = 50\pi^2 \frac{M^3}{\alpha^6} \tag{2.31}$$

in this approximation. With this we have

$$n_a^{(h)} = \frac{fM\alpha^6}{50\pi^2 m_a M^3} = \frac{f\alpha^5}{50\pi^2 M}. \tag{2.32}$$

Nummerically this is

$$n_a^{(h)} = 5.2 \times 10^{44} \left(\frac{f}{0.01}\right) \left(\frac{\alpha}{0.01}\right)^5 \left(\frac{M}{10 M_\odot}\right)^{-1} \text{cm}^{-3}, \tag{2.33}$$

which is very large, and why the superradiant axion clouds are potent tools in the search for the axion.

2.4 Accretion models

Even though black holes are quite simple objects in and of themselves, they all accrete matter from their surroundings which adds complexity to the system. Accretion physics is an extensive and active field of research because of its essential role in stellar, galactic, and black hole evolution and its role in black hole detection. Much of the accretion modeling today is based on magnetohydrodynamic simulations, see, for example, Ref. [54]. However, a couple of fundamental accretion models are widely used as starting points and give good first approximations

when studying accretion flows. These are accretion disks and spherical accretion, which will give good magnitude estimations suitable for this thesis.

The nature of black hole accretion is mainly determined by the accretion rate, $\dot{M}$, which describes how much matter is captured by the black hole per second. The rate is usually normalized against the Eddington rate,

$$\dot{M}_{edd} = \frac{L_{edd}}{\eta c^2}. \tag{2.34}$$

The Eddington luminosity, L_{edd}, is the luminosity which balances the radiative force with gravitational force and is roughly $L_{edd} = 1.2 \times 10^{38} M/M_{\odot} \mathrm{erg\,s^{-1}}$. η is the radiative efficency which is typically taken to be ~ 0.1 for black holes [60, 66]. The normalized accretion rate is then

$$\dot{m} = \frac{\dot{M}}{\dot{M}_{edd}} \approx \frac{\dot{M}}{1.33 \times 10^{18} \frac{M}{M_{\odot}} \mathrm{g\,s^{-1}}}. \tag{2.35}$$

If the accretion rate is high, $0.01 < \dot{m} < 1$, then there will be high friction in the flow, and the angular momentum will even out and align the matter into an accretion disk [47, 66, 67]. When the accretion rate is low, $\dot{m} \ll 0.01$, the flow becomes almost spherically symmetric and can be described as free-falling particles [46, 68–70]. There are multiple models between these two edge cases, most notably advection-dominated accretion flow (ADAF) [71, 72], but in this thesis, we will limit ourselves to these two simpler models, which will suffice as base approximations. Some typical accretion rates are $\dot{m} \sim 1$ for stellar black holes fueled by a companion star in a binary system, and $\dot{m} \sim 10^{-6}$ for SMBHs fueled by the denser inner regions of galaxies [54, 55]. One can also consider isolated black holes for which the properties of the surrounding medium determines the accretion rate and will typically result in rates lower than 10^{-8}. An accretion disk will surround stellar black holes, and the accretion flow around the SMBHs and isolated black holes are well approximated by spherical accretion.

2.4.1 Accretion disks

The most famous accretion models are the thin-disk by Shakura and Sunyaev [67], and its relativistic extension by Novikov and Thorne [47]. Some basic assumptions make it possible to solve the flow equations and extract radial profiles describing the accretion flow in three distinct radial regions defined by the dominant pressure. In the innermost region, the radiation pressure dominates, while in the outer two, the gas pressure dominates. The difference between the outer and the middle region is the process that determines the opacity. In the middle region, electron scattering dominates, whereas free-free absorption is most important in the outer region.

In this thesis, we are interested in black holes with high spin where relativistic effects can become important. We will, therefore, use the Novikov–Thorne model to describe accretion disks. The density and temperature profile, as well as the

disk thickness are all given in appendix B for each region of the Novikov–Thorne model. These are all radial expressions which depend on the black hole mass, the accretion rate, the spin, and a parameter α_p, usually taken to be $\alpha_p = 0.1$ [67], which describes the efficiency of the angular momentum transport. In appendix B are also the equations that describes the transition between the regions provided. Usually, the transitions occur at around $r \sim 100$ and $r \sim 10^3 - 10^4$ for typical stellar black holes and at $r \sim 10$ and $r \sim 100$ for SMBHs. We will through out chapter 3, where we study accretion disks, use the full equations found in appendix B for all numerical calculations.

2.4.2 Spherical accretion

The accretion rate is very low in spherical accretion, and friction between the accreted matter is almost negligible. One can, therefore, treat the accreted particles to be in free fall. In this thesis, we will consider two somewhat distinct cases where spherical accretion is relevant. The first is when we have an isolated black hole whose only source of matter is from the interstellar medium. In this case, we can estimate the accretion rate from the properties of the medium. In the second case, the accretion rate is known, for example, from observations. For example, for some SMBH where the rate can be estimated through observations, see, for example, Ref. [55].

The setup for describing spherical accretion is that we have a black hole traveling with velocity v_{rel} relative to an ambient medium with density ρ_∞ and temperature T_∞. We will also assume that the medium consists solely of hydrogen. The ambient particles will then travel with a speed of order [46, 68]

$$v_{eff} \approx \sqrt{v_{rel}^2 + c_s^2} \tag{2.36}$$

relative to the black hole, where c_s is the sound speed of the medium. The hydrogen particles will be captured by the black hole if the effective velocity is smaller than the escape velocity, i.e. , if

$$\frac{m_p}{r} > \frac{m_p v_{eff}^2}{2}, \tag{2.37}$$

where we remind ourselves that we have scaled the radius to the black hole mass. From this we define the capture radius, also known as the Bondi radius, as

$$r_b = \frac{2}{v_{eff}^2}. \tag{2.38}$$

This radius define the extent of the spherical accretion flow. The relative velocity of black holes are expected to be of the same order as the sound speed, typically $10 - 100\,\mathrm{km\,s^{-1}}$ [68, 73], but extreme events such as black hole mergers can kick the remnant black hole to speeds approaching $5000\,\mathrm{km\,s^{-1}}$ [74].

The accretion rate for spherical accretion can be estimated by the Bondi–Hoyle–Lyttleton formula [46, 68, 69]

$$\dot{M}_{BHL} = 4\pi\lambda_s M^2 \rho_\infty v_{eff}^{-3}, \tag{2.39}$$

where $\lambda_s \in O(1)$ is a factor that depends on the equation of state. This formula corresponds to a normalized rate of

$$\dot{m} = \frac{\dot{M}_{BHL}}{\dot{M}_{edd}} \approx 10^{-8}\lambda_s \left(\frac{M}{M_\odot}\right)\left(\frac{n_\infty}{1\,\mathrm{cm}^{-3}}\right)\left(\frac{v_{eff}}{10^{-4}}\right)^{-3/2}, \tag{2.40}$$

where $n_\infty = \rho_\infty/m_p$ is the number density of the interstellar medium. Assuming that the rate is constant all the way down to the horizon we have

$$\dot{M} = 4\pi M^2 r^2 v_r(r)\rho(r) = \text{constant}, \tag{2.41}$$

where v_r is the radial velocity of the accreted matter, and $\rho(r)$ is the density of the flow. A simple approximation for the radial velcoity is the free fall velocity

$$v_r(r) \approx \sqrt{\frac{2}{r}}, \tag{2.42}$$

for which we note that $v_r(r_b) = v_{eff}$. From this we can extract the density profile as

$$n(r) = \frac{\dot{M}}{4\sqrt{2}\pi m_p M^2 r^{3/2}}, \tag{2.43}$$

which can be used directly when $\dot{M}$ is known. If not, we insert $\dot{M}_{BHL}$ and get

$$n(r) = \frac{\lambda_s}{4} n_\infty \left(\frac{r_b}{r}\right)^{3/2}. \tag{2.44}$$

This expression coincides with the general relativistic derivation made in Ref. [69], but we have substituted for the effective velocity. λ_s is determined from the equation of state, and for an ideal gas $\lambda_s = 1/4$, we will for simplicity set $\lambda_s = 1$ in this thesis. We note that $n(r_b) < n_\infty$, in this model which is due to the fact that r_b is not as rigorously defined and just captures the general scale. Furthermore, it is common to consider the accretion to be further suppressed by an effective factor λ_{eff} as well, i.e. $\dot{M}_{BHL} \to \lambda_{eff}\dot{M}_{BHL}$, where λ_{eff} captures the outflow of matter from the black hole [75]. From the lack of X-ray signals from an expected population of isolated black holes in our galaxy, there are arguments for this parameter to be as small as $\lambda_{eff} \sim 10^{-3}$ [73, 75–77].

The accreting plasma will also sustain a magnetic field. The field strength can be estimated from the equipartition of magnetic and gravitational energy [68, 70],

$$\frac{B^2}{8\pi} \approx \frac{1}{6}\rho v_r(r)^2 \approx \frac{1}{3}\frac{\rho}{r}. \tag{2.45}$$

With the electron density in eq. (2.44) we get the radial profile as

$$B(r) \approx \sqrt{\frac{2\pi m_p n_\infty}{3}} r_b^{3/4} r^{-5/4} \approx 3\times 10^3 \left(\frac{n_{e,\infty}}{1\,\mathrm{cm}^{-3}}\right)^{1/2} \left(\frac{v_{eff}}{10^{-3}}\right)^{-3/2} r^{-5/4}\mathrm{G}. \tag{2.46}$$

Another way to estimate the magnetic field is to use the equipartition between magnetic and gas pressure, $B^2 \propto n_e T$, but due to the uncertainty in the electron temperature, which we will discuss next, the above expression is preferable.

The most complicated aspect of spherical accretion is that of the temperature. The simplest approach is to assume only adiabatic compression, then

$$T(r) = T_\infty \frac{r_b}{r} \tag{2.47}$$

for an ideal gas [69, 70]. However, this is mainly only accurate for the protons in the flow. When the accretion rate is low, then the time to reach thermal equilibrium between protons and electrons is longer than the time for the matter to reach the singularity, and we effectively get a two-temperature flow [68, 72, 78]. The electron temperature can then be described by the equation [78]

$$\frac{dT_e}{dr} + \frac{3}{2}(\gamma-1)\frac{T_e}{r} + \frac{4m_p M^3 \pi}{k\dot{M}}(\gamma-1)r^2(\Gamma_e - \Lambda_e) = 0, \tag{2.48}$$

where Γ_e and Λ_e account for all heating and cooling of the electrons and γ is the adiabatic index. The main heating is due to the Coulomb interactions with the protons, whereas the cooling has three main parts, bremsstrahlung, synchrotron radiation, and inverse Compton scattering of the synchrotron photons. The general treatment of this equation is difficult, and it is further complicated by the fact that the infall time can become shorter than the thermalization time of the electrons [72]. What is often done instead is to use a reduced version of eq. (2.47) as an approximation. This is motivated by the fact that if $v_{rel} \ll c_s$, where $c_s = \sqrt{5T_\infty/3m_p}$ is the sound speed in an ideal hydrogen gas, eq. (2.47) becomes

$$T(r) = T_\infty \frac{2}{rc_s^2} = \frac{6m_p}{5r} \approx \frac{1\times 10^{13}\,\mathrm{K}}{r}, \tag{2.49}$$

which would result in extremely relativistic electrons close to the black hole. These energetic electrons will cool much more efficently and both Refs. [72, 78] conclude that for higher accretion rates, the electron temperature will not exceed far above 10^{11} K, and studies of SMBHs reach similar conclusions [54, 79]. Thus, the electron

temperature is typical taken to be two orders of magnitude smaller than eq. (2.47), i.e.

$$T_e(r) \approx \frac{10^{11}\mathrm{K}}{r}, \tag{2.50}$$

used in, for example, Refs. [55, 70, 71]. However, in this thesis we will also be interested in the more extreme case of low densities where cooling effects will be less efficient. The literature is somewhat sparse on this topic. One model, found in Ref. [68], predicts very high temperatures at the black hole. Using their arguments we get that the radius where the electrons become relativistic, $T_e(r_{rel}) = m_e$, can be found from the equation

$$\frac{T_\infty}{m_e}\left(\frac{r_b}{r_{rel}}\right)^{5/4} + \frac{6m_p}{5m_e r_{rel}}\left(\left(\frac{r_b}{r_{rel}}\right)^{1/4} - 1\right) = 1, \tag{2.51}$$

and the electrons reach almost $T_e = m_p$ at the black hole. We will, in this thesis, mainly consider eqs. (2.47) and (2.50), the former when r_b is small, and the electrons have less time to heat up, and the second otherwise. We will also treat eq. (2.51) as an upper bound on the temperature in the low-density limit. However, we want to emphasize that the electron temperature of accretion flow is an area of research in and of itself, and these models should be treated as very rough estimates.

The interstellar and intergalactic media

To use the spherical accretion model for isolated black holes we need the parameters of the surrounding medium. Typically the interstellar medium is considered to be composed of three types of matter: cold hydrogen clouds, warm partly ionized hydrogen and warm fully ionized hydrogen [68, 80, 81]. The temperatures span from $\sim 10^2$ K to 10^6 K and the densities varies between $10^{-3} - 10^2\,\mathrm{cm}^{-3}$. The cold clouds contain the most matter, but only account for around 1% of the interstellar volume, so the other less dense media are more commonly encountered. Some black holes, especially those with high velocities, can escape their galaxy, reducing the density around it further. Typical intergalactic media has densities down to $10^{-6}\,\mathrm{cm}^{-3}$ and temperatures up to 10^7 K [82].

Chapter 3

Scattering processes in dense accretion flows

We will, in this thesis, consider the possible interactions between the axions found in the superradiant clouds and the surrounding plasma that can occur if we assume that the axion has the couplings to photons and electrons described in section 2.1. In this chapter, we will look specifically at interactions with the plasma found in denser accretion flows, where the plasma frequency is much larger than the axion mass. In these, the resonant conversion we will discuss in the next chapter is blocked, and we can treat the interactions as scattering processes of the type

$$e + a \to e + \gamma. \tag{3.1}$$

This process can possibly cause detectable signals by either quenching the superradiant growth or cause a large emission of photons from the system. Quenching is possible if the number rate,

$$\Gamma = -\frac{\dot{n}_a}{n_a}, \tag{3.2}$$

where n_a is the number density of axions, is larger than the superradiant rate. If this is the case, then the axions will turn into photons faster than new axions can be produced, halting the growth of the axion cloud, which could cause gravitational signals or prevent the axion clouds from forming altogether. If the reactions are too ineffective to quench the superradiance, there might still be a large luminosity of photons emitted from the system, which could cause detectable effects. The luminosity of the emitted photons can be calculated from

$$L = \int_D d^3 r Q(r), \tag{3.3}$$

where D is the intersection between the axion cloud and the accretion flow and Q is the volume emission rate of photons.

Assuming that Pauli-blocking and boson-stimulation are negligible, we get the change in axion number from [18, 19]

$$\dot{n}_a = -\int d\Pi_e d\Pi_a f_e(E_e) f_a(E_a) \int d\Pi'_e d\Pi_\gamma |\mathcal{M}|^2 (2\pi)^4 \delta(p_e + p_a - q_\gamma - q_e), \quad (3.4)$$

and the volume emission rate is similarly obtained as

$$Q_\gamma = \int d\Pi_e d\Pi_a f_e(E_e) f_a(E_a) \int d\Pi'_e d\Pi_\gamma E_\gamma |\mathcal{M}|^2 (2\pi)^4 \delta(p_e + p_a - q_\gamma - q_e). \quad (3.5)$$

The notation we use here is p_i and q_i for the four momenta of the initial and final state particles, respectively, where $i = e, a, \gamma$. E_i are the energies of the particles, and bold quantities are the three-momenta. We distinguish between the initial and final electron energy by using E'_e for the latter. $\mathcal{M}$ is the matrix element of the process, f_e and f_a are the phase-space distribution of electrons and axions, respectively, and

$$d\Pi_i = \frac{1}{(2\pi)^3} \frac{d^3 p_i}{2E_i} \quad (3.6)$$

is the Lorentz invariant measure.

There are many references that have done similar calculations to these for the reaction in the opposite direction, $e + \gamma \to e + a$, in the context of studying stellar evolution including axion cooling, for example, Refs. [13–19]. However, their results are not directly applicable in our scenario, since in the opposite direction the axion energies are determined by the thermal photons and will be much larger than the axion mass. The axion can then safely be treated as massless. In our case, we cannot neglect the axion mass since it is an important energy scale when the axions are non-relativistic. Thus, we have to step back and include the axion mass in the matrix elements and axion distribution before estimating the effects the interactions can have on the system.

3.1 Setup and general calculations

In the intersection between the axion cloud and the plasma we have a population of thermal electrons temperature T, which we for the most part will normalize to the electron mass as $\Theta_e = T/m_e$. Since the plasma is relatively hot and non-dense we can neglect any electron degeneracy and the electrons are well described by the Boltzmann distribution

$$f_e(E_e) = 2\exp(-E_e/m_e\Theta_e) \frac{n_e \pi^2}{m_e^3 \Theta_e K_2[\Theta_e^{-1}]}. \quad (3.7)$$

Here $n_e = \int d^3 p_e f_e/(2\pi)^3$ was used to express the distribution in terms of the electron density, n_e, instead of the chemical potential, and K_2 is the modified Bessel function of the second kind. We will consider systems where the gravitational

coupling, α, is small. In these systems, the axions are non-relativistic, and we can treat them to be at rest relative to the plasma electrons since their momentum is $\sim m_a\alpha/2$ [29]. The inclusion of the momentum can then be treated as a higher-order correction in α. With this we can approximate the axion distribution to

$$f_a(p_a) = (2\pi)^3 n_a \delta(\mathbf{p}_a), \tag{3.8}$$

which inserted into the phase space integrals sets $E_a = m_a$ and $\mathbf{p}_a = \mathbf{0}$, and yields a factor $n_a/2m_a$.

We are now interested in calculating the number and emission rate given by eqs. (3.4) and (3.5). These are very similar and we can simplify them simultaneously by considering the integral

$$I = \frac{n_a}{2m_a}\int d\Pi_e f_e(E_e)\int d\Pi'_e d\Pi_\gamma E_\gamma^s |\mathcal{M}|^2 (2\pi)^4 \delta(p_e + (m_a, \mathbf{0}) - q_\gamma - q_e), \tag{3.9}$$

where the phase space integration over the axion distribution has been carried out, and s is introduced to takes us back to $n_a\Gamma$ if $s = 0$ and Q if $s = 1$.

We continue by imposing the four-momenta conservation. Integrating over the momentum of the outgoing electron fixes its three-momentum as $\mathbf{q}_e = \mathbf{p}_e - \mathbf{q}_\gamma$, and the energy becomes $E'_e = \sqrt{E_e^2 + E_\gamma^2 - 2p_e E_\gamma \cos\theta}$, where θ is the angle between the incoming electron and the outgoing photon. The integral can then be written as

$$I = \frac{n_a}{32\pi^2 m_a}\int d\Pi_e f_e(E_e)\int \frac{E_\gamma^{s-1} d^3 q_\gamma}{E'_e} |\mathcal{M}|^2 \delta(E_e + m_a - E'_e - E_\gamma). \tag{3.10}$$

Integrating over the photon angles fixes

$$\cos\theta = \frac{2E_eE_\gamma - 2E_em_a + 2E_\gamma m_a - m_a^2}{2E_\gamma p_e} \Leftrightarrow E_\gamma = \frac{2E_em_a + m_a^2}{2E_e + 2m_a - 2p_e\cos(\theta)} \tag{3.11}$$

through the δ-function, which also yields the factor

$$\left|\frac{d\sqrt{E_e^2 + E_\gamma^2 - 2p_eE_\gamma\cos\theta}}{d\cos\theta}\right|^{-1} = \left(\frac{E_\gamma p_e}{\sqrt{E_e^2 + E_\gamma^2 - 2p_eE_\gamma\cos\theta}}\right)^{-1} = \frac{E'_e}{E_\gamma p_e} \tag{3.12}$$

from the inner function.[1] The integral is then

$$I = \frac{n_a}{16\pi m_a}\int d\Pi_e f_e(E_e)\int dE_\gamma \frac{E_\gamma^s}{p_e}|\mathcal{M}|^2, \tag{3.13}$$

where the limits in E_γ are obtained from eq. (3.11) as

$$E_\gamma = \left[\frac{2E_em_a + m_a^2}{2E_e + 2m_a + 2p_e}, \frac{2E_em_a + m_a^2}{2E_e + 2m_a - 2p_e}\right]. \tag{3.14}$$

[1] $\int f(x)\delta(g(x))dx = f(y)/g'(y)$ if $g(y) = 0$.

Using the electron distribution from eq. (3.7) and introducing the dimensionless quantities $x = E_e/m_e$, $p = \sqrt{x^2-1}$, $\xi = E_\gamma/m_a$ and $\epsilon = m_a/m_e$ we have

$$I = \frac{n_a n_e m_a^s}{32\pi m_e^2}\int_1^\infty dx \frac{\exp(-x/\Theta_e)}{\Theta_e K_2[\Theta_e^{-1}]}\int_{\frac{x+\epsilon/2}{x+\epsilon+p}}^{\frac{x+\epsilon/2}{x+\epsilon-p}} d\xi \xi^s |\mathcal{M}|^2. \tag{3.15}$$

For superradiant growth around astrophysical black holes, which we are interested in, $m_a < 10^{-10}$ eV and so $\epsilon < 10^{-15}$. We can, therefore, safely neglect ϵ when compared to x or ξ. Neglecting ϵ in the integration limits of ξ allows us to switch the order of integration in I through the limit change

$$\left\{1 < x, \xi \in \left[\frac{x}{x+p}, \frac{x}{x-p}\right]\right\} = \left\{0.5 < \xi, \frac{\xi}{\sqrt{2\xi-1}} < x\right\}, \tag{3.16}$$

i.e.

$$I = \frac{n_a n_e m_a^n}{32\pi m_e^2}\int_{1/2}^\infty d\xi \xi^s \int_{\xi/\sqrt{2\xi-1}}^\infty dx \frac{\exp(-x/\Theta_e)}{\Theta_e K_2[\Theta_e^{-1}]}|\mathcal{M}|^2. \tag{3.17}$$

This order will enable us to go further analytically and also extract the spectrum of the emitted photons more easily.

To proceed, we need the matrix element. Process (3.1) has three tree-level contributions. The first we will call the Primakoff channel, where a virtual photon mediates the reaction. The two others are mediated by the electron, and we collectively call these the Compton channel. Figure 3.1 shows the three tree-level Feynman diagrams. The Compton channel requires a spin-flip to produce the photon, this will minimize the interference between the two channels, and we can treat them separately [16]. We can then split the matrix element as $|\mathcal{M}|^2 \approx |\mathcal{M}_P|^2 + |\mathcal{M}_C|^2$. This also allows us to write $\Gamma = \Gamma_P + \Gamma_C$ and $Q = Q_P + Q_C$, where P stands for the Primakoff channel and C for the Compton channel. The next step is to find the matrix elements for the separate channels and, subsequently, determine the individual contributions to the number and emission rates.

3.1.1 The Primakoff channel

In the literature, there are multiple sources for the matrix element for the Primakoff channel, see, for example, Refs. [15–18]. Most of them use the approximation that $m_a \approx 0$, which, as mentioned, is not appropriate for us. The references also include varying cut-offs for the infrared divergence that stems from the massless propagator. The natural choice, used in, for example, Ref. [15], is the plasma frequency. However, it was later seattled in Ref. [16] that the correct cut-off should be the Debye screening, which for a fully ionized hydrogen plasma is

$$\kappa = \sqrt{\frac{8\pi\alpha_{em} n_e}{T}} \approx 5.25\times 10^{-11}\left(\frac{n_e}{1\,\mathrm{cm}^{-3}}\right)^{1/2}\Theta_e^{-1/2}\mathrm{eV}. \tag{3.18}$$

To include the axion mass and this cut-off, we have to find the matrix element from first principles. We do this by applying the normal Feynman algebra to the

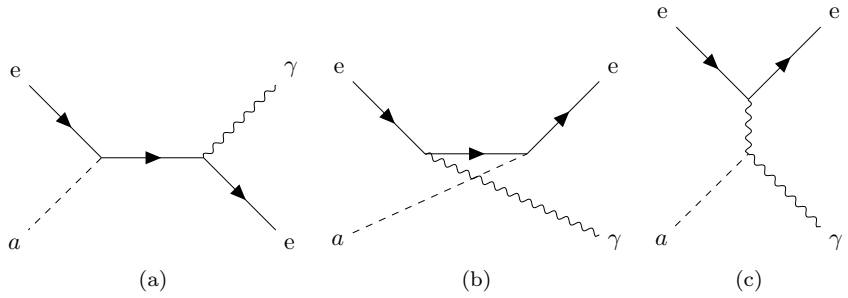

Figure 3.1. All three tree-level diagrams of the process $e + a \to e + \gamma$. Figures 3.1a and 3.1b depicts the two tree-level diagrams of the Compton channel, and figure 3.1c is the only tree-level diagram of the Primakoff channel.

tree-level diagram shown in figure 3.1c. We can then simplify it further by using that we are approximately in the rest frame of the axion. The details are shown in appendix C and the final matrix element, expressed in terms of the dimensionless parameters $x = E_e/m_e$, $\xi = E_\gamma/m_a$ and $\epsilon = m_a/m_e$ from the previous section, is given in eq. (C.7). Following Ref. [16] we include the effective screening factor

$$|F_{eff}|^2 = \frac{|\mathbf{k}|^2}{|\mathbf{k}|^2 + \kappa^2}, \tag{3.19}$$

where $\mathbf{k} = \mathbf{p}_a - \mathbf{q}_\gamma$ is the momentum transfer. This is included in the matrix element through $|\mathcal{M}|^2 \to |\mathcal{M}|^2 |F_{eff}|^2$ and we end at

$$|\mathcal{M}|^2 = \frac{64\pi\alpha_{em} g_{a\gamma}^2 m_e^2 \xi^2}{(2\xi-1)^2(\kappa_a^2+\xi^2)} \left((x^2(2\xi-1)-\xi^2)+ \right.$$
$$\left. \epsilon x\left(3\xi - 2\xi^2 - 1\right) + \epsilon^2\left(\xi^3 - 3/2\xi^2 + \xi - 1/4\right)\right), \tag{3.20}$$

where we also introduced the dimensionless quantity $\kappa_a^2 \equiv \kappa^2/m_a^2$ as well. Since $\epsilon \ll 1$ we only have to concern ourselves with the zeroth-order contribution in ϵ. Inserting this into eq. (3.17) we have

$$I = 2n_a n_e m_a^n \alpha_{em} g_{a\gamma}^2 \int_{1/2}^{\infty} d\xi \frac{\xi^{2+s}}{(2\xi-1)^2(\kappa_a^2+\xi^2)} X(\xi, \Theta_e), \tag{3.21}$$

where $X(\xi, \Theta_e)$ is the integral over x. This integral can be evaluated analytically to

$$X(\xi,\Theta_e) = \int_{\xi/\sqrt{2\xi-1}}^{\infty} dx \frac{\exp(-x/\Theta_e)}{\Theta_e K_2[\Theta_e^{-1}]}\left(x^2(2\xi-1)-\xi^2\right)$$
$$= \frac{2\Theta_e}{K[\Theta_e^{-1}]}\exp\left(-\frac{\xi}{\Theta_e\sqrt{2\xi-1}}\right)\left(\Theta_e(2\xi-1)+\xi\sqrt{2\xi-1}\right), \tag{3.22}$$

and we end at

$$I = \frac{4n_a n_e m_a^n \alpha_{em} g_{a\gamma}^2 \Theta_e}{K_2[\Theta_e^{-1}]} \int_{1/2}^{\infty} d\xi \frac{\xi^{2+s}\left(\Theta_e(2\xi-1)+\xi\sqrt{2\xi-1}\right)\exp\left(-\frac{\xi}{\Theta_e\sqrt{2\xi-1}}\right)}{(2\xi-1)^2(\kappa_a^2+\xi^2)}. \tag{3.23}$$

If $\kappa \gg m_a$, which is the case for most systems of interest in this chapter, we have that $\xi^2/\kappa_a^2 \ll 1$ since ξ is supressed by the exponential for all but the most extreme temperatures. We can then write the number rate as

$$\Gamma_P = \frac{\alpha_{em} g_{a\gamma}^2 n_e m_a^2}{\kappa^2} F_P(\Theta_e) = \frac{g_{a\gamma}^2 m_a^2}{8\pi} \Theta_e F_P(\Theta_e), \tag{3.24}$$

where $\Theta_e F_P(\Theta_e)$ contain the full temperature dependence. From this we have that the rates are essentially independent of the electron density. This can be confirmed numerically, and we found that the rates change with n_e only when both $\Theta_e > 1$ and $n_e < 10^2$ cm^{-3}. This corresponds to environments not encountered in this chapter.

3.1.2 The Compton channel

As for the Primakoff channel, there are multiple sources for the Compton matrix element, but many use the approximation $m_a \approx 0$. To get the matrix element we do the Feynman algebra in appendix C and the final expression for the matrix element, expressed in terms of the dimensionless parameters x, ξ, and ϵ, becomes

$$|\mathcal{M}|^2 = \frac{16\pi\alpha_{em} g_{ae}^2 \epsilon^2}{(2x+\epsilon)(2x-2\epsilon\xi+\epsilon)}\left(1+2\xi^2-2\xi+\frac{4\xi^2}{(2x+\epsilon)(2x-2\epsilon\xi+\epsilon)}\right). \tag{3.25}$$

To first order in ϵ, this can be simplified to

$$|\mathcal{M}|^2 = \frac{4\pi\alpha_{em} g_{ae}^2 \epsilon^2}{x^2}\left(1+2\xi^2-2\xi+\frac{\xi^2}{x^2}\right). \tag{3.26}$$

Inserting this matrix element into eq. (3.17) we find

$$I = \frac{\alpha_{em} g_{ae}^2 n_a n_e m_a^{s+2}}{8m_e^4} \int_{1/2}^{\infty} d\xi \xi^s \int_{\xi/\sqrt{2\xi-1}}^{\infty} dx \frac{\exp(-x/\Theta_e)}{\Theta_e K_2[\Theta_e^{-1}]}\left(\frac{1+2\xi^2-2\xi}{x^2}+\frac{\xi^2}{x^4}\right). \tag{3.27}$$

The general behavior of the Compton number rate is then described by

$$\Gamma_C = \frac{\alpha_{em} g_{ae}^2 n_e m_a^2}{m_e^4} F_C(\Theta_e), \tag{3.28}$$

where F_C is the temperature dependent integral.

3.2 Quenching the superradiant instability

The interactions with the plasma can quench the superradiant instability if $\Gamma_P + \Gamma_C \approx \Gamma_{011}$. We get the number rates by setting $s = 0$ and divide by n_a in eqs. (3.23) and (3.27). However, before we compare these with the superradiant exponent, Γ_{011}, we want to compare them with each other. The most important differences between the two channels are described by eqs. (3.24) and (3.28), and assuming that the temperature dependent integrals in these expressions are of the same order, we have

$$\frac{\Gamma_P}{\Gamma_C} \approx \frac{g_{a\gamma}^2 m_e^2}{\kappa^2 g_{ae}^2 / m_e^2}. \tag{3.29}$$

With the upper bounds on $g_{a\gamma}$ and g_{ae}, given in eqs. (2.6) and (2.7) respectively, we have that $g_{a\gamma} \approx g_{ae}/m_e$. With this, $\Gamma_P \gg \Gamma_C$ when $\kappa \ll m_e$, which is the case for most astrophysical plasma. This allows us to neglect the Compton channel and use $\Gamma \approx \Gamma_P$. This is fully supported by figure 3.2, where both number rates are calculated numerically using the full expressions and plotted vs. the temperature. In the figure $n_e = 1 \times 10^{20}\,\mathrm{cm}^{-3}$ was used, this corresponds to a realistic maximum for the electron density, which should favor Γ_C, but we see that Γ_P still dominates for all temperatures.

In order to quench the instability, we then want $\Gamma_P \approx \Gamma_{011}$. We see in figure 3.2 that Γ_P reaches a maximum of around $10^{-33}\mathrm{s}^{-1}$ for the very high temperatures of $\Theta_e \sim 10$. This rate corresponds to characteristic time scales far larger than the age of the universe, $t_0 \approx 4 \times 10^{17}\,\mathrm{s}$. Even though we theoretically can have a system where α and M yield $\Gamma_{011} < \Gamma_P$, this would also mean that $\Gamma_{011} \ll t_0^{-1}$, and the slow growth of the superradiant instability in this case would make the quenching irrelevant and completely undetectable. We can therefore conclude that dense accretion flows cannot quench the instability in any system of observational relevance.

3.3 Electromagnetic signals

Even though the interaction with the accreted matter cannot quench the instability, it might still yield a significant electromagnetic signal, even if only a small portion of the cloud converts into photons. Since the instability, if not quenched, yields immense populations of axions, see eq. (2.32), which can compensate for the low probability of photon emission. The total luminosity is given by eq. (3.3), where the integration should be done over the intersection between the cloud and the accretion flow. Since Q and Γ have the same dependence on each parameter, we can neglect the Compton channel compared to the Primakoff here as well. We can

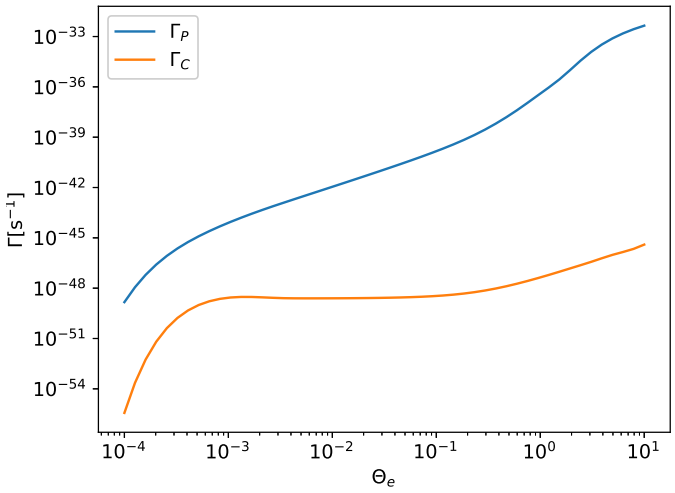

Figure 3.2. The temperature dependenc of Γ_P and Γ_C. The number rates are calculated from $\Gamma = I|_{s=0}/n_a$ using the expressions (3.23) and (3.27), respectively. The electron density and axion mass are fixed as $n_e = 10^{20}\text{cm}^{-3}$ and $m_a = 10^{-10}$ eV. Here we see that the Primakoff rate dominates for all relevant temperatures.

then approximate the total volume emission rate as

$$Q = Q_P = \frac{4 n_a n_e m_a \alpha_{em} g_{a\gamma}^2 \Theta_e}{K_2[\Theta_e^{-1}]} \int_{1/2}^{\infty} d\xi \frac{\xi^3 \left(\Theta_e(2\xi - 1) + \xi\sqrt{2\xi - 1}\right) \exp\left(-\frac{\xi}{\Theta_e\sqrt{2\xi-1}}\right)}{(2\xi - 1)^2(\kappa_a^2 + \xi^2)}. \tag{3.30}$$

As for Γ_P, we have that for low temperatures Q_P is essentially independent of the electron density and the most complicated dependence is that of the temperature.

In what follows, we will investigate the luminosity emitted from the two benchmark models described in section 2.4, the accretion disk and spherical accretion. The disk represents the dense but cold limit, while spherical accretion is the hot and non-dense limit of accretion. We note that an accretion disk will not be surrounded by completely empty space. Thus, typical luminosity from a system hosting a disk will be more akin to a slightly reduced sum of the luminosity from spherical accretion and a disk.

Note that in the coming numerical calculations, we have fixed $g_{a\gamma}$ at the unrestricted maximum from eq. (2.6) to give an estimate of the magnitudes involved. We will discuss the role of $g_{a\gamma}$ in more detail in chapter 5.

3.3.1 Accretion disks

In this section we will explore the luminosity emitted from the Novikov–Thorne disk described in appendix B. This is a thin disk of height $h(r)$, with an inner edge at the ISCO. The height of the disk is much smaller than the characteristic size of the axion cloud, $h \ll \Delta r_{cl}$, as is illustrated in figure 3.3. The disk will, therefore, determine the geometry of the intersection, and a reasonable approximation is to treat the disk as fully located in the $\theta = \pi/2$ plane. Thus, we have

$$L_{disk} \approx 2\pi r_g^2 \int_{r_{ISCO}}^{\infty} dr r h(r) Q_P(T(r), n_e(r), n_a(r, \theta = \pi/2)), \tag{3.31}$$

where we will use the axion distribution described in eq. (2.26) and we assume that the accreted matter is fully ionized so that $n_e(r) = n(r)$.

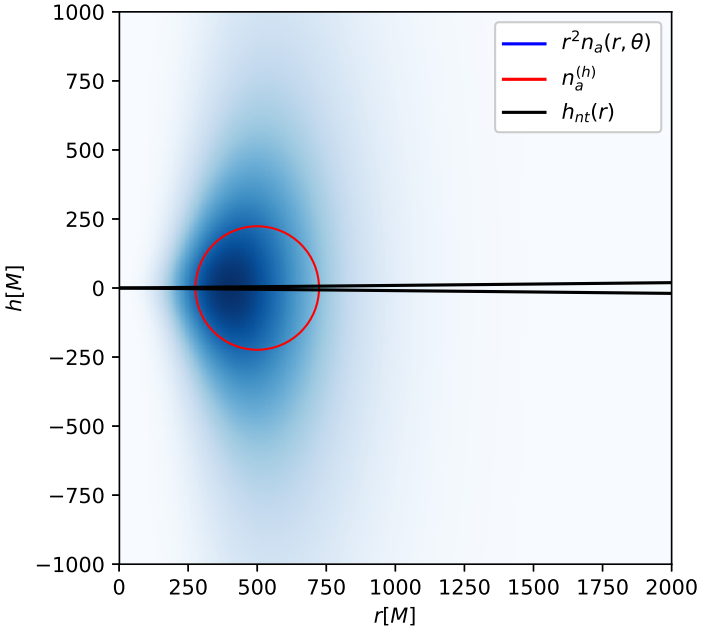

Figure 3.3. A representation of the geometry of the disk and axion cloud. The blue is the axion density from eq. (2.26) weighted by r^2, the opacity corresponds to the density. The red circle represents the torus where the homogeneous axion cloud approximation from eq. (2.32) is valid. The black lines are the edges of the Novikov–Thorne disk from appendix B. The parameters used for the plot are $M = 10 M_\odot$, $\alpha = 0.1$, $a = 0.9$, $\alpha_p = 0.1$ and $\dot{m} = 0.1$.

The full parameter space for this model is α, M, a, f, $\dot{m}$ and α_p. However, as we mentioned in the background, $\alpha_p = 0.1$ is usually fixed without further investigation. We also have that L is directly proportional to f, so we know exactly how it affects the luminosity. However, $f \sim 0.1$ can only be reached with the more efficient couplings of larger α, so one should be critical about the choice of f.

When it comes to $\dot{m}$, we have that the temperature, density, and height of the disk all are proportional to $\dot{m}^p$ for $p > 0$. We should, therefore, expect that higher accretion rates should yield larger luminosities. A relatively small span of $\dot{m}$ can support an accretion disk, $\dot{m} \approx 0.01 - 1$, so we should only see minor changes due to the rate. The luminosity depends on the spin, a, mainly through the location of the ISCO. The ISCO decrease with higher spin, which extends the disk further towards the black hole. This extension allows for more interaction with a hotter surrounding which should increase the luminosity.

The two most important parameters are M and α. The exact dependence of α is complicated because of n_a, but we have that $n_a \propto \alpha^7/M$, so we should expect a high sensitivity to α. When it comes to the black hole mass, it mainly scales the geometry and the number of axions in the cloud. The volume of an accretion disk is almost two dimensional, $V = M^2 h$, where $h < 0.1M$ at the axion cloud for most α. Then with $Q_P \propto m_a^3 = \alpha^3/M^3$ we have the very rough dependence

$$L_{disk} \propto \frac{\alpha^{10}}{M^2} h(r_{cl}). \tag{3.32}$$

Therefore, the luminosity should be roughly inversely proportional to the mass and very sensitive to changes in α.

We investigate the parameter space numerically in figures 3.4a and 3.4b, where the luminosity is plotted against α and M, respectively. In the two plots we also display the dependence on $\dot{m}$ and a by showing the luminosity for $\dot{m} = 0.01$ and $\dot{m} = 1$, as well as for $a = 0.1M$ and $a = 0.99M$. From these figures, we see that the predicted dependencies are roughly correct. We can essentially conclude that a small and rapidly spinning black hole with a strong coupling to the axion yield the largest luminosity. Numerical values for "typical" stellar and supermassive black holes, as well as some best possible values, are given in table 3.1 compared with the same from the spherical accretion model studied in the next section.

3.3.2 Spherical accretion

For spherical accretion, the axion cloud determines the geometry. The simplest and most accurate approximation is, therefore, to integrate over all of space down to the event horizon, r_+, i.e.,

$$L_{sphere} \approx 2\pi r_g^3 \int_{r_+}^{\infty} r^2 dr \int_0^{\pi} \sin\theta d\theta Q_P(T(r), n_e(r), n_a(r,\theta)). \tag{3.33}$$

For the electron density, we use model (2.43) and assume fully ionized hydrogen, and for the temperature, model (2.50) is used. Compared to the accretion disk,

where we had that the luminosity follows eq. (3.32), we have here that the volume of the intersection scales as M^3 and we should expect that

$$L_{sphere} \propto \frac{\alpha^{10}}{M} \tag{3.34}$$

instead. The simple temperature model of eq. (2.50) is independent of the mass and $L \propto M^{-1}$ should, therefore, be followed more closely compared to the disk. We should, therefore, still expect that smaller black holes should yield larger luminosities. However, the temperature is much larger than for the disk, so the claim that Q_P is independent of n_e might no longer hold since κ will be smaller than in the disk. If it is small enough to impact the luminosity, we will see this when $\dot{m}$ is varied. We should also expect the effect to be more noticeable for large α since that puts the cloud closer to the black hole, effectively raising the temperatures where most of the emission occurs. Higher spin should also increase the luminosity since in this model, the only thing affected by a is the ISCO, and a larger ISCO will lead to a larger area of high temperatures close to the black hole.

M and α are the parameters of most interest for this model as well and in figures 3.4c and 3.4d the luminosity is plotted vs α and M, respectively, for two different accretion rates, $\dot{m} = 10^{-8}$ and $\dot{m} = 10^{-4}$, and two spins, $a = 0.1M$ and $a = 0.99M$. Note that the accretion rates are much lower than those from the disk but still larger than the most extreme values that can be reached around isolated black holes, see eq. (2.40). In the figures, we see that the luminosity is essentially independent of $\dot{m}$ even though the temperature is much higher than in the disk. We also see the expected effect of increased spin, where the smaller ISCO greatly increases the total luminosity. Overall, we get that a fast spinning and small black hole yield the largest luminosities for spherical accretion. In table 3.1, "typical" and best possible values of the luminosity are provided, compared to those estimated from the disk model, to give a clearer sense of the magnitudes involved.

Table 3.1. Luminosity for different systems. The typical values correspond to parameters found more commonly in nature, whereas the best is for the most favorable but still realistic situations. The typical parameters are chosen as $\alpha = 0.1$, $a = 0.9M$, and $f = 0.01$, with $\dot{m} = 0.1$ for the disk and $\dot{m} = 10^{-6}$ for spherical accretion. The typical masses are set to $10M_\odot$ for stellar black holes and $10^7 M_\odot$ for SMBHs. The best parameters are chosen as $\alpha = 0.4$, $a = 0.99M$, and $f = 0.1$, with $\dot{m} = 1$ for the disk and $\dot{m} = 10^{-3}$ for spherical accretion. The most favorable masses are set to $3M_\odot$ for stellar black holes and $10^5 M_\odot$ for SMBHs.

	Stellar, disk	Stellar, sphere	SMBH, disk	SMBH, sphere
Typical	2×10^{-4} W	5×10^{5} W	2×10^{-19} W	0.1 W
Best	1×10^{2} W	1×10^{14} W	3×10^{-6} W	3×10^{9} W

3.3.3 Emitted spectra

In addition to the luminosity, we can also determine the spectrum of the emitted photons, which is important when considering the detectability of the signal.

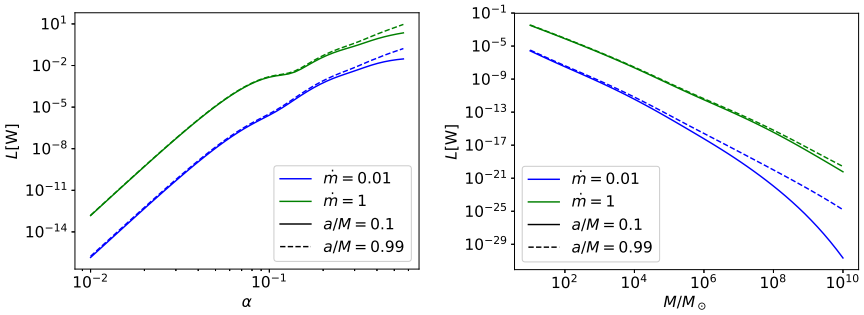

(a) Luminosity vs. α for an accretion disk. (b) Luminosity vs. M for an accretion disk.

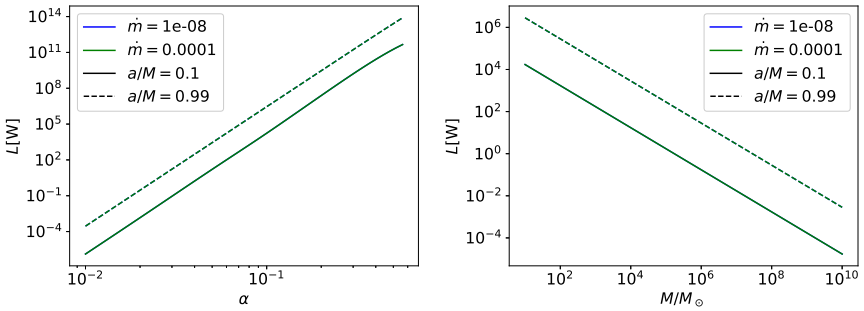

(c) Luminosity vs. α for spherical accretion. (d) Luminosity vs. M for spherical accretion.

Figure 3.4. The luminosity emitted from an accretion disk and spherical accretion plotted vs. α and M, respectively. In each figure, four plots are shown each calculated with different spin and accretion rate. In figures 3.4a and 3.4c $M = 10M_\odot$, while in figures 3.4b and 3.4d $\alpha = 0.1$. The assumed mass fraction of the axion cloud is $f = 0.01$ in all figures.

Setting $s = 1$ in (3.23) we get the spectrum from

$$F_\nu(\xi) \equiv \int_D d^3r \frac{dQ_P}{dE_\gamma}$$
$$= \int_D d^3r \frac{4n_a n_e \alpha_{em} g_{a\gamma}^2 \Theta_e}{K_2[\Theta_e^{-1}]} \frac{\xi^3 \left(\Theta_e(2\xi-1) + \xi\sqrt{2\xi-1}\right) \exp\left(-\frac{\xi}{\Theta_e\sqrt{2\xi-1}}\right)}{(2\xi-1)^2(\kappa_a^2+\xi^2)}, \quad (3.35)$$

where the volume integration is over the same geometries as for the luminosity. $\nu = E_\gamma = m_a\xi$ is the frequency of the photons and $F_\nu(\xi)d\xi$ is the total power emitted from the system in the frequency band $[\nu, \nu + d\nu] = [m_a\xi, m_a(\xi + d\xi)]$. The shape of the spectrum emitted from a black hole of $M = 3M_\odot$, calculated for different values of α, is given in figure 3.5 for both the accretion disk and spherical accretion model.

The spectrum is relatively independent of all parameters except for α, especially for the disk. The magnitude is only slightly affected by the spin of the black hole. The independence of the black hole mass can be explained by the fact that we differentiate with respect to E_γ, which is proportional to $m_a \propto M^{-1}$. The differentiation will, therefore, remove the dependence of M, since $L \propto M^{-1}$, roughly, in both models. However, we have to note that we have normalized the frequency to m_a, and the actual frequencies of the spectrum will be inversely proportional to M.

The shape of the spectrum from the disk is a very narrow peak at $E_\gamma = m_a$ with only a slight change in magnitude with increasing α. The spectrum from spherical accretion has a more complicated behavior. For small α, it resembles the disk spectrum with a dominant peak at m_a. However, when α increases, a large part of the emission occurs closer to the black hole where the electrons are more energetic, leading to more energetic photons and a significant contribution at higher frequencies. We see a rise to a broad peak at larger frequencies of around $10^3 m_a$ before the emission drops down again.

With estimates for the luminosity and a picture of the shape of the spectrum, the question now is whether we can detect and use these signals to search for imprints from the axion. We discuss this in chapter 5 since most of the discussion is relevant for the results from the next chapter as well.

3.4 Plasma frequency suppression and temperature sensitivity

We end this chapter by highlighting two important uncertainties which could affect the results.

In figure 3.5 we see that a significant amount of the emission occur at frequencies close to m_a. In these denser accretion flows, this corresponds to frequencies far below the plasma frequency $\omega_{pl} \approx 3 \times 10^{-11}\,\mathrm{eV}\sqrt{n_e/1\,\mathrm{cm}^{-3}}$. We expected that the plasma frequency should have blocked this emission more. A possible reason why we do not see this suppression is that we treat the emitted photon in the kinematics of section 3.1 as fully massless. One could do the kinematics and assume $q_\gamma^2 = \omega_{pl}^2$, this would reduce the luminosity greatly since we would effectively integrate from ω_{pl} in expressions (3.30) and (3.35) instead of 1/2. However, since the plasma frequency is not a real mass, this will not be completely correct either, and a more detailed analysis has to be made.

Another uncertainty in our analysis is that of the electron temperature of spherical accretion. Through the spin dependence, we saw that the luminosity is sensitive to the temperature close to the black hole. However, it is not clear if a more realistic temperature model would increase or decrease the total luminosity.

We will find in chapter 5 that the luminosities we estimated in this chapter are borderline significant as they are, and we can keep these uncertainties in mind by treating the signals as upper bounds to the actual emission.

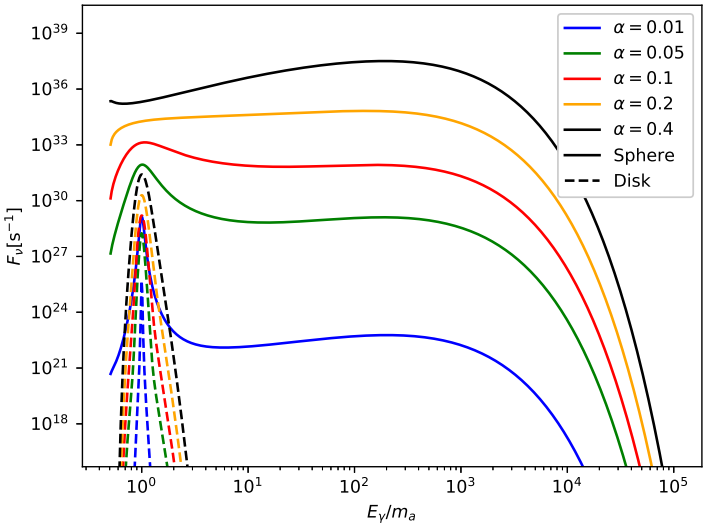

Figure 3.5. The spectra, the power emitted per frequency from the system, for spherical accretion, full lines, and the accretion disk, dashed lines, calculated for different values of α. The remaining parameters are set as $M = 3M_\odot$, $a = 0.99M$, $f = 0.01$, in both models. The accretion rates are $\dot{m} = 1$ for the disk and $\dot{m} = 10^{-5}$ for the spherical accretion. Note that the peaks only align because of the scaling by m_a of the x-axis. $\alpha = 0.1$ corresponds to $m_a = 4 \times 10^{-12}\,\mathrm{eV}$, which, if directly converted, yields a photon of frequency $\sim 1\,\mathrm{kHz}$. To get numerical values in more conventional units, $\mathrm{W\,Hz^{-1}}$, one has to multiply by h, putting the highest values of around $10^3\,\mathrm{W\,Hz^{-1}}$.

Chapter 4

Resonant conversion in spherical accretion

In the analysis of the previous chapter, we saw that the emission rate was, for the most part, essentially independent of the density of the accretion flow. This breaks down if the density is low enough that the plasma frequency, given by

$$\omega_{pl} \approx \left(\frac{4\pi\alpha_{em} n_e}{m_e} \right)^{1/2}, \tag{4.1}$$

is comparable to the axion mass. If this is the case, resonant conversion of axions can occur since the mass difference no longer blocks the conversion. The accretion rates considered in the previous chapter were always high enough that $\omega_{pl} \gg m_a$ throughout the flow. However, there are situations when it is possible to have densities low enough that $\omega_{pl} \approx m_a$ in regions overlapping with the axion cloud. For example, high-velocity black holes can experience a significantly reduced accretion rate, as accounted for in the model of section 2.4.2. Another example is supernova remnants which are left in an under-density after the explosion. We will, in this chapter, consider the first scenario: isolated black holes traveling fast through interstellar or intergalactic space, reducing the density low enough that resonant conversion of axions can have significant effects on the system.

The scattering formalism we used in the previous chapter is not able to capture resonant conversion because the inclusion of κ we used from Ref. [16] does assume that $\omega_{pl} \gg m_a$. Resonant conversion is instead best described by the modified Maxwell's equations [83], which allows axions to mix with photons when traveling through a external magnetic field. The formalism for studying this mixing was developed quite early in Ref. [84], and applications of it can be found in Refs. [48, 85] in the context of DM-axions in the vicinity of neutron stars. This situation is quite similar to our situation, with an axion cloud interacting with the magnetic field suspended in the astrophysical plasma. The main difference is that we have much

smaller magnetic fields, but this is compensated by the much larger densities found in superradiant axion clouds. We will, therefore, in this chapter apply the methods from Refs. [48, 84] to study the resonant conversion in the overlap between the superradiant axion clouds and low-density spherical accretion.

4.1 Emitted power through resonant conversion

In this section we relay the important results from Ref. [48] in the new context of superradiant axion clouds.

With the existence of the axion-photon coupling, given in eq. (2.2), Maxwell's equations for the electromagnetic field have to be modified. The modification allows axions and photons to mix in the presence of an external magnetic field. Assuming radial planar waves of the form

$$a(r,t) = \mathrm{i}e^{\mathrm{i}\omega t - \mathrm{i}kr}\tilde{a}(r) \text{ and } A_{\parallel}(r,t) = e^{\mathrm{i}\omega t - \mathrm{i}kr}\tilde{A}_{\parallel}(r), \tag{4.2}$$

where a is the axion field, and $A_{\parallel}$ is the photon component transverse to the direction of propagation and co-planar with the magnetic field, one can show, see appendix D for more details, that Maxwell's equations reduce down to the mixing equation

$$\left[-\mathrm{i}\frac{d}{dr} + \frac{1}{2k}\begin{pmatrix} m_a^2 - \xi\omega_{pl}^2 & \Delta_B \\ \Delta_B & 0 \end{pmatrix}\right]\begin{pmatrix} \tilde{A}_{\parallel} \\ \tilde{a} \end{pmatrix} = 0. \tag{4.3}$$

The quantities ξ and Δ_B are related to the angle θ between the direction of motion and the external magnetic field strength, B, according to

$$\xi = \frac{\sin^2\tilde{\theta}}{1 - \frac{\omega_{pl}^2}{\omega^2}\cos^2\tilde{\theta}} \text{ and } \Delta_B = Bg_{a\gamma}m_a\frac{\xi}{\sin\theta}. \tag{4.4}$$

Equation (4.3) is valid close to the resonance radius, r_c, which is where the axion mass coincide with the plasma frequency, i.e., where

$$\omega_{pl}(r_c) = \omega \approx m_a. \tag{4.5}$$

Through perturbation analysis, Ref. [48] provides the following formula for the transition rate at radius r:

$$p_{a\gamma} = \left|\int_0^r dr' \frac{B(r')\xi(r')g_{a\gamma}}{2v_c\sin\tilde{\theta}} \exp\left(\frac{-\mathrm{i}\int_0^{r'} d\tilde{r}\left[m_a^2 - \xi(\tilde{r})\omega_{pl}^2(\tilde{r})\right]}{2m_a v_c}\right)\right|^2, \tag{4.6}$$

where v_c is the axion velocity. Taking $r \to \infty$ and using the method of stationary phase, the previous expression simplifies to

$$p_{a\gamma}^{\infty} = v_c \lim_{r-\infty} p_{a\gamma}(r) \approx \frac{1}{2v_c}g_{a\gamma}^2 B(r_c)^2 l^2, \tag{4.7}$$

where

$$l = \sqrt{\frac{2\pi r_c M v_c}{3 m_a}} \tag{4.8}$$

is the effective size of the conversion area. The additional factor of v_c in this expression comes from considering the effect the changing plasma frequency has on the frequency of the outgoing photons far from r_c where the mixing becomes negligible, see Ref. [48] for the details. The expression in eq. (4.7) holds for any θ to first order in v_c. For the axion cloud, $v_c \approx \alpha/2$ and the expression can be treated as the first-order approximation in α. Using this, the radiated power through a solid angle $d\Omega$ at r_c is

$$\frac{d\mathcal{P}}{d\Omega} \approx 2 p_{a\gamma}^{\infty} \rho_a(r_c) v_c r_c^2 M^2, \tag{4.9}$$

where we have normalized r_c to $r_g = M$ which results in the factor M^2. The factor of 2 comes from the fact that the conversion can come from movement inwards and outwards from the black hole. Note that in the previous chapter, we used the luminosity L, while here we use a different notation with $d\mathcal{P}/d\Omega$ to resemble the source material. Integrating the latter over the angles results in the former.

Formulas (4.7) and (4.9) are readily applicable to the superradiant axion cloud. We can rewrite it in terms of α, using $m_a M = \alpha$ and $v_c \approx \alpha/2$, and get

$$\frac{d\mathcal{P}}{d\Omega} \approx \frac{\pi}{3} g_{a\gamma}^2 B(r_c)^2 \alpha M^3 r_c^3 n_a(r_c). \tag{4.10}$$

Resonance conversion is only relevant in spherical accretion since the density is far abvove 1 cm^{-3} in accretion disks. In spherical accretion B and r_c are spherically symmetrical but we do have an angular dependence in n_a. To simplify the calculations we average the density from eq. (2.26) over the sphere at r_c and get

$$n_a(r_c) \approx \frac{f\alpha^7}{96\pi M} \exp\!\left(-\alpha^2 r_c\right) \left(3 - \alpha^2 r_c + \frac{\alpha^4}{4} r_c^2 + 2\alpha^2 r_c^2\right) \equiv \frac{f\alpha^7}{96\pi M} g(r_c). \tag{4.11}$$

Inserting this we get the radiated power

$$\frac{d\mathcal{P}}{d\Omega} = \frac{f}{288} M^2 \alpha^8 g_{a\gamma}^2 B(r_c)^2 r_c^3 g(r_c), \tag{4.12}$$

which in watt yields

$$\frac{d\mathcal{P}}{d\Omega} \approx 1.5 \times 10^{21} \left(\frac{f}{0.01}\right) \left(\frac{M}{M_\odot}\right)^2 \left(\frac{g_{a\gamma}}{0.66 \times 10^{-19}\,\mathrm{eV}^{-1}}\right)^2 \left(\frac{B(r_c)}{1\,\mathrm{mG}}\right)^2 \alpha^8 r_c^3 g(r_c)\,\mathrm{W}, \tag{4.13}$$

and so it has the potential to be substantial.

4.2 The resonance condition

Formula (4.12) is dependent on the radius r_c where the plasma frequency coincides with the axion mass. This is the resonance radius, and it is the most important quantity of this chapter. For resonant conversion to occur r_c must exist and the total luminosity is highly sensitive to its location relative to the axion cloud. The resonance radius is determined from its definition,

$$\omega_{pl} = \sqrt{\frac{4\pi\alpha_{em} n_e(r_c)}{m_e}} = m_a, \tag{4.14}$$

and does only depend on the electron density of the accretion flow. It is therefore useful to introduce

$$m_1 \equiv \sqrt{\frac{4\pi\alpha_{em} \times 1\,\mathrm{cm}^{-3}}{m_e}} = 3.71 \times 10^{-11}\,\mathrm{eV}, \tag{4.15}$$

which is the plasma frequency corresponding to a density of $n_e = 1\,\mathrm{cm}^{-3}$. We see that this is comparable to the axion mass we have in the superradiant clouds around stellar black holes, which means that we will require very low densities in the accretion flow for resonant conversion to be relevant. We can already conclude that we will not see resonant conversion around SMBHs since superradiant axion clouds around those require masses much smaller than m_1. These low electron densities are found throughout the galaxy but for resonant conversion to yield large luminosities we need low densities close to the black hole. The lowest densities are achieved around isolated black holes that travels rapidly through space, as described in section 2.4.2, and this chapter will, therefore, focus on these systems.

Inserting the electron density model from eq. (2.44) into eq. (4.14), we can extract the resonance radius as a function of the ambient electron density, $n_{e,\infty}$, and the Bondi radius, r_b, as

$$\begin{aligned} r_c &= 4^{-2/3} \left(\frac{n_{e,\infty}}{1\,\mathrm{cm}^{-3}}\right)^{2/3} \left(\frac{m_1}{m_a}\right)^{4/3} r_b \\ &\approx 0.072 \left(\frac{n_{e,\infty}}{1\,\mathrm{cm}^{-3}}\right)^{2/3} \left(\frac{M}{M_\odot}\right)^{4/3} \alpha^{-4/3} r_b. \end{aligned} \tag{4.16}$$

From this, we get a condition on the system for where resonance conversion can occur from the fact that $r_c < r_b$ must be satisfied. The density model is only valid in that region, and $r_c > r_b$ means that the system requires lower electron densities than the ambient density. From this the resonance condition can be expressed as

$$\left(\frac{n_{e,\infty}}{1\,\mathrm{cm}^{-3}}\right) < 4 \left(\frac{m_a}{m_1}\right)^2 \Leftrightarrow \left(\frac{n_{e,\infty}}{1\,\mathrm{cm}^{-3}}\right) < 51.8 \left(\frac{M}{M_\odot}\right)^{-2} \alpha^2, \tag{4.17}$$

which essentially describes for which systems the axion mass is larger than the ambient plasma frequency. In figure 4.1 we have plotted the (α, M) plane where this

condition is satisfied for some different ambient densities. Since we want $\alpha \sim 0.1$, it is clear from this figure that we have to consider black holes for which $M \lesssim 10 M_\odot$ and $n_{e,\infty} < 0.01\text{cm}^{-3}$.

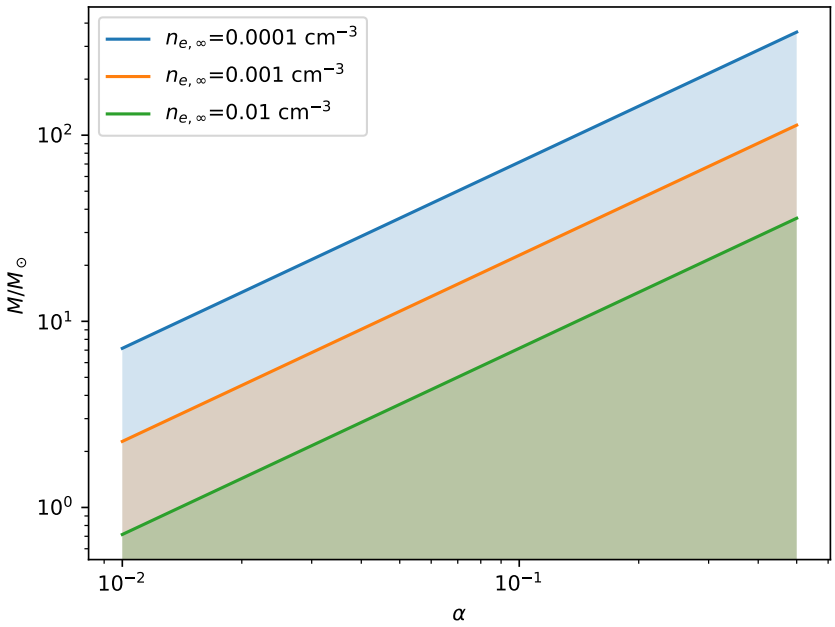

Figure 4.1. Systems where $r_c < r_b$ as described by eq. (4.17), visualized for a couple of ambient densities. The shaded areas are (α, M)-pairings for which resonant conversion of axions into photons can occur. Essentially where the ambient plasma frequency is less than the mass of the superradiant axions.

For the brightest emission we want as large axion density as possible at r_c. The most optimal case is, therefore, when $r_c \approx r_{cl} \approx 1/\alpha^2$. Since $r_c = x r_b$ where $x < 1$, we have that

$$\alpha \approx x^{-1/2} v_{eff} \Rightarrow v_{eff} \lesssim \alpha \tag{4.18}$$

would yield the largest signals. We can see from this that we want v_{eff} to be large, preferably comparable to α. This is not a perfect analysis since x depends on α. As mentioned in the background, it is possible for black holes to reach velocities up to $v_{eff} = 0.017$, resulting from black hole mergers, which is comparable to the smaller values of α. However, more common velocities are around $v_{eff} \approx 10^{-5} - 10^{-3}$. We will explore exactly how important the condition $v_{aff} \approx \alpha$ is for the radiated power in the next section, together with its dependence on all the other parameters.

4.3 Exploring the parameter space

In this section, we will explore how the radiated power from eq. (4.12) depends on the different parameters in order to identify the systems in which a significant signal can be achieved. Throughout, we will assume that the axion cloud has a mass of 1% of the black hole mass, i.e. $f = 0.01$, and use the magnetic field model from eq. (2.46) unless otherwise stated. We will also use the upper bound on $g_{a\gamma}$ from eq. (2.6) to give the largest possible signals. We will discuss the role of the coupling in more detail in the next chapter.

We argued in the previous section that we are interested in large velocities, much larger than the sound speed of the ambient medium. We will therefore assume $v_{eff} \approx v_{rel}$ and disregard the sound speed. The sound speed was also the only thing dependent of the ambient temperature, T_∞, so when calculating the radiated power from eq. (4.12) it seems that we can neglect the temperature completely. However, there is a large caveat to this which we will discuss at the end of this section.

We plot the radiated power vs. all the relevant parameters below, but before that, we want to note two things that are relevant for all plots. First, we set a lower limit on radiated power at 1 W, this makes the plots easier to read, and lower signals are of no interest to us. This will sometimes result in some labeled graphs not showing up in the figures. They are still included since the fact that they yield neglectable signals are important for the discussion. Secondly, the graphs are sometimes cut-off, seemingly arbitrary. This cut-off comes from imposing the condition $r_c < r_b$. Otherwise, the models would interpolate outside the region where they are valid.

Black hole mass and gravitational coupling: From figure 4.1, we saw that resonant conversion is only relevant for black holes with mass $\lesssim 10M_\odot$ if $\alpha \sim 0.1$, which is required for the instability to yield large axion densities. However, because of the complicated dependence on r_c and α in eq. (4.12) it is unclear what (M, α)-pairings yield the highest luminosity. We, therefore, plot the radiated power vs. α for fixed mass in figure 4.2, and vice versa in figure 4.3. In these figures we use three different ambient densities 10^{-2}, 10^{-3}, and 10^{-4} cm^{-3} and held $v_{eff} = 0.01$ fixed.

We see from the figures that the luminosity can reach up to 10^{25} W when α is large and M is small. The luminosity quickly drops of when M increase above $10M_\odot$ but for all masses below that limit we can have significant signals. The luminosity seems to be less sensitive to α since we can have signals almost as high as 10^{20} W all the way down to $\alpha \approx 0.01$. Thus, a small black hole with moderate coupling to the axion is required for resonant conversion to be relevant.

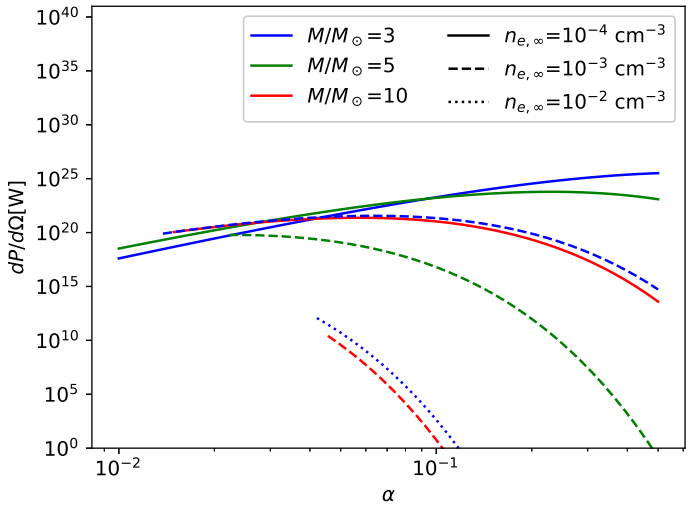

Figure 4.2. The radiated power vs. α for different pairings of black hole mass and ambient density. We only consider α in range where superradiance is relevant, see condition (2.24). The relative velocity used here is $v_{rel} = 0.01$.

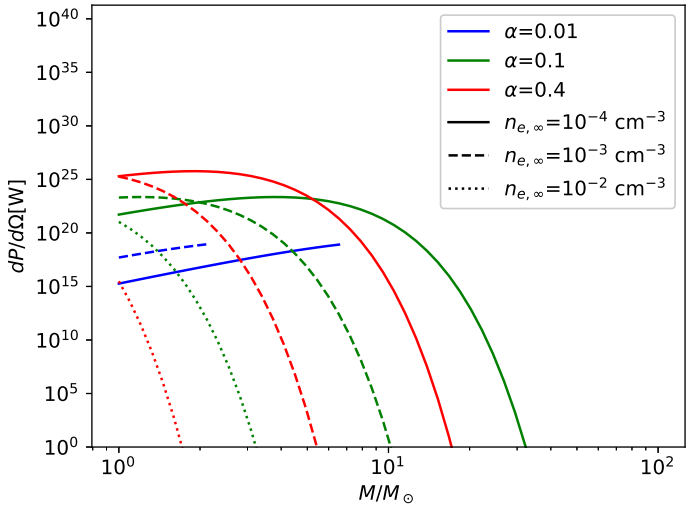

Figure 4.3. The radiated power vs. M for different pairings of α and ambient density. The relative velocity used here is $v_{rel} = 0.01$.

Plasma parameters: To get a better grip on how $n_{e,\infty}$ and v_{eff} affect the signals we plot the radiated power vs. both of them in figures 4.4 and 4.5 respectively. We see from the first figure that lower densities generally benefit the signals, but we can still achieve large signals as long as $n_e < 10^{-2}\text{cm}^{-3}$, which is the case in parts of the galaxy. The most restrictive parameter for resonant conversion is the velocity. We see in figure 4.5 that we require $v_{rel} > 10^{-3}$ and the most favorable case occurs when $v_{rel} \approx 0.01$. These velocities are on the extreme side but are not impossible to reach [74]. Therefore, a small isolated black hole traveling through the galaxy at these velocities can support an environment where resonant conversion can yield significant signals.

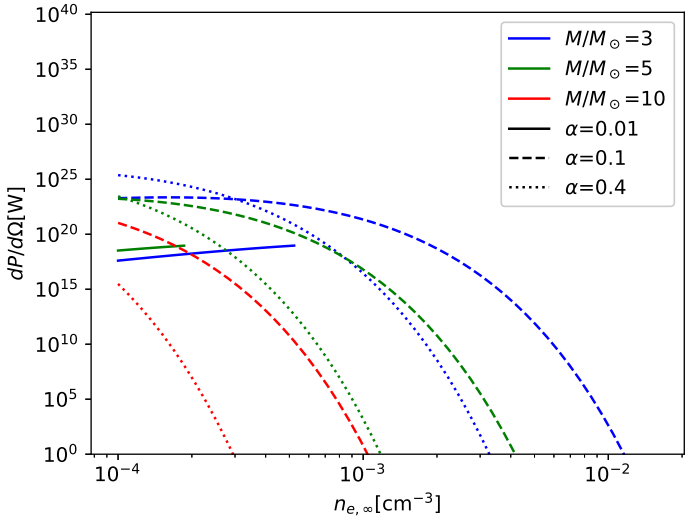

Figure 4.4. The radiated power vs. the ambient electron density, $n_{e,\infty}$, for a couple of (α, M) pairings. The relative velocity is fixed at $v_{rel} = 0.01$.

Magnetic field: In the above analysis, we have used the magnetic field model from eq. (2.46). However, as mentioned in the background, there are some model uncertainties here, and one get a lower estimate if one instead uses the equipartition $B^2 \propto Tn_e$ to estimate the magnetic field. We also have large-scale galactic magnetic fields of some µG [81, 86], and these can act as effective lower bounds on the field strength. The differences between these models are shown in figure 4.6, where the emitted power is plotted against the ambient density using the three different magnetic field models. We see that, even for the lower field strengths, that the emission can be substantial.

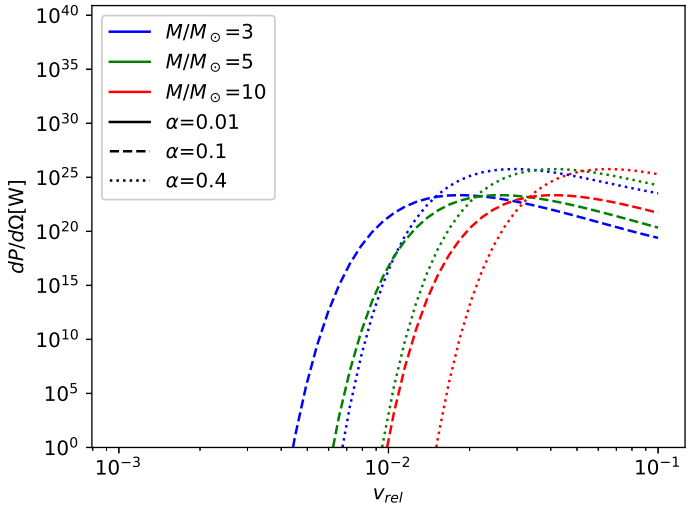

(a) $n_{e,\infty} = 10^{-3}\text{cm}^{-3}$.

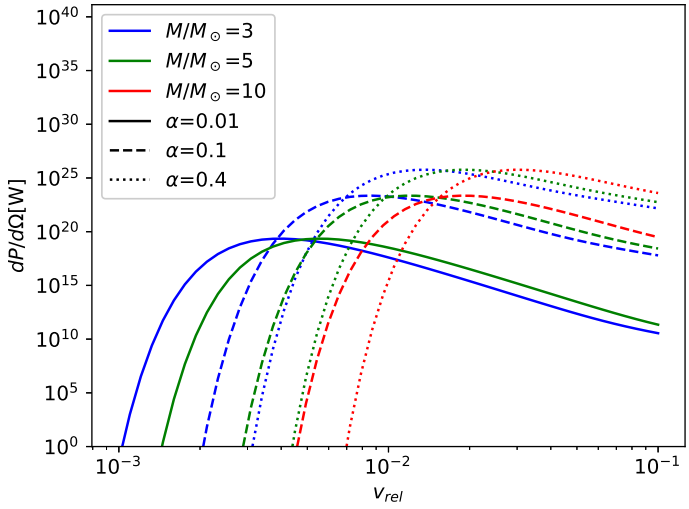

(b) $n_{e,\infty} = 10^{-4}\text{cm}^{-3}$.

Figure 4.5. The radiated power plotted against the relative velocity, calculated using two different ambient densities.

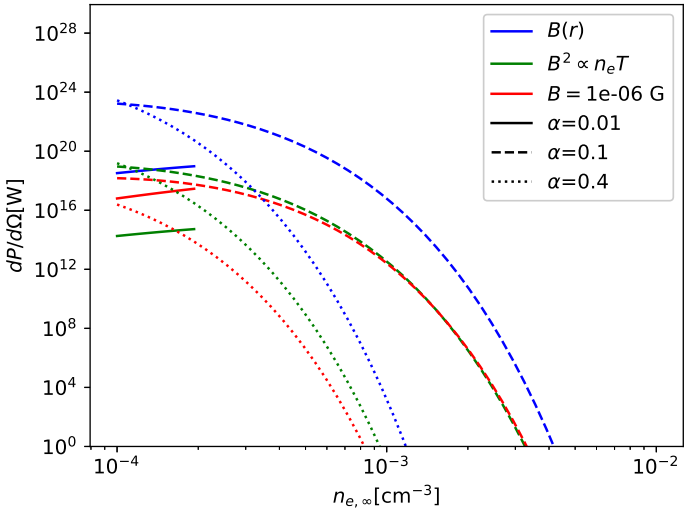

Figure 4.6. The emitted power vs. ambient electron density comparing three magnetic field models. $B(r)$, plotted in blue, refers to the model from eq. (2.46) which we have used throughout this chapter. The second model, plotted in green, uses the equipartition $B^2/8\pi \sim 4n_e(r)T(r)$, where n_e and T is given by eqs. (2.44) and (2.47), to estimate the magnetic field. The last plots, shown in red, uses a constant magnetic field of 1 µG. We use $v_{rel} = 0.01$ and $M = 5M_\odot$ in all calculations for this figure.

Temperature: Until now, we have neglected the temperature of the flow since when the relative velocities are large, the temperature does not affect the radiated power. However, this is not strictly true, and there is one important detail that depends on the temperature: the plasma frequency. The expression we used, eq. (4.1), is only accurate for low temperatures. If $T \approx m_e$ the plasma frequency will increase rapidly [87]. Therefore, we must ensure that the temperature at r_c is low enough, i.e. $T(r_{cl}) < m_e$, for our results to be valid. As mentioned in chapter 2, the electron temperature of accretion flows is a complicated subject with much uncertainty. For low-density spherical accretion, we have the models eqs. (2.47) and (2.51), which give quite different temperatures at the resonant radius. We will treat the former as a lower estimate and the second as an upper estimate and compare the predicted temperatures at r_c.

The easiest way to check if the temperature is lower than m_e is to compare the relativistic radius r_{rel}, defined as where $T(r_{rel}) = m_e$, to r_c. If $r_{rel} < r_c$, then the calculations of the previous sections should be accurate, otherwise our analysis of resonant conversion breaks down. Starting with the temperature from eq. (2.47), we have that

$$r_{rel} = \frac{T_\infty}{T_{rel}} r_b = \Theta_{e,\infty} r_b. \tag{4.19}$$

$r_{rel} < r_c$ is then satisfied if

$$\Theta_{e,\infty} < 0.072 \left(\frac{n_{e,\infty}}{1\,\mathrm{cm}^{-3}}\right)^{2/3} \left(\frac{M}{M_\odot}\right)^{4/3} \alpha^{-4/3}. \tag{4.20}$$

The weakest limit, for the systems we have considered, is at around $\Theta_{e,\infty} < 5{\times}10^{-4}$, which is the limit when $n_{e,\infty} = 10^{-4}\mathrm{cm}^{-3}$, $M = M_\odot$ and $\alpha = 0.5$. This corresponds to an ambient temperature of around 3×10^6 K, which is roughly the highest observed temperature in the interstellar medium [81]. Thus we can conclude that if the electron temperature follows the model of eq. (2.47) we do not have to worry about high temperatures.

The temperature model in eq. (2.51) from Ref. [68] predicts higher temperatures and we investigate this model in figure 4.7. In this figure, the region where $r_{rel} < r_c$ is marked in the $(v_{eff}, n_{e,\infty})$-plane for different black hole mass and α pairings. The figure indicates that there are some possibilities that the temperatures at r_c are too large. However, since the other model accepts all systems, we can treat eq. (2.51) as a worst-case scenario. We will discuss the temperature uncertainty and other potential flaws at the end of the next chapter.

4.4 Bondi suppression

In the previous section we have used the Bondi suppression factor $\lambda_s = 1$, i.e. the accretion rate is $\dot{M} = \dot{M}_{BHL}$ from eq. (2.39). We saw then that we required large velocities. Some studies have suggested that λ_{eff} has to be small, $\lambda_{eff} \leq$

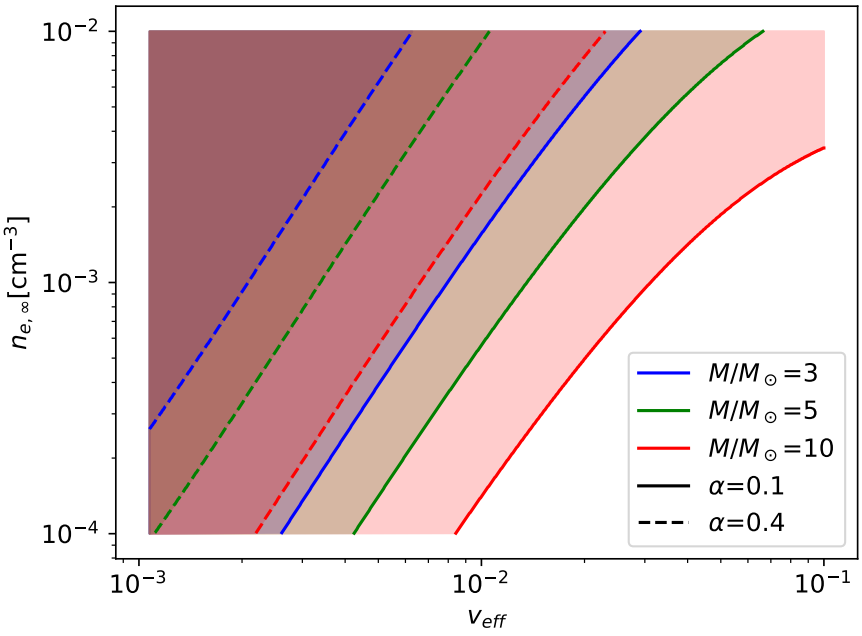

Figure 4.7. The areas in the $(v_{eff}, n_{e,\infty})$-plane where $r_c > r_{rel}$. r_{rel} is the radius at which $T(r_{rel}) = m_e$, calculated from eq. (2.51), the shaded area is therefore where the resonant radius is farther out than where the electrons become relativistic. In these areas, the radiated power calculated in this chapter is valid according to this model. However, this is an upper bound, and the area of validity is, in reality, larger. Especially since $T_\infty = 10^6$ K is used in this figure, which is the highest ambient temperature expected in interstellar space. For lower values of α, the temperature is low enough in the whole plane.

0.01, in order to explain the lack of signals from isolated black holes in the galaxy [73]. If this is the case, we would have a larger parameter space where resonant conversion could be relevant. However, another explanation for the lack of signals proposed in these studies is that the isolated black holes have higher velocities than previously assumed. Thus, we should not consider high velocities and small λ_{eff} simultaneously. Instead, we will try to answer the question of whether a reduced value of λ_{eff} could compensate and yield large luminosities for slower black holes. I.e., how small does λ_{eff} have to be for the emitted power to remain large if we reduce the relative velocity to 0, i.e. $v_{eff} \approx c_s$.

With the magnetic field model we used throughout the chapter, we have that

$$\frac{dP}{d\Omega} \propto B(r_c)^2 r_c^3 g(r_c) \propto \lambda_{eff}^{4/3} v_{eff}^{-4} g(r_c). \tag{4.21}$$

This expression includes all the factors of λ_{eff} and v_{eff}. The exact dependence in $g(r_c)$ is complicated, but this factor ensures that the resonant radius is as close to the cloud as possible. Thus, we want r_c to be unchanged, i.e. $\lambda_{eff}^{2/3} v_{eff}^{-2}$ should stay constant. If this is the case, then the prefactors of eq. (4.21) will also stay the same. From this we have found the condition that $\lambda_{eff} v_{eff}^{-3}$ should stay constant. Reducing from $v_{eff} \approx 0.01$ to $v_{eff} \approx c_s \approx 10^{-4}$, which is the largest sound speed typically encountered in the interstellar medium, would then require $\lambda_{eff} = 10^{-6}$. This is much lower than the suggested reduction of $\lambda_{eff} \approx 10^{-4} - 10^{-2}$. We can therefore conclude that the signals favor larger velocities rather than Bondi suppression. Some in-between mode might exist with some Bondi suppression for slightly slower black holes, which could yield large enough signals for a larger parameter space than found in the previous section. We do, however, leave this for future study.

4.5 Quenching the superradiant instability

We have seen in this chapter, that the estimated luminosity is much larger than for the non-resonant conversion of the previous chapter. Therefore, to give a complete comparison, we want to investigate whether resonant conversion can quench the superradiant instability since it is more efficient in turning axions into photons than the non-resonant conversion. Since there is very little exchange of energy between the plasma and the axion cloud, the signal should be quite monochromatic with all photons emitted close to $E_\gamma \approx m_a$. We can then estimate the number of converted axions per second to be $\dot{N} \approx L/m_a$. Assuming a fully developed axion cloud of mass $M_{cl} \approx fM$, we have that the total number of axions present is $N = fM/m_a$, and we can approximate the number rate as

$$\Gamma \approx \frac{L/m_a}{M_{cl}/m_a} = \frac{L}{fM}. \tag{4.22}$$

The largest signals estimated have a luminosity of $L \approx 10^{25}$ W for $M = 3M_\odot$ and $f = 0.01$. With this we have

$$\Gamma \approx 1 \times 10^{-21}\,\mathrm{s}^{-1}. \tag{4.23}$$

This is much larger than what we found in 3.2. However, it is still much smaller than the superradiant rate. We can therefore use the same argument as in section 3.2 to conclude that resonant conversion will not be able to quench the superradiant instability. Thus, neither resonant nor non-resonant interactions between the astrophysical plasma and the axions can interfere with the evolution of the superradiant axion cloud.

Chapter 5

Detectability

In this chapter, we will discuss the possible application of the work from the previous chapters. To give a complete picture, we will also look closer at which systems the work is relevant for and put the work in its astrophysical context. Before we go into details, it is worth summarizing the results of the two previous chapters. We have studied the interaction between a superradiant axion cloud and the astrophysical plasma around a black hole. We divided it into dense accretion flows and non-dense accretion flows where resonant conversion could occur, each type studied in chapter 3 and 4, respectively. The commonality found between both was that the interaction was not effective enough to quench the evolution of the axion cloud, and we, therefore, focused the study on electromagnetic signals. We found that the signals from both types of systems could be neglected for SMBHs and reached the highest luminosities for the smallest stellar black holes.

In chapter 3, we found that the emission was essentially independent of the density of the flow and the contribution from an accretion disk was negligible compared with that from spherical accretion. However, the estimates from a single accretion disk are not the complete picture, and the total luminosity from a system hosting a disk are probably more akin to that estimated for spherical accretion since the disk will be surrounded by a hotter plasma in addition to the disk [59]. However, there will be a reduction compared with pure spherical accretion since the disk will cool the system overall. The maximum luminosity found in this chapter was around 10^{14} W if the black hole were small, rapidly spinning, and only accreted spherically. Neglecting the reduction that a disk would entail, whose presence we rely on to detect black holes, this is the maximum luminosity we can expect from an axion cloud surrounding one of the observed stellar black holes in our galaxy.

In chapter 4, we looked at systems where resonant conversion of axions into photons could occur. In these systems, the luminosities reached 10^{25} W, which is significantly higher than for non-resonant conversion. To achieve this magnitude, we found that the black hole had to travel fast through an ambient medium of densities found in the sparsest regions of interstellar space or in intergalactic space.

In this chapter, we will look at the which parts of the axion parameter space could potentially be observed through direct detection of our signals using radio astronomy. We will also look at the interaction between the emitted photons and their surroundings, both directly in the accretion flow and the ambient medium to see if this could have detectable effects. The population of systems where it is likely that the estimated signals to be realized is then discussed. Finally, we end this chapter, and the thesis, by discussing some of the major uncertainties of the used models.

5.1 Direct detection

The main goal of this work is to find new channels through which we can search for the axion. In this section we want to compare our signals to the sensitivity of modern telescopes in order to determine if they can be used for this. However, the telescope in question must be able to operate at the given frequencies of the signals and it turns out that this is the main limitation of applying our results in the search for the axion.

We plotted the spectrum from the denser spherical accretion and the accretion disk in figure 3.5. We see in this figure that for the disk and the weakest signals from spherical accretion, we have a peak at m_a, and only when α increases do a significant emission occurs at higher energies of $10^2 - 10^3 m_a$. In contrast, the resonant conversion only produces photons with energies $\sim m_a$. The axion mass corresponds to a frequency of

$$E_\gamma = m_a = \frac{\alpha}{M} = 4.2 \left(\frac{\alpha}{0.4}\right) \left(\frac{3M_\odot}{M}\right) \text{kHz}. \tag{5.1}$$

This frequency is sadly far below the range of modern ground-based radio telescopes whom all operate at frequencies above 10 MHz. This limit is imposed by absorption in the ionosphere and large interference from human-made sources at lower frequencies [88]. Thus, we have to consider space-based radio astronomy [88–90]. However, there are few telescopes currently operational here as well. They can reach frequencies down to around 100 kHz but are only observing sources in the solar system. There is much interest in developing this field to reach these extremely low frequencies, but there are many challenges to overcome before we can use space-based telescopes to search for our estimated signals. One of which is absorption in the solar wind of photons below 10 kHz. Thus, direct detection is challenging with current methods but dedicated space-based telescopes could possibly be used to search for narrow peaks at kHz corresponding to the axion mass in the future.

5.1.1 Using a hypothetical radio telescope

Even though direct detection is difficult, we might still want to toy with the idea of a telescope operating at the relevant frequencies. We can then get an idea about if our signals are large enough to detect in principle and which part of the axion parameter space could theoretically be searched with them.

To estimate if a signal is detectable by a given telescope, one can compare the flux density,

$$S = \frac{\frac{dP}{d\Omega}}{bd^2} = \frac{L}{b4\pi d^2} \tag{5.2}$$

calculated using the distance, d, to the source and the bandwidth, b, of the signal, with the minimum detectable flux of the telescope, S_{min}. S_{min} can be estimated by the formula [48, 91]

$$S_{min} = \frac{1}{\eta_s}\frac{\text{SEFD}}{\sqrt{2b\Delta t}}, \tag{5.3}$$

where SEFD is the system-equivalent flux density, b is the observing bandwidth, Δt is the total observation time, and η_s is the signal conversion efficiency. η_s^{-1} can also be referred to as the minimal signal to noise ratio. Since this section is speculative, we will, for simplification, assume that b is fine-tuned to be the same in both the signal flux density and S_{min}, and that it is of the same order as the frequency of the observed peak of the spectrum. We will not do any advanced bandwidth analysis. For the resonant conversion, we will therefore use $b = m_a$ and for non-resonant conversion $b \approx m_a - 10^3 m_a$, depending on α.

For a stellar black hole not experiencing resonant conversion we then have that

$$S \approx 10^{-6}\left(\frac{1000\,\text{pc}}{d}\right)^2\left(\frac{L}{10\,\text{TW}}\right)\left(\frac{1\,\text{MHz}}{B}\right)\text{Jy}, \tag{5.4}$$

where $1\,\text{Jy} = 1\times10^{-26}\,\text{W}\,\text{m}^{-2}\,\text{Hz}^{-1}$, and for a black hole experiencing resonant conversion

$$S \approx 10^{4}\left(\frac{1000\,\text{pc}}{d}\right)^2\left(\frac{L}{1\times10^{20}\,\text{W}}\right)\left(\frac{1\,\text{kHz}}{B}\right)\text{Jy}. \tag{5.5}$$

We consider $d = 1000$ pc since there could exist a population of isolated black holes in this region [73]. However, the most favorable signals from isolated black holes require $n_e \approx 10^{-4}$ cm^{-3} which we encounter more commonly outside the galaxy and would then be located at $d \gtrsim 10^5$ pc.

If $S > S_{min}$ the signal is detectable. However, since the telescope in question does not exist, we have to motivate some realistic values for η_s, Δt, and the SEFD. A good modern telescope can have efficiency up to almost $\eta_s \sim 1$, and we can use $\eta_s \approx .5$ for our hypothetical telescope. Due to the restriction imposed by the atmosphere discussed in the previous section, we can assume that this telescope will be space-based and can handle longer observation times. In Ref. [48] they use an observation time of 100 h, which is a good baseline. The SEFD is difficult to estimate since

it is the least straightforward to interpolate from existing telescopes and is highly frequency dependent. In Ref. [48] they use the approximate value 2 Jy from the Arecibo Telescope operating at GHz, and the DSL mission described in Ref. [90] might achieve a sensitivity down to ∼5 Jy operating around 1 MHz. Therefore, it is not inconceivable to propose that a telescope designed for the detection of the specific wavelengths in question might reach down to 1 Jy. However, a more realistic estimate, compared with most currently operating radio telescopes, is around 100 Jy. To be somewhat restrictive, we will, for our hypothetical telescope, use SEFD = 100 Jy. We can now estimate what part of the parameter space we can probe using our estimated signals with this hypothetical telescope.

In all numerical results in the previous chapters, we have used the upper bound on $g_{a\gamma}$ from eq. (2.6) to give the highest possible luminosity. The goal now is to find what the minimum $g_{a\gamma}$ is that still yields detectable signals. Since S has the simple $S \propto g_{a\gamma}^2$ dependence, we can extract the lowest possible coupling easily from the equation $S = S_{min}$. Thus, given a black hole of mass M, we can look for axions of masses close to $m_a \sim 1/M$, and with a coupling down to the limit estimated from $S = S_{min}$, using our hypothetical radio telescope. From this, we get a region in the $(m_a, g_{a\gamma})$ parameter space which, theoretically, could be probed and excluded if we do not find the signals.

In figure 5.1 we have plotted the hypothetical $S = S_{min}$ line in the $(m_a, g_{a\gamma})$ plane for a couple of black hole systems experiencing resonant or non-resonant conversion. The region above this line represent the axions that we could theoretically look for using direct detection of our signals. The figure shows that resonant conversion around isolated black holes is fairly potent in restricting the parameter space. However, since we have to detect and identify the isolated black holes themselves first, they are not very practical for this purpose. We could potentially be able to use the signals to search for the black holes instead. The black holes experiencing non-resonant conversion do not cover any new areas but could be used to reinforce the exclusion from CAST for small axion masses.

We reiterate here that the main purpose of this section and figure 5.1 is to illustrate the magnitude of the signals and is purely hypothetical in its actual practical use for searching for the the axion. As we will discuss, other obstacles than the low frequency make this type direct observation difficult.

5.2 Absorption

In the previous section, we assumed that the emitted photons travel undisturbed through the galaxy. This is not necessarily the case, especially not at the lowest frequencies of interest. The photons will interact with the astrophysical plasma and can be absorbed or even upscattered. At the frequencies in question free-free absorption is the dominant channel of absorption. The mean-free path for a photon of energy E_γ traveling through a medium with particle densities $n_e = n_p = n$ of

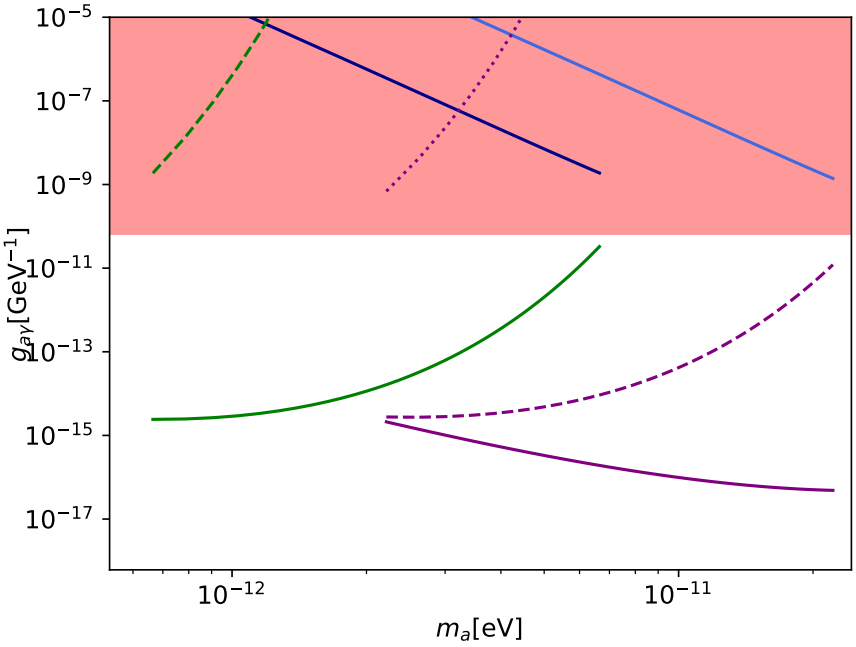

Figure 5.1. The part of the axion parameter space that could be searched observing six different black hole configurations. The area above the lines represents the axion parameter space which can be probed using the hypothetical telescope to search for the estimated signals of this work. The blue lines represent stellar black holes that accrete spherically without resonant conversion, located at a distance of 1000 pc from Earth. The darker blue has $M = 10M_\odot$ and the lighter blue line has $M = 3M_\odot$. The purple and green lines are black holes outside of the galaxy which experience resonant conversion. These are also located at $d = 1000$ pc from Earth, and the green represent a mass of $10M_\odot$, while the purple has $M = 3M_\odot$. The full line was calculated using $n_{e,\infty} = 1 \times 10^{-4}\,\mathrm{cm}^{-3}$, the dashed with $n_{e,\infty} = 1 \times 10^{-3}\,\mathrm{cm}^{-3}$, and the dotted with $n_{e,\infty} = 1 \times 10^{-2}\,\mathrm{cm}^{-3}$. Each line is limited to axion masses in $[0.05/M, 0.5/M]$, all black holes are assumed to have $a = 0.9M$, and the cloud has the mass fraction of $f = 0.01$. The resonant conversion is also calculated with $v_{rel} = 0.01$. The shaded area represents the parameter space that has been excluded by CAST [10].

temperature T is [41, 92]

$$l_{mfp} = (n\sigma_{ff})^{-1}\,, \tag{5.6}$$

where

$$\sigma_{ff} = \frac{4\pi^2\alpha\sigma_T}{\sqrt{6\pi}} n \sqrt{\frac{m_e}{T}} \frac{g_{ff}(E_\gamma, T)}{TE_\gamma^2} \tag{5.7}$$

and the gaunt factor is given by

$$g_{ff}(E_\gamma, T) \approx 4.691 \left(1 - 0.118 \ln\left(\left(\frac{E_\gamma}{6.58\,\mu\mathrm{eV}}\right)\left(\frac{T}{1\times10^4\,\mathrm{K}}\right)^{-3/2}\right)\right). \tag{5.8}$$

Scaled to the black hole mass, for comparison, we have

$$\frac{l_{mfp}}{M} \approx 1.1\times10^7 \left(\frac{M}{3M_\odot}\right)^{-3} \left(\frac{\alpha}{0.1}\right)^2 \left(\frac{T}{1\times10^4\,\mathrm{K}}\right)^{3/2} \left(\frac{n}{1\,\mathrm{cm}^{-3}}\right)^{-2}. \tag{5.9}$$

If we consider the simple model for spherical accretion we have used, where $T \propto r^{-1}$ and $n \propto r^{-3/2}$, then $l_{mfp} \propto r^{3/2}$ in the accretion flow, and will be shorter closer to the black hole, i.e. more absorption will occur near the black hole. We can then get a conservative estimate by considering $l_{mfp} = l_{mfp}(n_\infty, T_\infty)$. Comparing this with the Bondi radius, $r_b \propto v_{eff}^{-2}$, will tell us whether the absorption will occur in the accretion flow or out in the surrounding medium.

For the resonant conversion, we required that $v_{eff} > 10^{-3}$ and $n_\infty < 10^{-2}$ cm^{-3}, and can readily conclude that most photons will be able to escape the system without being absorbed back into the accretion flow. However, for non-resonant conversion, we cannot draw this conclusion. Assuming that $v_{eff} \approx c_s$ we have that

$$r_b \approx c_s^{-2} \approx 1.3\times10^9 \left(\frac{T}{1\times10^4\,\mathrm{K}}\right)^{-1} \tag{5.10}$$

for an ideal hydrogen gas, which is larger than l_{mfp}. Even though we have photons of energies up to $10^3 m_a$, which would increase l_{mfp}, we also have higher densities than 1 cm^{-3}. It is, therefore, very likely that a significant portion of the non-resonant emission will be absorbed directly back into the accreted plasma. The question is then if this will affect the flow in any meaningful way. Assuming that the emitted energy is quickly reabsorbed in the accretion flow, we can then estimate the energy added to each accreted particle by

$$E \approx \frac{L}{\dot{M}/m_p} \approx 0.08\,\mathrm{eV} \left(\frac{L}{1\times10^{14}\,\mathrm{W}}\right)\left(\frac{\dot{m}}{10^{-8}}\right)^{-1}. \tag{5.11}$$

This energy is insignificant, especially when we consider the fact that much of the energy of the emitted photons come from the electrons themselves when $E_\gamma > m_a$, and the energy would simply be recycled. Therefore, we can conclude that the non-resonant conversion will not significantly affect the accretion flow, nor will most of the emitted photons escape the system.

For resonant conversion, we have that $l_{mfp} \gg r_b$. The photons will escape the system, and the energy will be spread out through the interstellar or intergalactic medium. However, the total energy is not large enough to affect the medium significantly, $L/(nl_{mfp}^3) \ll 1$ eV/s, compared to, for example, Ref. [41], where they estimate that burst of energy up to 10^{38} J distributed during a short period of time could cause shock waves in the medium. The photons from the resonant conversion will, therefore, simply pass through the medium or be absorbed into the surrounding without heating it noticeably.

Some of the photons will, instead of being absorbed, be upscattered through inverse Compton scattering, similar to the Sunyaev–Zeldovich effect for the CMB [93, 94]. In theory, this could increase the energy of the low-frequency photons to detectable levels, especially if it occurs in the hotter parts of the accretion flow. However, many subsequent scatterings are required to increase the magnitude enough to be detectable [94], and the mean free path for inverse Compton scattering in the limits $E_\gamma \ll m_e$ is [95]

$$\frac{l_{mfp}}{M} \approx \left(\frac{8\pi\alpha_{em}^2}{m_e^2} n_e M\right)^{-1} \approx 1 \times 10^{19} \left(\frac{M_\odot}{M}\right) \left(\frac{n_e}{1\,\mathrm{cm}^{-3}}\right)^{-1}, \tag{5.12}$$

which is much larger than for the free-free absorption. It is, therefore, unlikely that this can help in the search for the signals in question.

5.3 Stimulation effects

We expect that the photons from the resonant conversion will leave the system without being absorbed in the accretion flow. However, they can still affect the system without being absorbed. Since the number of photons is large, they contribute with a non-negligible electromagnetic field. Suppose the added magnetic field is comparable to the magnetic field suspended in the accretion flow. Then we will get an amplification of the conversion rate, which would lead to even larger magnetic fields and so on. This stimulation effect could lead to much larger signals than first estimated, which in turn would increase the likelihood of detection.

In Refs. [26, 40, 41] this type of stimulation process has been studied, but where the source of photons comes from the axion decay into photons. In these systems, the stimulation effect leads to pulsing laser-like emission with luminosities of up to 1×10^{50} W. In these papers, they neglect any interactions with the surrounding plasma. However, as we have shown, the interaction with the plasma can lead to significant photon emission, which could possibly result in similar stimulation effects as those estimate from the axion decay.

The emitted photons can stimulate the resonant conversion if the magnetic field the emitted photons contribute to reaches the same magnitude as the initial

magnetic field. If the energy density of the emitted photons is ρ_γ, then the magnetic field strength they contribute with is

$$B_\gamma \approx \sqrt{\rho_\gamma}. \tag{5.13}$$

We can estimate ρ_γ through

$$\rho_\gamma = p^\infty_{a\gamma} m_a n_a = \frac{\pi}{3} g^2_{a\gamma} B^2 \alpha r_c M n_a(r_c), \tag{5.14}$$

where $p^\infty_{a\gamma}$ is the energy transfer function from eq. (4.7). Assuming that we are in the most beneficial situation where $r_c = r_{cl} = 5/\alpha^2$ we have, from eq. (4.11), that

$$\rho_\gamma = \frac{50f}{288} g^2_{a\gamma} B^2 \alpha^3, \tag{5.15}$$

where we have used $g(5/\alpha^2) \approx 10/\alpha^2$. Stimulation effects becomes important if $B_\gamma \gtrsim B(r_c)$ which we can rewrite as

$$\sqrt{\frac{50f}{288}} g_{a\gamma} \alpha^{3/2} \gtrsim 1. \tag{5.16}$$

This can be formulated as the condition

$$g_{a\gamma} \gtrsim 2 \times 10^{-16}\,\mathrm{GeV}^{-1} \sqrt{f} \left(\frac{\alpha}{0.01}\right)^{-3/2} \tag{5.17}$$

on the coupling constant. We can compare this to a similar condition found for stimulated decay in Refs. [40, 41]

$$g_{a\gamma} \gtrsim 1 \times 10^{-15}\,\mathrm{GeV}^{-1} f^{-1/2} \left(\frac{\alpha}{0.01}\right)^{-2}. \tag{5.18}$$

These conditions describe the coupling strength required for a system to experience stimulation effects. We see that our bound is very similar to theirs, and we can therefore expect stimulation effects to be relevant for resonant conversion as well. Thus, there is a possibility that including stimulation effects could increase the luminosities estimated in chapter 4 by many orders of magnitude. We also have to note that the plasma frequency blocks the decay of axions when $\omega_{pl} > m_a/2$, and resonant conversion cannot be relevant simultaneously as the stimulated decay. The plasma interaction could instead replace the decay as the source of photons and still lead to lasing of similar amplitudes as estimated in Refs. [26, 40, 41]. The plasma interaction might also accelerate the lasing since decay is a slower process than the plasma interactions. Overall, considering stimulation effects increase the likelihood that resonant conversion can cause observational signals. We do, however, have to leave a more detailed analysis of this for future study.

5.4 Relevant astrophysical systems

Throughout this thesis, we have assumed the existence of a black hole of a given mass M and spin a, coupled to an axion field of mass α/M, where α is large enough to form an axion cloud of mass $M_{cl} = fM$. We have then essentially treated all of these parameters as independent, which is not the case. For example, M and α must satisfy condition (2.24) for the growth of the cloud to occur in astrophysical time and we considered $0.5 > \alpha > 0.01$ in the analysis to keep to this condition. Further, we have that the mass of the cloud cannot exceed $f \approx \alpha a/M$ from eq. (2.27), and for that reason we rarely exceeded $f > 0.01$, which might even be a bit restrictive for the largest α but slightly too large for the smallest. We were less careful with the condition from eq. (2.21) which imposes large spin. However, the luminosity from the resonant conversion is only dependent of the spin through f, and the non-resonant favors extremal spin, so our results are compatible with this condition.

The above restrictions give reasonable estimations of the parameters involved. However, to get the full relationship between them and the complete picture of the system overall, one must consider the full time evolution. All the parameters are time-dependent and the discussed conditions must be satisfied at different times during the growth of the cloud. To study the time evolution, one has to solve the relevant differential equations, including the superradiant growth, energy extraction from the black hole, and all the relevant depletion channels in the cloud. A good study of this is Ref. [31]. They include accretion, which is important for the evolution of the black hole, as well as depletion through gravitational wave emission. As we have concluded, the plasma interaction is not effective enough to quench the evolution of the cloud. Thus the general behavior from reference [31] give good insight for our systems as well. Solving these time evolution equations is beyond the scope of this thesis, but we can relay the important points to supplement the complete picture of the systems of interest.

In contrast to how we have treated the analysis in the main part of the thesis, the only fully static parameter is the axion mass, which will have a single value if the axion exists. Thus, the black hole must be tuned to the corresponding mass, $M \approx 1/m_a$, for an axion cloud to form. If the accretion rate is large enough, and the black hole mass is smaller than $1/m_a$, it will eventually grow and spin up enough to trigger the instability. The cloud will then grow and reduce the black hole spin until eq. (2.21) no longer is satisfied, shutting down the instability. The exact behavior after the shutdown is the most complicated, but the cloud will start to deplete, mainly due to gravitational wave emission and partly due to the interactions we have discussed. Therefore, the signals we have estimated will change in time, mostly due to the proportionality to f, but also since α changes when M grows. The decreasing value of a will also affect the emission through non-resonant conversion. Our estimated luminosities will then represent the maximum achieved only during a shorter period of time and not represent a constant emission. A complete time analysis would, of course, benefit this work but there is one detail in this analysis which is not valid for our systems.

The described scenario relies on the accretion to eventually put the system in the right mass range to trigger the instability. However, for the resonant conversion we have considered the accretion rates are around $\dot{m} \approx 10^{-10} - 10^{-18}$, see eq. (2.40), and the time scale which describes how fast accretion affect the mass of the black hole is

$$\frac{M}{\dot{M}} \approx 5 \times 10^7 \dot{m}^{-1} \text{yr}. \tag{5.19}$$

We can, therefore, not rely on accretion to tune isolated black holes to the axion mass since it would take far longer than is observationally relevant to change the mass significantly. Therefore, the black hole has to be created at the correct mass. Further, for resonant conversion, we also require fast traveling isolated black holes. The small catalog of observed black holes does not support the existence of any that satisfy the relevant criteria. This is mainly due to the fact that we require high accretion rates to discover black holes. However, there are reasons to believe that large populations of isolated black holes exist in our galaxy. They have just eluded observation so far.

From stellar evolution models, there are estimates that there should exist up to 10^8 stellar black holes in our galaxy [96]. These are remnants of supernova explosions and are more often than not left isolated. Another theory that could result in a large population is that of primordial black holes (PBHs) [97]. These are black holes created in overdense regions in the early stages of the universe and are candidates to explain a portion of the dark matter in the universe. The mass of PBHs is not restricted to the typical values of stellar remnants and could be less than $M_\odot$. Regardless of their origin, there are reasons to believe isolated black holes exist in the galaxy, and many are currently searching for them through the emission caused by low rate accretion [73, 75–77]. Since we know very little about these black holes, we cannot say much about their evolution and interactions. However, they might reach the high velocities we require for resonant conversion, either from the initial supernova kick or through merging events. With these velocities, they could also easily escape the galaxy, reducing the ambient density around them.

An additional benefit in considering PHBs is the possibility of lower masses. The main restriction of the signals we have derived is the mass bound from stellar evolution. Lower mass black holes could potentially probe for larger axions that undergo resonant conversion at larger densities which would no longer require intergalactic ambient densities and extreme velocities. Further, the frequency of the emission would be higher around PBHs and potentially be detectable with modern telescopes. Suppose the population of black holes contributes to a significant portion of the dark matter in the galaxy. Then we should also expect that a significant portion of these black holes are located far outside the galaxy center since the dark matter halo extends further than the galaxy itself. This could then result in the lower densities of around 10^{-4} cm^{-3} that benefit resonant conversion.

The existence of a large population of isolated black holes, independent of their origin, is the most likely source of the signals we have studied in this thesis and could help with the search for the axion, especially if their mass is smaller than considered

in this thesis. We end this section by also mentioning that significant signals from resonant conversion could also be treated as a tool to help the search for isolated black holes, especially if the axion with the right mass is discovered through other means. The detection of the right signals from some unknown source could then lead us to both isolated black holes and the axion, or the absence of signals could mutually exclude the existence of axions in this mass range and isolated black holes of the corresponding mass.

5.5 Model uncertainties

We want to end the thesis by reiterate and discuss the largest uncertainties in the models of this work and bring up some possible steps for improvement.

The first point of uncertainty is that of the inclusion of the plasma frequency in chapter 3. We mentioned that we see quite a lot of emission at low frequencies which was not expected. One possible error is that the plasma frequency is not considered in the kinematics and its inclusion would likely reduce the emission at $E_\gamma < \omega_{pl}$. Another interpretation is that the low frequency photons will be quickly absorbed back into the plasma, yielding no effective emission at these frequencies. Either way, we concluded in this chapter that the signals estimated in chapter 3 are barely significant as is, so this problem will not affect the general conclusion. However, a more detailed analysis would definitely benefit the work. It could also be helpful for future applications with low mass axions since it is more common throughout the literature to consider axion conversion where $E_\gamma \gg m_a \gg \omega_{pl}$, which, as we have seen, is not always the case.

The second, and most important uncertainty, lies in the simplified models of the electron temperature in spherical accretion. The temperature affects the estimated signals from both the non-resonant and resonant conversion. For relativistic temperatures our analysis for resonant conversion would break down since the plasma frequency becomes temperature dependent and a study including the full expression would be required. However, higher temperatures would benefit the non-resonant conversion and increase the total emission, especially if the temperature closest to the black hole is increased in a more realistic model. A population of non-thermal electrons is also likely to be present, and we have not included it in our models. A more detailed study of the temperature of the accretion flow, possibly using simulation methods or some non-explicit $T(r)$ dependencies, is necessary to increase the accuracy here. The choice of models simplified the analysis in this work but possibly reduced the accuracy. However, the findings are still relevant and show that the interaction between the axion clouds and the surrounding plasma can cause significant effects in the right circumstances.

The final point of uncertainty is that of the stability of the spherical accretion model for n and B in the high velocity and high spin limits. The model was chosen partly due to its simplicity, and its validity is interpolated to extreme limits in v_{eff} and a. The high spin limit is usually assumed to hold without much discussion.

As we saw for the disk model, the biggest effect of high spin is the location of the ISCO, and it is not unreasonable to assume that the location of the ISCO and the event horizon is the most important differences for spherical accretion in this limit as well. One example which considers the effect of high spin is Ref. [98] where they found that high spin might reduce the accretion rate but the spherical symmetry might also be lost. The extreme velocities that we have considered in this work have rarely been studied in this context of spherical accretion. Ref. [68] includes a small discussion and concludes that the spherical accretion should be stable from forming a disk at high speeds but do not claim anything further than that. The spherical accretion model might break down in other ways, for example, by losing spherical symmetry or be affected by turbulence. A more sophisticated analysis of this limit has to be made to be sure, but this is not the subject of this thesis. We assumed that the models are stable enough that our results still pose as valid approximations.

Chapter 6

Summary and conclusions

In this thesis, we have studied the interaction between superradiant axion clouds and the astrophysical plasma the hosting black hole accretes. We divided the interactions into two separate parts, scattering processes in denser accretion flow, which we studied in chapter 3, and resonant conversion possible in low-rate accretion flow, which was the focus of chapter 4. We could conclude, for both types of interactions, that the conversion of axions into photons was not effective enough to quench the formation of the axion cloud and affect previously predicted gravitational signals. We, therefore, shifted the focus to the possible electromagnetic signals caused by the conversion of axions into photons.

We found that the scattering processes relevant in dense accretion flows to be essentially independent of the density of the accreted matter. This was due to the fact that the signals were proportional to the electron density but also suppressed by the Debye screening which is proportional to the density. These two effects then canceled each other for most systems of interest. Due to this independence of the density we could conclude that the emission from the interaction in an accretion disk would be negligible compared to that from the hotter plasma found in spherical accretion. In the most favorable case, the luminosity from spherical accretion could reach up to 10^{14} W, with a significant contribution at a frequency a couple of magnitudes larger than the axion mass. The most significant emission was predicted to come from a small and fast-spinning black hole, whereas the emission estimated from SMBHs was found to be insignificant.

The resonant conversion in low-rate accretion could yield luminosities of up to 10^{25} W. To achieve these magnitudes, the accretion rate had to be low enough so that the plasma frequency could be comparable to the axion mass somewhere in the accretion flow. We concluded that the black holes have to travel very fast and through a low-density region of space for this to be possible. We also found that, in a realistic setting, resonant conversion can only happen for black holes with masses less than $\sim 10M_{\odot}$. As for the non-resonant conversion, we saw that the smallest possible black hole led to the largest luminosities.

In chapter 5, we discussed the possibility of detecting the signals from both types of interactions. We saw there that direct detection seemed challenging and would require dedicated space-based telescopes looking for narrow peaks in the kHz range corresponding to a specific axion mass. We also discussed the possibility for the photons to cause other detectable signatures from the system. We found that the most likely scenario was that the photons would be quickly absorbed, possibly already in the accretion flow. However, the energy extracted from the axion cloud was estimated to be too low to heat the plasma enough to disrupt the accretion flow or cause detectable shock waves in the surrounding medium.

The black holes that we have observed throughout the universe belong to the category of denser accretion flows, and we could not find any new signatures that could be used to detect an axion cloud around these. The signals from resonant conversion were found to be more promising and could potentially be large enough to be observable with dedicated telescopes and then be used to search for axions or isolated black holes. We also mentioned that stimulation effects might be relevant in the resonant case due to the large photon density. We did not go into details about this but referred to Refs. [39–41] where similar effects have been studied. However, we concluded that stimulation effects could amplify the signals further and improve the possibility of detection. Since the signals could be detectable, we discussed the population of isolated black holes around which resonant conversion could be relevant. We concluded that the theoretically predicted large population of isolated black holes in and around the galaxy was well suited to yield signs of resonant conversion. Overall, we can conclude that the commonly used assumption that we can neglect the interaction between an axion cloud and the astrophysical plasma still holds well for typical black hole systems but around isolated black holes it could be important and potentially helpful in the search for axions.

Appendix A

Deriving the superradiant exponents

In this appendix, we derive the superradiant rates in the slow-spinning, $a \ll M$, and non-relativistic, $\omega \approx m_a$, approximation. The derivation provided here is a detailed account based mainly on similar calculations found in Refs. [23, 25, 26, 62], and serves the purpose to fill in gaps commonly brushed over.

The goal of the derivation is to determine the energy eigenvalues of the quasi-bound modes of the axion field around a black hole. This is done by first separating the Klein–Gordon equation into one angular and one radial equation. The angular equation is then solved to acquire the separation constant. The radial equation can then be solved by dividing space into a far and a near region. In each region, the radial equation can be solved analytically, and the final step of the derivation is to match the solutions in the overlap of the two regions. This yields an equation from which the energy eigenvalues can be extracted. The superradiant exponents can then be found as the imaginary part of the eigenvalues.

A.1 Klein–Gordon equation in the Kerr-background

The dynamics of the axion field is described by the Klein–Gordon equation

$$\left(\nabla_\mu \nabla^\mu - m_a^2\right) \psi = 0, \tag{A.1}$$

where any backreactions and non-linarities can be neglected, see Ref. [31] for a discussion of this topic. Using the Kerr-metric in eq. (2.9) one can get the full

equation in terms of Boyer–Lindquist coordinates. It turns out that this equation is separable using the ansatz [65]

$$\psi = e^{-\mathrm{i}\omega t + \mathrm{i}m\phi} R(r) S(\theta), \tag{A.2}$$

where $R(r)$ solves the radial equation

$$\Delta \partial_r \left(\Delta \partial_r R(r)\right) + \left[\left((r^2+a^2)\omega - ma\right)^2 - \Delta\left(r^2 m_a^2 - 2\omega m a + a^2\omega^2 + C\right)\right] R(r) = 0, \tag{A.3}$$

and $S(\theta)$ solves the angular equation

$$\frac{1}{\sin\theta}\partial_\theta\left(\sin\theta \partial_\theta S(\theta)\right) + \left[C - a^2(m_a^2 - \omega^2)\cos^2\theta - \frac{m^2}{\sin^2\theta}\right] S(\theta) = 0, \tag{A.4}$$

where C is the separation constant. Equations (A.3) and (A.4) can now be treated separately.

A.2 The angular equation

Equation (A.4) can be forund as eq. (21.6.2) in chapter 21 about spheroidal wave functions in Ref. [99] in the form

$$\frac{d}{d\eta}\left[(1-\eta^2)\frac{d}{d\eta}S_{lm}(c,\eta)\right] + \left(\lambda_{lm} - c^2\eta^2 - \frac{m^2}{1-\eta^2}\right) S_{lm}(c,\eta) = 0. \tag{A.5}$$

To match ours we identify $\eta = \cos\theta$, $c^2 = a^2(m_a^2 - \omega^2)$, $\lambda_{lm} = C$, $S_{lm}(c,\eta) = S(\theta)$, and that

$$\frac{d}{d\cos\theta}\sin^2\theta\frac{d}{d\cos\theta} = \frac{d}{-\sin\theta d\theta}\sin^2\theta\frac{d}{-\sin\theta d\theta} = \frac{1}{\sin\theta}\frac{d}{d\theta}\sin\theta\frac{d}{d\theta}. \tag{A.6}$$

The eigenvalues, λ_{lm}, can be expanded as

$$\lambda_{lm} = \sum_{i=0}^{\infty} k_{2i} c^{2i}, \tag{A.7}$$

where the first two terms are

$$k_0 = l(l+1) \text{ and } k_2 = \frac{1}{2}\left[1 - \frac{(2m-1)(2m+1)}{(2l-1)(2l+3)}\right]. \tag{A.8}$$

Here l and m are integers satisfying $|m| \leq l$. Note that in the limit $c \to 0$ we recover the spherical harmonics

$$e^{\mathrm{i}m\phi} S(\theta)\big|_{c=0} = Y_{lm}(\theta,\phi), \tag{A.9}$$

showing the resemblance to the hydrogen atom. From this we have obtained the separation constant, which in the slow spinning and non-relativistic limit are well approximated by

$$\lambda_{lm} \approx l(l+1). \tag{A.10}$$

A.3 The radial equation

A.3.1 Setup for the radial equation

From the angular equation we have retrieved an expression for the separation constant, $C = \lambda_{lm}$, and we can now study the radial equation, eq. (A.3). Since we assume $a \ll M$ we have that $a\omega \approx am_a \ll \alpha \ll 1$, and also $r \gg a$ in the whole region of consideration. This allow us to neglect some terms in eq. (A.3) of higher order in α, and left is

$$\Delta\partial_r\left(\Delta\partial_r R(r)\right) + \left[\left(r^2\omega - ma\right)^2 - \Delta\left(r^2 m_a^2 + l(l+1)\right)\right] R(r) = 0. \tag{A.11}$$

To proceed, we divide the space in two regions, the near region where $r - r_+ \ll 1/m_a$, and the far region where $r - r_+ \gg M$. Since $\alpha = m_a M \ll 1$ we have an overlap between these two regions, and the strategy is then to match the solutions found in the two regions in the overlap. This will allow us to extract the eigenvalues ω.

To do this we need boundary conditions for equation in both regions. Since we consider quasi-bound states we want a well behaved solution at infinity and thus $\lim_{r\to\infty} R(r) = 0$ is the boundary condition in the far region. At the horizon, r_+, we want the wave to be ingoing, i.e. the radial momentum given by the momentum operator $-\mathrm{i}\partial_r$ should be negative.

A.3.2 Near region

In the near region $r \approx r_+$, and since we assume $a \ll M$, $r_+ \approx 2M$, which means that $rm_a \approx \alpha$. Thus, to first order in α we have

$$\Delta\partial_r\left(\Delta\partial_r R(r)\right) + \left[\left(r_+^4\left(\omega - m\Omega\right)^2 - \Delta l(l+1)\right]\right. R(r) = 0, \tag{A.12}$$

where the angular velocity of the horizon, $\Omega = a/2Mr_+ \approx a/r_+^2$, were inserted. We can now introduce the coordinate

$$z = \frac{r - r_+}{r - r_-} \tag{A.13}$$

that goes from $z = 0$ at the horizon and to $z = 1$ at infinity. With this definition we get

$$\partial_r = \frac{(z-1)^2}{r_+ - r_-}\partial_z \tag{A.14}$$

and

$$\Delta = \frac{z\left(r_+ - r_-\right)^2}{(1-z)^2}. \tag{A.15}$$

Inserting these, dividing by $\Delta(1-z)$, and introducing

$$\varpi = (\omega - m\Omega)r_+^2/(r_+ - r_-) \tag{A.16}$$

transforms the radial equation to the following equation in z

$$z(1-z)\partial_z^2 R(z) + (1-z)\partial_z R(z) + \varpi^2 \frac{1-z}{z} R(z) - \frac{l(l+1)}{1-z} R(z) = 0. \tag{A.17}$$

Here we redefine R as

$$R(z) = z^{\mathrm{i}\varpi}(1-z)^{l+1} F(z) \tag{A.18}$$

with this inserted the equation takes the form

$$z(1-z)\partial_z^2 F(z) + \left[\tilde{c} - (\tilde{a} + \tilde{b} + 1)z\right] \partial_z F(z) - \tilde{a}\tilde{b} F(z) = 0. \tag{A.19}$$

We have briefly introduced the constants $\tilde{a} = l + 1 + 2\mathrm{i}\varpi$, $\tilde{b} = l + 1$ and $\tilde{c} = 1 + 2\mathrm{i}\varpi$ to match it with the standard hypergeometric equation, eq. (15.5.1) in Ref. [99], the tilde is used to avoid confusion with the previouly introduced variables. Close to $z = 0$, which is the definition of the near region, we have two linearly independent solutions $F(\tilde{a}, \tilde{b}, \tilde{c}, z)$ and $z^{1-\tilde{c}} F(\tilde{a} - \tilde{c} + 1, \tilde{b} - \tilde{c} + 1, 2 - \tilde{c}, z)$, which inserted into $R(z)$ gives

$$R(z) = z^{\mathrm{i}\varpi}(1-z)^{l+1} \left(A z^{-2\mathrm{i}\varpi} F(\tilde{a} - \tilde{c} + 1, \tilde{b} - \tilde{c} + 1, 2 - \tilde{c}, z) + B F(\tilde{a}, \tilde{b}, \tilde{c}, z) \right). \tag{A.20}$$

When $z \to 0$ we have that these solutions behave as $(r - r_+)^{\pm \mathrm{i}\varpi}$. Since we have the boundary condition of ingoing waves at the horizon we must set $B = 0$, and the solution in the near region is

$$R(z) = A z^{-\mathrm{i}\varpi}(1-z)^{1+l} F(l+1, l+1-2\mathrm{i}\varpi, 1-2\mathrm{i}\varpi, z). \tag{A.21}$$

In the end, we want to match this solution with the solution in the far region, in the overlap between M and $1/m_a$. In this region we have that $z \approx 1$, and we can do the following shift [99]

$$\begin{aligned} F(a,b,c,z) = {} & \frac{\Gamma(c)\Gamma(c-a-b)}{\Gamma(c-a)\Gamma(c-b)} F(a, b, a+b-c+1, 1-z) \\ & + (1-z)^{c-a-b} \frac{\Gamma(c)\Gamma(a+b-c)}{\Gamma(a)\Gamma(b)} F(c-a, c-b, c-a-b+1, 1-z) \end{aligned} \tag{A.22}$$

and we can use $F(a, b, c, 0) = 1$. Further in this limit we have that

$$1 - z = \frac{r - r_-}{r - r_-} - \frac{r - r_+}{r - r_-} \underset{r \gg r_-}{\approx} \frac{r_+ - r_-}{r}, \tag{A.23}$$

and altogether we have the following near solution in the middle region

$$\begin{aligned} R_{near}(r) \approx A \Bigg[& \left(\frac{r_+ - r_-}{r} \right)^{l+1} \frac{\Gamma(1-2\mathrm{i}\varpi)\Gamma(-2l-1)}{\Gamma(-l-2\mathrm{i}\varpi)\Gamma(-l)} \\ & + \left(\frac{r_+ - r_-}{r} \right)^{-l} \frac{\Gamma(1-2\mathrm{i}\varpi)\Gamma(2l+1)}{\Gamma(l+1)\Gamma(l+1-2\mathrm{i}\varpi)} \Bigg]. \end{aligned} \tag{A.24}$$

A.3.3 Far region

When $r - r_+ \gg M$ we can disregard the spin completely in our slow-rotation limit, and we have the equation

$$\Delta\partial_r\left(\Delta\partial_r R(r)\right) + \left[r^4\omega^2 - \Delta\left(r^2 m_a^2 + l(l+1)\right)\right] R(r) = 0, \tag{A.25}$$

where $\Delta = r^2 - 2Mr$. Using the chain rule it is easy to see that

$$\Delta\partial_r\left(\Delta\partial_r R(r)\right) = \Delta^{3/2}\left(\partial_r^2\left(\Delta^{1/2}R(r)\right) - R\partial_r^2\Delta^{1/2}\right) \tag{A.26}$$

with which the equation can be rearranged to

$$\partial_r^2\left(\Delta^{1/2}R(r)\right) - R\partial_r^2\Delta^{1/2} + \left[\frac{r^4}{\Delta^2}\omega^2 - \frac{r^2}{\Delta}m_a^2 - \frac{l(l+1)}{\Delta}\right]\Delta^{1/2}R(r) = 0. \tag{A.27}$$

In the far region we have that $r \gg M$ and thus $2M/r \ll 1$ so

$$\frac{r^4}{\Delta^2} \approx 1 + 2\frac{2M}{r},\ \frac{r^2}{\Delta} \approx 1 + \frac{2M}{r}, \tag{A.28}$$

and

$$\Delta^{1/2} \approx r(1 - \frac{M}{r}) = r - M \approx r. \tag{A.29}$$

The far region equation is then approximetly

$$\partial_r^2\left(rR(r)\right) + \left[\omega^2 - m_a^2 + \frac{4M\omega^2 - 2Mm_a^2}{r} - \frac{l(l+1)}{r^2}\right] rR(r) = 0. \tag{A.30}$$

Here we define

$$z = kr = 2(m_a^2 - \omega^2)^{1/2}r \tag{A.31}$$

and

$$\nu = \frac{4M\omega^2 - 2Mm_a^2}{k}, \tag{A.32}$$

which changes the equation to the shape of equation eq. (13.1.31) in Ref. [99],

$$\partial_z^2(zR) + \left[-\frac{1}{4} + \frac{\nu}{z} - \frac{l(l+1)}{z^2}\right] zR = 0, \tag{A.33}$$

which has the solution

$$zR = Be^{-\frac{1}{2}z}z^{l+1}U(l+1-\nu, 2l+2, z), \tag{A.34}$$

where U is a confluent hypergeometric function. In the overlap we have small z where U behaves as

$$U(\tilde{a}, \tilde{b}, z) \approx \frac{\pi}{\sin\left(\pi\tilde{b}\right)}\left(\frac{1}{\Gamma(1+\tilde{a}-\tilde{b})\Gamma(\tilde{b})} - z^{1-\tilde{b}}\frac{1}{\Gamma(\tilde{a})\Gamma(2-\tilde{b})}\right), \tag{A.35}$$

which means that we have the far region solution

$$R_{far}(r) \approx Be^{-kr/2}\frac{\pi}{\sin(\pi(2l+2))}\left(\frac{1}{\Gamma(-l-\nu)\Gamma(2l+2)}(kr)^l - \frac{1}{\Gamma(1+l-\nu)\Gamma(-2l)}(kr)^{-l-1}\right) \quad \text{(A.36)}$$

in the middle region.

A.3.4 Matching far and near regions

Comparing the near and far solutions in the middle region, i.e. eqs. (A.24) and (A.36), we see that we have one r^l term and one r^{-l-1} term in both. If the solutions are equal in the middle region then the ratio between these two terms should also be equal which give the equation

$$-\frac{\Gamma(-l-\nu)\Gamma(2l+2)}{\Gamma(1+l-\nu)\Gamma(-2l)}k^{-2l-1} = \frac{\Gamma(l+1)\Gamma(-2l-1)\Gamma(l+1-2\mathrm{i}\varpi)}{\Gamma(2l+1)\Gamma(-l)\Gamma(-l-2\mathrm{i}\varpi)}(r_+ - r_-)^{2l+1}. \quad \text{(A.37)}$$

Here we can use the expression

$$\frac{\Gamma(l+1-2\mathrm{i}\varpi)}{\Gamma(-l-2\mathrm{i}\varpi)} = (-1)^{l+1}2\mathrm{i}\varpi\prod_{j=1}^{l}(j^2+4\varpi^2), \quad \text{(A.38)}$$

which can be derived from $\Gamma(x+1) = x\Gamma(x)$ [25, 62], and we have

$$\frac{\Gamma(-l-\nu)}{\Gamma(1+l-\nu)\Gamma(-2l)} = (-1)^l 2\mathrm{i}\varpi((r_+-r_-)k)^{2l+1} \times \frac{(2l+1)!l!}{(2l)!}\frac{\Gamma(-2l-1)}{\Gamma(-l)}\prod_{j=1}^{l}(j^2+4\varpi^2). \quad \text{(A.39)}$$

To go further, we need to handle negative integers in the Γ-function. In general we simply want to apply the formula

$$\frac{\Gamma(-n)}{\Gamma(-m)} = \frac{(-1)^{(n-m)}m!}{n!}. \quad \text{(A.40)}$$

However, we need to be very careful with a detail often left out in the literature. The formula above only applies in the simultaneous limit and we have an additional negative sign when we approach integer values from different directions, i.e.

$$\lim_{\delta\to 0}\frac{\Gamma(-n+\delta)}{\Gamma(-m+\delta)} = \frac{(-1)^{(n-m)}m!}{n!} = -\lim_{\delta\to 0}\frac{\Gamma(-n+\delta)}{\Gamma(-m-\delta)}. \quad \text{(A.41)}$$

Thus, to continue we have to remember the definition of l from eq. (A.7). In reality we have $l+\delta$ where $\delta \ll \alpha \ll 1$ and practically we take $\delta \to 0$. This does not come

into play in the derivation until now when applying formula (A.40). We first apply the formula to the right-hand side of eq. (A.39) where the original form is valid and get

$$\frac{\Gamma(-l-\nu)}{\Gamma(1+l-\nu)\Gamma(-2l)} = -\mathrm{i}2\varpi((r_+-r_-)k)^{2l+1}\frac{(l!)^2}{((2l+1)!)^2(2l)!}\prod_{j=1}^{l}(j^2+4\varpi^2). \quad \text{(A.42)}$$

Here we notice that the right-hand side of eq. (A.42) are proportional to a factor k^{2l+1} and since $k \ll 1$ when $m_a \sim \omega$ this side is very suppressed. We can, therefore, define the function

$$G(\nu) = \frac{\Gamma(-l-\nu)}{\Gamma(1+l-\nu)\Gamma(-2l)}, \quad \text{(A.43)}$$

and $\nu = \nu_0 + \delta\nu$ where $G(\nu_0) = 0$. The first order contribution yields the equation

$$\Gamma(\nu_0) = \frac{\Gamma(-l-\nu_0)}{\Gamma(1+l-\nu_0)\Gamma(-2l)} = 0. \quad \text{(A.44)}$$

Through formula (A.40), we have that $\Gamma(-l-\nu_0)/\Gamma(-2l)$ are finite if $-l-\nu_0 = -m$ is an negative integer, and $1/\Gamma(l+1-\nu_0) = 0$ if $l+1-\nu_0 = -n$ also is a negative integer. These can both be satisfied since $m = n+2l+1$ and l is an integer in the limit wen are interested in. Since $\nu = \nu_0 + \delta\nu$ we can also split $\omega = \omega_0 + \delta\omega$ and we can extract ω_0 through eqs. (A.31)-(A.32) as

$$\omega_0^2 = m_a^2 - \frac{m_a^4 M^2}{\nu_0^2} - 4\frac{M^2}{\nu_0^2}(\omega_0^2 - m_a^2). \quad \text{(A.45)}$$

To second order in α we can neglect the third term here and we have

$$\omega_0 \approx m_a\left(1 - \frac{\alpha^2}{2(n+l+1)}\right). \quad \text{(A.46)}$$

These are the hydrogen like energy levels of the superradiant modes where $n+l+1$ can be compared to the principle quantum number, and we get the condition $l < n+l+1$ from the fact that $m = -l-\nu_0$ has to be positive.

Since ω_0 is real, we have to go to the next order contribution to extract the superraiant rates. We do this by Taylor expansion of G:

$$G(\nu_0+\delta\nu) = G(\nu_0) + \frac{\Gamma(-m)}{\Gamma(-n)\Gamma(-2l)}\left(\psi(-n) - \psi(-m)\right)\delta\nu, \quad \text{(A.47)}$$

where $\psi(z) = \Gamma'(z)/\Gamma(z)$ is the digamma function, which has the property

$$\frac{\psi(-z)}{\Gamma(-z)} = (-1)^{z+1}z! \quad \text{(A.48)}$$

in the limit where z goes to a positive integer. With this we have

$$G(\nu_0+\delta\nu)=\frac{\Gamma(-m)}{\Gamma(-2l)}\left((-1)^{n+1}n!-\frac{\Gamma(-m)}{\Gamma(-n)}(-1)^{m+1}m!\right)\delta\nu. \tag{A.49}$$

$-m$ behaves as $-l$ and therefore we can apply (A.40) directly on the first factor, where as $-n$ behaves as l and we have to remember eq. (A.41) in the second term. With this in mind we have have

$$G(\nu_0+\delta\nu)=(-1)^{m-2l}\frac{(2l)!}{m!}\left((-1)^{n+1}n!+(-1)^{2m-n+1}n!\right)\delta\nu, \tag{A.50}$$

where we use $m=n+2l+1$ and get

$$G(\nu_0+\delta\nu)=2\frac{(2l)!n!}{(n+2l+1)!}\delta\nu. \tag{A.51}$$

With this in eq. (A.42) we can express

$$\delta\nu=-\mathrm{i}\varpi_0((r_+-r_-)k_0)^{2l+1}\left(\frac{l!}{(2l+1)!(2l)!}\right)^2\frac{(n+2l+1)!}{n!}\prod_{j=1}^{l}(j^2+4\varpi_0^2), \tag{A.52}$$

where $\varpi_0=\varpi(\omega_0)$ and

$$k_0=k(\omega_0)=2(m_a^2-\omega_0^2)^{1/2}\approx 2\frac{Mm_a^2}{(n+l+1)} \tag{A.53}$$

is the corresponding first order contributions. To extract $\delta\omega$ we use

$$\delta\nu=\left.\frac{\partial\nu}{\partial\omega}\right|_{\omega=\omega_0}\delta\omega=\left(\omega_0 M\frac{3m_a^2-2\omega_0^2}{(m_a^2-\omega_0^2)^{3/2}}\right)\delta\omega, \tag{A.54}$$

and with the same expression as for k_0 we have

$$\delta\omega=\delta\nu\frac{\frac{M^3m_a^6}{(n+l+1)^3}}{\omega_0 M\left(m_a^2+2\frac{M^2m_a^4}{(n+l+1)^2}\right)}=\delta\nu\frac{M^2m_a^3}{(n+l+1)^3}+O(\alpha^3), \tag{A.55}$$

where we have used $\omega_0=m_a(1+O(\alpha^2))$ to get the first order contribution. Inserting $\delta\nu$ from eq. (A.52) with the expression for k_0 we have

$$\begin{aligned}\delta\omega=&-\mathrm{i}2^{2l+1}\varpi_0(r_+-r_-)^{2l+1}M^{2l+3}m_a^{4l+5}\\&\times\left(\frac{l!}{(2l+1)!(2l)!}\right)^2\frac{(n+2l+1)!}{n!(n+l+1)^{2l+4}}\prod_{j=1}^{l}(j^2+4\varpi_0^2).\end{aligned} \tag{A.56}$$

What we have left to insert is

$$\varpi_0 = (\omega_0 - m\Omega)\frac{r_+^2}{(r_+ - r_-)}, \tag{A.57}$$

doing so we can express $\delta\omega$ as

$$\begin{aligned}\delta\omega &= 2^{2l+1}\mathrm{i}M^{2l+3}m_a^{4l+5}(m\Omega-\omega_0)r_+^{2l+2}\\ &\times\left(\frac{l!}{(2l+1)!(2l)!}\right)^2\frac{(n+2l+1)!}{(n+l+1)^{2l+4}n!}\prod_{j=1}^{l}\left(j^2\left(1-\frac{r_-}{r_+}\right)^2+4r_+^2(m\Omega-\omega_0)^2\right).\end{aligned} \tag{A.58}$$

As a last step we use that $r_+ \approx 2M$ and $r_- \approx a$ in the slow rotation limit and get

$$\delta\omega = \mathrm{i}\alpha^{4l+5}(m\Omega-\omega_0)C_{nlm}, \tag{A.59}$$

where

$$\begin{aligned}C_{nlm} = 2^{4l+3}&\left(\frac{l!}{(2l+1)!(2l)!}\right)^2\frac{(n+2l+1)!}{(n+l+1)^{2l+4}n!}\\ &\times\prod_{j=1}^{l}\left(j^2\left(1-\frac{a}{2M}\right)^2+16M^2(m\Omega-\omega_0)^2\right).\end{aligned} \tag{A.60}$$

A.4 Summary

Above we found the energy eigenvalues of the supperradiant modes, and they could be split as $\omega = \omega_0 + \delta\omega$ where the parts are found in eqs. (A.46) and (A.59) respectively. One usually redefine these as

$$\omega = \omega_{nlm} + \mathrm{i}\Gamma_{nlm}, \tag{A.61}$$

where nlm resembles the hydrogen quantum numbers with $n+l+1$ as the principle quantum number. The energy levels ω_{nlm} behaves exactly as the hydrogen modes and the major difference is the imaginary part, which gives rise to the exponential growth in the field when the superradiant condition

$$m\Omega > \omega_{nlm} \tag{A.62}$$

is satisfied. The rate Γ_{nlm} derived in this appendix is only slightly less general than the one presented in chapter 2 from Ref. [29]. The most important feature is the superradiant condition, the α^{4l+5} behavior, and that the rate of the dominant mode, $n = 0$ and $l = m = 1$, can be found to first order in α in the slow rotation limit as[1]

$$\Gamma_{011} = \frac{a}{M}\frac{\alpha^9}{12M}. \tag{A.63}$$

[1]Somewhere in the derivation in this appendix we have lost a factor ofs 2 compared to generally accepted solution, see eq. (2.22).

Appendix B

The Novikov–Thorne Disk

In this appendix we present the details of the accretion disk model by Novikov and Thorne we used in chapter 3. The source for this appendix is Refs. [47, 66] and further details can be found in those.

The Novikov–Thorne disk is the relativistic extenstion of the thin-disk model of Shakura and Sunjaev disk [67]. Through some small extra assumptions the relevant equation describing the flow of the accreted matter can be solved algebraically in three distinct radial regions characterized by the dominant pressure. In the innermost region, the radiation pressure dominates, while in the outer two, the gas pressure dominates. The difference between the outer and the middle region is the process that determines the opacity. In the middle region, electron scattering dominates, whereas free-free absorption is the most important in the outer region. In each region the particle density n, the temperature T, and the thickness of the disk H can be found as function of multiple parameters. The expressions for these are given bellow for each region. The parameters these functions depend on are: the radius, which in the expressions has been normalized to r_g; the mass of the black hole, $m = M/M_\odot$; the accretion rate, $\dot{m}$, which we have normalized according to eq. (2.35); and a parameter α, which describes the efficiency of the momentum transport. The profiles are also proportional to $\mathcal{A}-\mathcal{E}$ and $\mathcal{Q}$ which are functions of r and the the dimensionless spin, $a_* = a/M$ given further below in this appendix.

In the inner region we have

$$n = \left[1 \times 10^{17}\,\mathrm{cm}^{-3}\right] \alpha_p^{-1} \dot{m}^{-2} m^{-1} r^{\frac{3}{2}} \mathcal{A}^{-4} \mathcal{B}^{6} \mathcal{D} \mathcal{E}^{2} \mathcal{Q}^{-2}, \tag{B.1}$$

$$T = \left[5 \times 10^{7}\,\mathrm{K}\right] \alpha_p^{-\frac{1}{4}} m^{-\frac{1}{4}} r^{-\frac{3}{8}} \mathcal{A}^{-\frac{1}{2}} \mathcal{B}^{\frac{1}{2}} \mathcal{E}^{\frac{1}{4}}, \tag{B.2}$$

$$h = \left[2 \times 10^{6}\,\mathrm{cm}\right] \dot{m} m \mathcal{A}^{2} \mathcal{B}^{-3} \mathcal{C}^{\frac{1}{2}} \mathcal{D}^{-1} \mathcal{E}^{-1} \mathcal{Q}. \tag{B.3}$$

This region extends down to the ISCO and transitions to the middle region at r_{in} which is given by the implicit equation

$$r_{in} = 5.2 \times 10^{2} \alpha^{\frac{2}{21}} m^{\frac{2}{15}} \dot{m}^{\frac{4}{5}} \mathcal{A}^{\frac{20}{21}} \mathcal{B}^{-\frac{36}{21}} \mathcal{D}^{-\frac{8}{21}} \mathcal{E}^{-\frac{10}{21}} \mathcal{Q}^{\frac{16}{21}}, \tag{B.4}$$

where $\mathcal{A} - \mathcal{Q}$ all depend on r_{in}. Typical values of r_{in} is $\sim 1 - 10$ for SMBHs and $\sim 50 - 100$ for stellar black holes.

The middle region is described by

$$n = \left[6 \times 10^{25}\,\mathrm{cm}^{-3}\right] \alpha_p^{-\frac{7}{10}} \dot{m}^{\frac{2}{5}} m^{-\frac{7}{10}} r^{-\frac{33}{20}} \mathcal{A}^{-1} \mathcal{B}^{\frac{3}{5}} \mathcal{D}^{-\frac{1}{5}} \mathcal{E}^{\frac{1}{2}} \mathcal{Q}^{\frac{2}{5}}, \tag{B.5}$$

$$T = \left[2 \times 10^{9}\,\mathrm{K}\right] \alpha_p^{-\frac{1}{5}} \dot{m}^{\frac{2}{5}} m^{-\frac{1}{5}} r^{-\frac{9}{10}} \mathcal{B}^{-\frac{2}{5}} \mathcal{D}^{-\frac{1}{5}} \mathcal{Q}^{\frac{2}{5}}, \tag{B.6}$$

$$h = \left[3 \times 10^{3}\,\mathrm{cm}\right] 3.2 \alpha_p^{-\frac{1}{10}} \dot{m}^{\frac{1}{5}} m^{\frac{9}{10}} r^{\frac{21}{20}} \mathcal{A} \mathcal{B}^{-\frac{6}{5}} \mathcal{C}^{\frac{1}{2}} \mathcal{D}^{-\frac{3}{5}} \mathcal{E}^{-\frac{1}{2}} \mathcal{Q}^{\frac{1}{5}}, \tag{B.7}$$

and is valid between r_{in} and r_{out} where r_{out} is given by the explicit equation

$$r_{out} = 1.9 \times 10^{4} \dot{m}^{2/3} \mathcal{A}^{\frac{2}{3}} \mathcal{B}^{-\frac{8}{15}} \mathcal{D}^{-\frac{1}{3}} \mathcal{E}^{-\frac{1}{3}} \mathcal{Q}^{\frac{2}{3}}. \tag{B.8}$$

r_{out} is around 100 for most SMBHs and ranges between $10^3 - 10^4$ for stellar black holes.

The outer region is space outside of r_{out} and where

$$n = \left[8 \times 10^{26}\,\mathrm{cm}^{-3}\right] \alpha_p^{-\frac{7}{10}} \dot{m}^{\frac{11}{20}} m^{-\frac{7}{10}} r^{-\frac{15}{8}} \mathcal{A}^{-\frac{17}{20}} \mathcal{B}^{\frac{3}{10}} \mathcal{D}^{-\frac{11}{40}} \mathcal{E}^{\frac{17}{40}} \mathcal{Q}^{\frac{11}{20}}, \tag{B.9}$$

$$T = \left[4 \times 10^{8}\,\mathrm{K}\right] \alpha_p^{-\frac{1}{5}} \dot{m}^{\frac{3}{10}} m^{-\frac{1}{5}} r^{-\frac{3}{4}} \mathcal{A}^{-\frac{1}{10}} \mathcal{B}^{-\frac{1}{5}} \mathcal{D}^{-\frac{3}{20}} \mathcal{E}^{\frac{1}{20}} \mathcal{Q}^{\frac{3}{10}}, \tag{B.10}$$

$$h = \left[1 \times 10^{3}\,\mathrm{cm}\right] \alpha_p^{-\frac{1}{10}} \dot{m}^{\frac{3}{20}} m^{\frac{9}{10}} r^{\frac{9}{8}} \mathcal{A}^{\frac{19}{20}} \mathcal{B}^{-\frac{11}{10}} \mathcal{C}^{\frac{1}{2}} \mathcal{D}^{-\frac{23}{40}} \mathcal{E}^{-\frac{19}{40}} \mathcal{Q}^{\frac{3}{20}}. \tag{B.11}$$

The functions $\mathcal{A}$ to $\mathcal{E}$ are defined as

$$\mathcal{A} = 1 + a_*^2 r^{-2} + 2a_*^2 r^{-3}, \tag{B.12}$$

$$\mathcal{B} = 1 + a_* r^{-3/2}, \tag{B.13}$$

$$\mathcal{C} = 1 - 3r^{-1} + 2a_* r^{-3/2}, \tag{B.14}$$

$$\mathcal{D} = 1 - 2r^{-1} + a_*^2 r^{-2}, \tag{B.15}$$

$$\mathcal{E} = 1 + 4a_*^2 r^{-2} - 4a_*^2 r^{-3} + 3a_*^4 r^{-4}, \tag{B.16}$$

and $\mathcal{Q}$ is given by

$$\begin{aligned} \mathcal{Q} = \mathcal{Q}_0 \Bigg[& y - y_0 - \frac{3}{2} \ln\left(\frac{y}{y_0}\right) - \frac{3(y_1 - a_*)^2}{y_1(y_1 - y_2)(y_1 - y_3)} \ln\left(\frac{y - y_1}{y_0 - y_1}\right) \\ & - \frac{3(y_2 - a_*)^2}{y_2(y_2 - y_1)(y_2 - y_3)} \ln\left(\frac{y - y_2}{y_0 - y_2}\right) - \frac{3(y_3 - a_*)^2}{y_3(y_3 - y_1)(y_3 - y_2)} \ln\left(\frac{y - y_3}{y_0 - y_3}\right) \Bigg], \end{aligned} \tag{B.17}$$

where

$$\mathcal{Q}_0 = \frac{1 + a_* r^{-3/2}}{(r - 3 + 2a_* r^{-1/2})^{1/2}},$$
$$y = \sqrt{r},$$
$$y_0 = \sqrt{r_{ISCO}},$$
$$y_1 = 2\cos(\arccos(a_*) - \pi)/3),$$
$$y_2 = 2\cos(\arccos(a_*) + \pi)/3),$$
$$y_3 = -2\cos(\arccos(a_*)/3).$$

Appendix C

Matrix elements

In this appendix we present the details for deriving the matrix elements used in chapter 3. We have the interaction

$$e + a \to e + \gamma \tag{C.1}$$

which have three tree-level contributions shown in figure 3.1. We denote the four momenta for the initial particles as p_i, $i = e, a$, and the final momenta as q_i, $i = e, \gamma$. For the Feynman algebra we use common notation that can be found in, for example, Ref. [95].

C.1 The Primakoff channel

The tree-level Feynman diagram for the Primakoff channel is shown in figure 3.1c. To find the matrix element for this we need the axion-photon vertex, which can be derived from expression (2.2) to

$$\mathrm{i}g_{a\gamma}\epsilon^{\mu\nu\rho\sigma}p_\nu q_\rho, \tag{C.2}$$

where p and q are the photon momenta, and ϵ is the four dimensional Levi-Civita tensor. With this and normal Feynman rules we have that

$$\begin{aligned}\mathrm{i}\mathcal{M} &= \varepsilon^*_\rho(q_\gamma)\bar{u}(q_e)\left(\mathrm{i}e\gamma^\alpha\right)u(p_e)\frac{-\mathrm{i}g_{\alpha\mu}}{(p_a - q_\gamma)^2}\mathrm{i}\epsilon^{\mu\nu\rho\sigma}\left(p_a - q_\gamma\right)_\nu\left(q_\gamma\right)_\sigma \\ &= \mathrm{i}\frac{eg_{a\gamma}}{t}\varepsilon^*_\rho(q_\gamma)\bar{u}(q_e)\gamma_\mu u(p_e)\epsilon^{\mu\nu\rho\sigma}\left(p_a - q_\gamma\right)_\nu\left(q_\gamma\right)_\sigma,\end{aligned} \tag{C.3}$$

where $t = (p_a - q_\gamma)$ is the usual Mandelstam variable, ε is the polarization vectos of the photon, and u is the electron spinnors. Averaging over initial spins and

summing over outgoing yields

$$\langle|\mathcal{M}|^2\rangle = \frac{e^2 g_{a\gamma}^2}{2t^2}(-g_{\rho r})\,\mathrm{Tr}\Big(\gamma_\mu(\not{p}_e + m_e)\gamma_m(\not{q}_e + m_e)\Big) \\ \times \epsilon^{\mu\nu\rho\sigma}\epsilon^{mnrs}\,(p_a - q_\gamma)_\nu\,(q_\gamma)_\sigma\,(p_a - q_\gamma)_n\,(q_\gamma)_s. \quad \text{(C.4)}$$

Simplifying this in *Mathematica* using *FeynCalc* [100] we have

$$\langle|\mathcal{M}|^2\rangle = \frac{4e^2 g_{a\gamma}^2}{t^2}\,(p_a\cdot q_e p_a\cdot q_\gamma p_e\cdot q_\gamma + p_a\cdot p_e p_a\cdot q_\gamma q_e\cdot q_\gamma \\ -p_a^2 p_e\cdot q_\gamma q_e\cdot q_\gamma - q_\gamma^2 p_a\cdot p_e p_a\cdot q_e + m_e^2\left(p_a^2 q_\gamma^2 - (p_a\cdot q_\gamma)^2\right)). \quad \text{(C.5)}$$

In the main part of the thesis we are interested in axions approximately at rest. In this frame we can derive the following expressions for the Mandelstam variables and relevant dot products:

$$\begin{aligned} s &= m_a^2 + m_e^2 + 2E_e m_a,\\ t &= m_a^2 - 2m_a E_\gamma,\\ u &= m_e^2 - m_a^2 + 2m_a(E_\gamma - E_e),\\ p_a\cdot q_\gamma &= m_a E_\gamma,\\ p_a\cdot p_e &= m_a E_e,\\ p_e\cdot q_\gamma &= m_a^2/2 - m_a(E_\gamma - E_e),\\ p_e\cdot q_e &= m_e^2 - m_a^2/2 + m_a E_\gamma,\\ p_a\cdot q_e &= m_a^2 - m_a(E_\gamma - E_e),\\ q_e\cdot q_\gamma &= m_a^2/2 + m_a E_e. \end{aligned}$$

Inserting these in the matrix we have

$$\langle|\mathcal{M}|^2\rangle = \frac{64\pi\alpha_{em} g_{a\gamma}^2}{(2E_\gamma - m_a)^2}\Big(2E_e^2 E_\gamma m_a - E_e^2 m_a^2 - E_\gamma^2 m_e^2 \\ +3E_e E_\gamma m_a^2 - 2E_e E_\gamma^2 m_a - E_e m_a^3 + E_\gamma^3 m_a - \frac{3}{2}E_\gamma^2 m_a^2 + E_\gamma m_a^3 - \frac{1}{4}m_a^4\Big). \quad \text{(C.6)}$$

To simplify the calculations in the main part we introduced the dimensionless quantities $x = E_e/m_e$, $\xi = E_\gamma/m_a$, and $\epsilon = m_a/m_e$ with which have the final result

$$|\mathcal{M}|^2 = \frac{64\pi\alpha_{em} g_{a\gamma} m_e^2}{(2\xi - 1)^2}\left((x^2(2\xi - 1) - \xi^2)\right. \\ \left. +\epsilon x\left(3\xi - 2\xi^2 - 1\right) + \epsilon^2\left(\xi^3 - \frac{3}{2}\xi^2 + \xi - \frac{1}{4}\right)\right). \quad \text{(C.7)}$$

C.2 The Compton channel

To calculate the matrix elements for the Compton channel we need the axion-electron vertex which can be derived from eq. (2.4) to

$$\frac{\mathrm{i}g_{ae}}{2m_e}\not{p}_a\gamma_5. \tag{C.8}$$

The Compton channel has two tree-level contributions, see figures 3.1a and 3.1b. The first we call the s-contribution for which the matrix element is

$$\begin{aligned}\mathrm{i}\mathcal{M} &= \varepsilon^*_\mu(q_e)\bar{u}(q_e)\left(\mathrm{i}\gamma^\mu e\right)\frac{\mathrm{i}(\not{p}_a+\not{p}_e+m_e)}{s-m_e^2}\frac{-\mathrm{i}g_{ae}}{2m_e}\not{p}_a\gamma_5 u(p_e)\\ &= \mathrm{i}\frac{eg_{ae}}{2m_e(s-m_e^2)}\varepsilon^*_\mu(q_e)\bar{u}(q_e)\gamma^\mu\left(\not{p}_a+\not{p}_e+m_e\right)\not{p}_a\gamma_5 u(p_e).\end{aligned} \tag{C.9}$$

Similarly we have the u-contribution which have the matrix element

$$\mathrm{i}\mathcal{M}_u = \mathrm{i}\frac{eg_{ae}}{2m_e(u-m_e^2)}\varepsilon^*_\mu(q_e)\bar{u}(q_e)\not{p}_a\gamma_5\left(\not{p}_e-\not{q}_\gamma+m_e\right)\gamma^\mu u(p_e). \tag{C.10}$$

The total matrix element is then $\mathcal{M}=\mathcal{M}_s+\mathcal{M}_u$ and we have

$$|\mathcal{M}|^2 = \frac{\pi\alpha_{em}g_{ae}^2}{m_e^2}\left(\varepsilon^*_\mu(q_e)\bar{u}(q_e)C^\mu u(p_e)\right)\left(\varepsilon^*_\nu(q_e)\bar{u}(q_e)C^\nu u(p_e)\right)^*, \tag{C.11}$$

where we have defined

$$C^\mu = \gamma^\mu\frac{\left(\not{p}_a+\not{p}_e+m_e\right)}{s-m_e^2}\not{p}_a\gamma_5 + \not{p}_a\gamma_5\frac{\left(\not{p}_e-\not{q}_\gamma+m_e\right)}{u-m_e^2}\gamma^\mu. \tag{C.12}$$

Averaging over the incoming particles and summing over the outgoing we get

$$\langle|\mathcal{M}|^2\rangle = \frac{\pi\alpha_{em}g_{ae}^2}{2m_e^2}\left(-g_{\mu\nu}\right)\mathrm{Tr}\Big(C^\mu(\not{p}_e+m_e)\bar{C}^\nu(\not{q}_e+m_e)\Big), \tag{C.13}$$

where

$$\bar{C}^\nu = \gamma^0\left(C^\nu\right)^\dagger\gamma^0 = \not{p}_a\gamma_5\frac{\left(\not{p}_a+\not{p}_e+m_e\right)}{s-m_e^2}\gamma^\mu + \gamma^\mu\frac{\left(\not{p}_e-\not{q}_\gamma+m_e\right)}{u-m_e^2}\not{p}_a\gamma_5. \tag{C.14}$$

The trace algebra is easily done in *FeynCalc* [100] and inserting the Mandelstam variables and dot products from the previous section we find

$$\begin{aligned}\langle|\mathcal{M}|^2\rangle = &\frac{16\pi\alpha_{em}g_{ae}^2}{(2E_e+m_a)(2E_e-2E_\gamma+m_a)}\\ &\times\left(m_a^2+2E_\gamma-2E_\gamma m_a+\frac{4E_\gamma^2m_e^2}{(2E_e+m_a)(2E_e-2E_\gamma+m_a)}\right).\end{aligned} \tag{C.15}$$

Finally, we use the dimensionless quantities x, ξ, and ϵ and end at

$$\langle|\mathcal{M}|^2\rangle = \frac{16\pi\alpha_{em}g_{ae}^2\epsilon^2}{(2x+\epsilon)(2x-2\epsilon\xi+\epsilon)}\left(1+2\xi^2-2\xi+\frac{4\xi^2}{(2x+\epsilon)(2x-2\epsilon\xi+\epsilon)}\right). \tag{C.16}$$

Appendix D

Modified Maxwell's equations

Including the axion-photon coupling yields the following modified Maxwell's equations [83, 101]

$$\nabla \cdot \mathbf{E} = \rho - g_{a\gamma}\mathbf{B} \cdot \nabla a, \tag{D.1}$$

$$\nabla \times \mathbf{B} - \partial_t \mathbf{E} = \mathbf{J} + g_{a\gamma}\left(\mathbf{B}\partial_t a - \mathbf{E} \times \nabla a\right), \tag{D.2}$$

$$\nabla \cdot \mathbf{B} = 0, \tag{D.3}$$

$$\nabla \times \mathbf{E} + \partial_t \mathbf{B} = 0, \tag{D.4}$$

$$-\partial_t^2 a + \nabla^2 a = m_a^2 a - g_{a\gamma}\mathbf{E} \cdot \mathbf{B}. \tag{D.5}$$

We are interested in resonant conversion of axions into photons in an external magnetic field, this will occur in a relative small area around a black hole and we can therefore neglect any relativistic effects. We will consider the axions and electric field to be plane waves moving in the z-direction, i.e.

$$a = \tilde{a}(z)e^{\mathrm{i}\omega t - \mathrm{i}kz} \text{ and } \mathbf{E} = \begin{pmatrix} E_x \\ E_y \\ E_z \end{pmatrix} e^{\mathrm{i}\omega t - \mathrm{i}kz}, \tag{D.6}$$

where $\omega \approx m_a$ is the frequency and $k \approx m_a\alpha/2$ is the wave number. Further, we choose our coordinates so that the external magnetic field takes the form

$$\mathbf{B}_e = B_e \begin{pmatrix} 0 \\ \sin\theta \\ \cos\theta \end{pmatrix}. \tag{D.7}$$

In this coordinate system eq. (D.5) becomes

$$\omega^2\tilde{a} + \partial_z^2\tilde{a} = m_a^2\tilde{a} - g_{a\gamma}B_e\left(E_y \sin\theta + E_z\cos\theta\right). \tag{D.8}$$

With the remaining equations, eqs. (D.1)-(D.4), one can derive the following equation for the propagation of the electric field [48]

$$-\nabla^2\mathbf{E}+\nabla(\nabla\cdot\mathbf{E})=\omega^2\mathbf{D}+\omega^2 g_{a\gamma}a\mathbf{B}_e, \tag{D.9}$$

where $\mathbf{D}$ is the electric displacement field imposed by the magnetic field given by

$$\mathbf{D}=R_{yz}(\theta)\begin{pmatrix}\epsilon,\mathrm{i}g,0\\-\mathrm{i}g,\epsilon,0\\0,0,\eta\end{pmatrix}R_{yz}(-\theta). \tag{D.10}$$

The elements are defined as

$$\epsilon=1-\frac{\omega_{pl}}{\omega^2-\Omega_c^2},\ g=\frac{\omega_{pl}^2\Omega_c}{\omega(\omega^2-\Omega_c^2)}\text{ and }\eta=1-\frac{\omega_{pl}^2}{\omega^2}, \tag{D.11}$$

where $\Omega_c=\sqrt{\alpha_{em}}B_e/m_e$, and R_{yz} are rotation matrices. If the magnitude of the external magnetic field satisfy

$$\frac{\sqrt{\alpha}_{em}B_e}{m_e}\gg m_a\approx\omega_{pl}, \tag{D.12}$$

then $\epsilon\to 1$ and $g\to 0$, this decouples E_x from the other components. Since E_z does not propagate we then have

$$\begin{pmatrix}-\partial_z^2E_y\\0\end{pmatrix}=\omega^2\begin{pmatrix}1-\frac{\omega_{pl}^2}{\omega^2}\sin^2\theta & -\frac{\omega_{pl}^2}{\omega^2}\sin\theta\cos\theta\\-\frac{\omega_{pl}^2}{\omega^2}\sin\theta\cos\theta & 1-\frac{\omega_{pl}^2}{\omega^2}\cos^2\theta\end{pmatrix}\begin{pmatrix}E_y\\E_z\end{pmatrix}+g_{a\gamma}\omega^2\tilde{a}B_e\begin{pmatrix}\sin\theta\\\cos\theta\end{pmatrix}. \tag{D.13}$$

From this E_z can be solved for algebraically, and substituting it into the equation for E_y and eq. (D.8) we get the following equation

$$-\partial_z^2\begin{pmatrix}E_y\\\tilde{a}\end{pmatrix}=\begin{pmatrix}\frac{\omega^2-\omega_{pl}^2}{1-\frac{\omega_{pl}^2}{\omega^2}\cos^2\theta} & \frac{g_{a\gamma}\omega^2B_e\sin\theta}{1-\frac{\omega_{pl}^2}{\omega^2}\cos^2\theta}\\\frac{g_{a\gamma}B_e\sin\theta}{1-\frac{\omega_{pl}^2}{\omega^2}\cos^2\theta} & \omega^2-m_a^2-\frac{g_{a\gamma}^2B_e^2\cos^2\theta}{1-\frac{\omega_{pl}^2}{\omega^2}\cos^2\theta}\end{pmatrix}\begin{pmatrix}E_y\\\tilde{a}\end{pmatrix}, \tag{D.14}$$

which describes the mixing between a and E_y. We can neglect the term proportional to $g_{a\gamma}^2$ since we are typically interested in magnetic fields much smaller than $1\times 10^8\,\mathrm{G}\approx 1\times 10^6\,\mathrm{eV}^2$, which yields $g_{a\gamma}B\ll 1\times 10^{-13}\,\mathrm{eV}\approx m_a$ for the values of $g_{a\gamma}$ and m_a we are interested in. We then have the equation

$$-\partial_z^2\begin{pmatrix}E_y\\\tilde{a}\end{pmatrix}=\begin{pmatrix}\frac{\omega^2-\omega_{pl}^2}{1-\frac{\omega_{pl}^2}{\omega^2}\cos^2\theta} & \frac{g_{a\gamma}\omega^2B_e\sin\theta}{1-\frac{\omega_{pl}^2}{\omega^2}\cos^2\theta}\\\frac{g_{a\gamma}B_e\sin\theta}{1-\frac{\omega_{pl}^2}{\omega^2}\cos^2\theta} & \omega^2-m_a^2\end{pmatrix}\begin{pmatrix}E_y\\\tilde{a}\end{pmatrix}. \tag{D.15}$$

We want to express this in terms of the photon field transverse to the wave motion, $\tilde{A}_\parallel = E_y/\mathrm{i}\omega$, instead of the electric field. If we also redefine $\tilde{a} \to \mathrm{i}\tilde{a}$ and $z = r$ we can rewrite the equation as

$$-\partial_r^2 \begin{pmatrix} \tilde{A}_\parallel \\ \tilde{a} \end{pmatrix} = \begin{pmatrix} \frac{\omega^2-\omega_{pl}^2}{1-\frac{\omega_{pl}^2}{\omega^2}\cos^2\theta} & \frac{g_{a\gamma}\omega B_e \sin\theta}{1-\frac{\omega_{pl}^2}{\omega^2}\cos^2\theta} \\ \frac{g_{a\gamma}\omega B_e \sin\theta}{1-\frac{\omega_{pl}^2}{\omega^2}\cos^2\theta} & \omega^2 - m_a^2 \end{pmatrix} \begin{pmatrix} \tilde{A}_\parallel \\ \tilde{a} \end{pmatrix}. \tag{D.16}$$

We have used expressions in the main work which are based on this mixing equation. However, condition (D.12) does not hold for the systems we consider in chapter 4. This is, fortunately, not a major problem. In general, we will have mixing between the axion and the transveres photon polarization independently of the magnitude of B_e [84], and the corrections should be minor if we consider magnetic fields that does not satisfy (D.12). For example, in the opposite limit, $\sqrt{\alpha_{em}}B_e/m_e \ll m_a$, $g \to 0$ and $\epsilon \to \eta$ close to r_c. Using this instead we end at the mixing equation of the form

$$-\partial_r^2 \begin{pmatrix} \tilde{A}_\parallel \\ \tilde{a} \end{pmatrix} = \begin{pmatrix} \omega^2 - \omega_{pl}^2 & g_{a\gamma}\omega B_e \sin\theta \\ g_{a\gamma}\omega B_e \sin\theta & \omega^2 - m_a^2 \end{pmatrix} \begin{pmatrix} \tilde{A}_\parallel \\ \tilde{a} \end{pmatrix}, \tag{D.17}$$

which is essentially the same as what is found in Ref. [84], but with the plasma frequency inserted as the mass of the photon. This is however different to eq. (D.16), but Ref. [48] argues that using $\theta = \pi/2$ gives the first order approximation in v_c, the axion velocity, and in that case eqs. (D.16) and (D.17) reduces to the same expression. Further, inserting $\theta = \pi/2$ from the beginning we arrive at the same expression independently of the magnetic field. We can therefore conclude that the expressions used in chapter 4 should hold to first order in α, since $v_c \approx \alpha/2$ in the axion cloud, independently on the strength of the magnetic field.

The last step in the derivation of both Refs. [48, 84] is to lineraize the equation through the WKB approximation which hold close to r_c where the matrix changes slowly compared to $1/k$, and we get the equation

$$2\mathrm{i}k\partial_r \begin{pmatrix} \tilde{A}_\parallel \\ \tilde{a} \end{pmatrix} = \begin{pmatrix} \frac{\omega^2-\omega_{pl}^2}{1-\frac{\omega_{pl}^2}{\omega^2}\cos^2\theta} & \frac{g_{a\gamma}\omega B_e \sin\theta}{1-\frac{\omega_{pl}^2}{\omega^2}\cos^2\theta} \\ \frac{g_{a\gamma}\omega B_e \sin\theta}{1-\frac{\omega_{pl}^2}{\omega^2}\cos^2\theta} & \omega^2 - m_a^2 \end{pmatrix} \begin{pmatrix} \tilde{A}_\parallel \\ \tilde{a} \end{pmatrix}, \tag{D.18}$$

where if we define

$$\xi = \frac{\sin^2\theta}{1-\frac{\omega_{pl}^2}{m_a^2}\cos^2\theta} \text{ and } \Delta_B = B_e g_{a\gamma} m_a \frac{\xi}{\sin\theta}, \tag{D.19}$$

we arrive at eq. (4.3).

Bibliography

[1] R. D. Peccei and H. R. Quinn, *CP Conservation in the Presence of Pseudoparticles*, Phys. Rev. Lett. **38**, 1440 (1977).

[2] R. D. Peccei and H. R. Quinn, *Constraints imposed by CP conservation in the presence of pseudoparticles*, Phys. Rev. D **16**, 1791 (1977).

[3] S. Weinberg, *A New Light Boson?*, Phys. Rev. Lett. **40**, 223 (1978).

[4] F. Wilczek, *Problem of Strong P and T Invariance in the Presence of Instantons*, Phys. Rev. Lett. **40**, 279 (1978).

[5] L. F. Abbott and P. Sikivie, *A cosmological bound on the invisible axion*, Phys. Lett. B **120**, 133 (1983).

[6] J. Preskill, M. B. Wise and F. Wilczek, *Cosmology of the invisible axion*, Phys. Lett. B **120**, 127 (1983).

[7] I. G. Irastorza and J. Redondo, *New experimental approaches in the search for axion-like particles*, Prog. Part. Nucl. Phys. **102**, 89 (2018).

[8] L. Di Luzio *et al.*, *The landscape of QCD axion models*, Phys. Rep. **870**, 1 (2020).

[9] A. Arvanitaki *et al.*, *String axiverse*, Phys. Rev. D **81**, 123530 (2010).

[10] CAST collaboration, V. Anastassopoulos *et al.*, *New CAST limit on the axion–photon interaction*, Nat. Phys. **13**, 584 (2017).

[11] The ADMX Collaboration, S. J. Asztalos *et al.*, *SQUID-Based Microwave Cavity Search for Dark-Matter Axions*, Phys. Rev. Lett. **104**, 041301 (2010).

[12] J. Redondo and A. Ringwald, *Light shining through walls*, Contemp. Phys. **52**, 211 (2011).

[13] D. A. Dicus *et al.*, *Astrophysical Bounds on the Masses of Axions and Higgs Particles*, Phys. Rev. D **18**, 1829 (1978).

[14] D. A. Dicus *et al.*, *Astrophysical Bounds on Very Low Mass Axions*, Phys. Rev. D **22**, 839 (1980).

[15] M. Fukugita, S. Watamura and M. Yoshimura, *Astrophysical constraints on a new light axion and other weakly interacting particles*, Phys. Rev. D **26**, 1840 (1982).

[16] G. G. Raffelt, *Astrophysical axion bounds diminished by screening effects*, Phys. Rev. D **33**, 897 (1986).

[17] A. Pantziris and K. Kang, *Axion Emission Rates in Stars and Constraints on Its Mass*, Phys. Rev. D **33**, 3509 (1986).

[18] G. G. Raffelt, *Astrophysical methods to constrain axions and other novel particle phenomena*, Phys. Rep. **198**, 1 (1990).

[19] E. W. Kolb and M. S. Turner, *The Early Universe* (Addison-Wesely Publishing Company, 1990).

[20] S. A. Teukolsky, *Rotating Black Holes: Separable Wave Equations for Gravitational and Electromagnetic Perturbations*, Phys. Rev. Lett. **29**, 1114 (1972).

[21] W. H. Press and S. A. Teukolsky, *Floating Orbits, Superradiant Scattering and the Black-hole Bomb*, Nature **238**, 211 (1972).

[22] T. J. Zouros and D. M. Eardley, *Instabilities of massive scalar perturbations of a rotating black hole*, Ann. Phys. **118**, 139 (1979).

[23] S. Detweiler, *Klein-Gordon equation and rotating black holes*, Phys. Rev. D **22**, 2323 (1980).

[24] R. Penrose and R. M. Floyd, *Extraction of Rotational Energy from a Black Hole*, Nat. Phys. Sci. **229**, 177 (1971).

[25] H. Furuhashi and Y. Nambu, *Instability of Massive Scalar Fields in Kerr-Newman Spacetime*, Prog. Theor. Phys. **112**, 983 (2004).

[26] J. Rosa, *The extremal black hole bomb*, J. High Energy Phys. **2010**, 15 (2010).

[27] D. Baumann *et al.*, *The spectra of gravitational atoms*, J. Cosmol. Astropart. Phys. **2019**, 006 (2019).

[28] R. Brito, V. Cardoso and P. Pani, *Superradiance, New Frontiers in Black Hole Physics* (Springer International Publishing, 2020).

[29] A. Arvanitaki and S. Dubovsky, *Exploring the string axiverse with precision black hole physics*, Phys. Rev. D **83**, 044026 (2011).

[30] A. Arvanitaki, M. Baryakhtar and X. Huang, *Discovering the QCD axion with black holes and gravitational waves*, Phys. Rev. D **91**, 084011 (2015).

[31] R. Brito, V. Cardoso and P. Pani, *Black holes as particle detectors: evolution of superradiant instabilities*, Class. Quant. Gravity **32**, 134001 (2015).

[32] A. Arvanitaki *et al.*, *Black hole mergers and the QCD axion at Advanced LIGO*, Phys. Rev. D **95**, 043001 (2017).

[33] D. Baumann, H. S. Chia and R. A. Porto, *Probing ultralight bosons with binary black holes*, Phys. Rev. D **99**, 044001 (2019).

[34] D. Baumann *et al.*, *Gravitational collider physics*, Phys. Rev. D **101**, 083019 (2020).

[35] V. Cardoso *et al.*, *Constraining the mass of dark photons and axion-like particles through black-hole superradiance*, J. Cosmol. Astropart. Phys. **2018**, 043 (2018).

[36] A. Gruzinov, *Black Hole Spindown by Light Bosons*, (2016), 1604.06422.

[37] M. Baryakhtar *et al.*, *Black hole superradiance of self-interacting scalar fields*, Phys. Rev. D **103**, 095019 (2021).

[38] T. W. Kephart and T. J. Weiler, *Stimulated radiation from axion cluster evolution*, Phys. Rev. D **52**, 3226 (1995).

[39] J. G. Rosa and T. W. Kephart, *Stimulated Axion Decay in Superradiant Clouds around Primordial Black Holes*, Phys. Rev. Lett. **120**, 231102 (2018).

[40] T. Ikeda, R. Brito and V. Cardoso, *Blasts of Light from Axions*, Phys. Rev. Lett. **122**, 081101 (2019).

[41] D. Blas and S. J. Witte, *Imprints of axion superradiance in the CMB*, Phys. Rev. D **102**, 103018 (2020).

[42] C. M. Yoo *et al.*, *Axion Cloud Decay due to the Axion-photon Conversion with Background Magnetic Fields*, (2021), 2103.13227.

[43] J. P. Conlon and C. A. Herdeiro, *Can black hole superradiance be induced by galactic plasmas?*, Phys. Lett. B **780**, 169 (2018).

[44] A. Caputo *et al.*, Electromagnetic signatures of dark photon superradiance, 2021.

[45] D. Blas and S. J. Witte, *Quenching mechanisms of photon superradiance*, Phys. Rev. D **102**, 123018 (2020).

[46] H. Bondi, *On Spherically Symmetrical Accretion*, Mon. Not. Roy. Astron. Soc. **112**, 195 (1952).

[47] I. D. Novikov and K. S. Thorne, Black Holes (Les Astres Occlus), pp. 343–450, 1973.

[48] A. Hook *et al.*, *Radio Signals from Axion Dark Matter Conversion in Neutron Star Magnetospheres*, Phys. Rev. Lett. **121**, 241102 (2018).

[49] J. E. Kim, *Weak-Interaction Singlet and Strong* CP *Invariance*, Phys. Rev. Lett. **43**, 103 (1979).

[50] M. Dine, W. Fischler and M. Srednicki, *A simple solution to the strong CP problem with a harmless axion*, Phys. Lett. B **104**, 199 (1981).

[51] R. Z. Ferreira, A. Notari and F. Rompineve, *Dine-Fischler-Srednicki-Zhitnitsky axion in the CMB*, Phys. Rev. D **103**, 063524 (2021).

[52] T. A. Thompson *et al.*, *A noninteracting low-mass black hole–giant star binary system*, Science **366**, 637 (2019).

[53] LIGO Scientific Collaboration and Virgo Collaboration, B. Abbott *et al.*, *Observation of Gravitational Waves from a Binary Black Hole Merger*, Phys. Rev. Lett. **116**, 061102 (2016).

[54] A. Chael *et al.*, *The role of electron heating physics in images and variability of the Galactic Centre black hole Sagittarius A**, Mon. Not. Roy. Astron. Soc. **478**, 5209 (2018).

[55] Event Horizon Telescope collaboration, K. Akiyama *et al.*, *First M87 Event Horizon Telescope Results. V. Physical Origin of the Asymmetric Ring*, Astrophys. J. Lett. **875**, L5 (2019).

[56] LIGO Scientific Collaboration, R. Abbott *et al.*, *GW190521: A Binary Black Hole Merger with a Total Mass of* $150M_{\odot}$, Phys. Rev. Lett. **125**, 101102 (2020).

[57] R. P. Kerr, *Gravitational Field of a Spinning Mass as an Example of Algebraically Special Metrics*, Phys. Rev. Lett. **11**, 237 (1963).

[58] J. M. Bardeen, B. Carter and S. W. Hawking, *The Four Laws of Black Hole Mechanics*, Commun. Math. Phys. **31**, 161 (1973).

[59] C. S. Reynolds, *Observational Constraints on Black Hole Spin*, Annu. Rev. Astron. Astrophys. **59**, 117 (2021).

[60] M. Guirdy, *Modern general relativity* (Cambridge University Press, 2019).

[61] Y. B. Zel'dovich, *Amplification of Cylindrical Electromagnetic Waves Reflected from a Rotating Body*, J. Exp. Theor. Phys. **35**, 1085 (1972).

[62] V. Cardoso *et al.*, *The Black hole bomb and superradiant instabilities*, Phys. Rev. D **70**, 044039 (2004).

[63] W. Unruh, *Separability of the Neutrino Equations in a Kerr Background*, Phys. Rev. Lett. **31**, 1265 (1973).

[64] S. R. Dolan, *Instability of the massive Klein-Gordon field on the Kerr spacetime*, Phys. Rev. D **76**, 084001 (2007).

[65] D. R. Brill *et al.*, *Solution of the Scalar Wave Equation in a Kerr Background by Separation of Variables*, Phys. Rev. D **5**, 1913 (1972).

[66] M. A. Abramowicz and P. C. Fragile, *Foundations of Black Hole Accretion Disk Theory*, Living Rev. Relativ. **16** (2013).

[67] N. I. Shakura and R. A. Sunyaev, *Black holes in binary systems. Observational appearance.*, Astron. Astrophys. **500**, 33 (1973).

[68] G. Beskin and S. Karpov, *Low-rate accretion onto isolated stellar mass black holes*, Astron. Astrophys. **440**, 223 (2005).

[69] S. L. Shapiro and S. A. Teukolsky, *Black Holes, White Dwarfs, and Neutron Stars* (John Wiley & Sons, Ltd, 1983).

[70] J. R. Ipser and R. H. Price, *Synchrotron radiation from spherically accreting black holes*, Astrophys. J. **255**, 654 (1982).

[71] F. Yuan and R. Narayan, *Hot Accretion Flows Around Black Holes*, Annu. Rev. Astron. Astrophys. **52**, 529 (2014).

[72] R. Mahadevan and E. Quataert, *Are Particles in Advection-dominated Accretion Flows Thermal?*, Astrophys. J. **490**, 605 (1997).

[73] R. P. Fender, T. J. Maccarone and I. Heywood, *The closest black holes*, Mon. Not. Roy. Astron. Soc. **430**, 1538 (2013).

[74] C. O. Lousto and Y. Zlochower, *Hangup Kicks: Still Larger Recoils by Partial Spin-Orbit Alignment of Black-Hole Binaries*, Phys. Rev. Lett. **107**, 231102 (2011).

[75] F. Scarcella *et al.*, *Multiwavelength detectability of isolated black holes in the Milky Way*, Mon. Not. Roy. Astron. Soc. **505**, 4036 (2021).

[76] D. Gaggero *et al.*, *Searching for Primordial Black Holes in the Radio and X-Ray Sky*, Phys. Rev. Lett. **118**, 241101 (2017).

[77] J. Manshanden *et al.*, *Multi-wavelength astronomical searches for primordial black holes*, J. Cosmol. Astropart. Phys. **2019**, 026–026 (2019).

[78] M. Colpi, L. Maraschi and A. Treves, *Two-temperature model of spherical accretion onto a black hole.*, Astrophys. J. **280**, 319 (1984).

[79] D. Psaltis, *The Influence of Gas Dynamics on Measuring the Properties of the Black Hole in the Center of the Milky Way with Stellar Orbits and Pulsars*, Astrophys. J. **759**, 130 (2012).

[80] C. F. McKee and J. P. Ostriker, *A theory of the interstellar medium: three components regulated by supernova explosions in an inhomogeneous substrate.*, Astrophys. J. **218**, 148 (1977).

[81] K. M. Ferrière, *The interstellar environment of our galaxy*, Rev. Mod. Phys. **73**, 1031 (2001).

[82] F. Nicastro *et al.*, *Observations of the missing baryons in the warm–hot intergalactic medium*, Nature **558**, 406 (2018).

[83] P. Sikivie, *Experimental Tests of the Invisible Axion*, Phys. Rev. Lett. **51**, 1415 (1983).

[84] G. Raffelt and L. Stodolsky, *Mixing of the Photon with Low Mass Particles*, Phys. Rev. D **37**, 1237 (1988).

[85] T. D. P. Edwards *et al.*, *Unique Multimessenger Signal of QCD Axion Dark Matter*, Phys. Rev. Lett. **124**, 161101 (2020).

[86] L. M. Widrow, *Origin of galactic and extragalactic magnetic fields*, Rev. Mod. Phys. **74**, 775 (2002).

[87] J. Redondo and M. Postma, *Massive hidden photons as lukewarm dark matter*, J. Cosmol. Astropart. Phys. **02**, 005 (2009).

[88] B. Cecconi, *Goniopolarimetry: Space-borne radio astronomy with imaging capabilities*, C. R. Phys. **15**, 441 (2014).

[89] B. Cecconi *et al.*, 2018 IEEE Aerospace Conference, pp. 1–19, 2018.

[90] X. Chen *et al.*, *Discovering the Sky at the Longest Wavelengths with Small Satellite Constellations*, (2019), 1907.10853.

[91] J. M. Wrobel and R. C. Walker, Synthesis Imaging in Radio Astronomy II, edited by G. B. Taylor, C. L. Carilli and R. A. Perley, Vol. 180, of *Astronomical Society of the Pacific Conference Series*, p. 171, 1999.

[92] B. T. Draine, *Physics of the interstellar and intergalactic medium* (Princeton University Press, 2010).

[93] R. A. Sunyaev and Y. B. Zeldovich, *Small-Scale Fluctuations of Relic Radiation*, Astrophys. Space Sci. **7**, 3 (1970).

[94] E. L. Wright, *Distortion of the microwave background by a hot intergalactic medium.*, Astrophys. J. **232**, 348 (1979).

[95] M. E. Peskin and D. V. Schroeder, *An introduction to quantum field theory* (Westview, 1995).

[96] M. Samland, *Modeling the Evolution of Disk Galaxies. II. Yields of Massive Stars*, Astophys. J. **496**, 155 (1998).

[97] A. M. Green and B. J. Kavanagh, *Primordial black holes as a dark matter candidate*, J. Phys. G Nucl. Part. Phys. **48**, 043001 (2021).

[98] A. Aguayo-Ortiz *et al.*, *Spherical accretion: Bondi, Michel, and rotating black holes*, Mon. Not. Roy. Astron. Soc. **504**, 5039 (2021).

[99] M. Abramowitz and I. A. Stegun, *Handbook of mathematical functions* (Dover Publications, 1970).

[100] V. Shtabovenko, R. Mertig and F. Orellana, *FeynCalc 9.3: New features and improvements*, Comput. Phys. Commun. **256**, 107478 (2020).

[101] A. J. Millar *et al.*, *Dielectric haloscopes to search for axion dark matter: theoretical foundations*, J. Cosmol. Astropart. Phys. **2017**, 061–061 (2017).

TRITA SCI-GRU 2021:348